Spring 2013

Numerical modeling of porosity and macrosegregation in continuous casting of steel

Pengfei Du
University of Iowa

NUMERICAL MODELING OF POROSITY AND MACROSEGREGATION IN CONTINUOUS CASTING OF STEEL

by

Pengfei Du

An Abstract

Of a thesis submitted in partial fulfillment
of the requirements for the Doctor of
Philosophy degree in Mechanical Engineering
in the Graduate College of
The University of Iowa

May 2013

Thesis Supervisor: Professor Christoph Beckermann

ABSTRACT

The continuous casting process is a widely used technique in modern steel plants. However, it is a complicated process that is not well understood. The objective of this research is to model the porosity and macrosegregation due to shrinkage related effects and solid deformation in the continuous casting of steel.

Solid phase movements due to bulging and variable roll gap are modeled with a simple algebraic equation based on assumed slab surface deflection. A simplified single domain fluid flow model is derived to predict the pressure field. When liquid pressure drops to zero, porosity starts to form. The distribution of porosity is calculated using the porosity equation which is based on the mass conservation. A macrosegregation model based on the species conservation is derived. With the relative velocity calculated from the pressure results and the solid velocity, macrosegregation is obtained. Since the solid phase velocity is not zero and mixture density is not assumed to be constant, porosity and macrosegregation due to both solid deformation and shrinkage effects are incorporated.

In order to validate the model, the pressure field of a three-dimensional pure metal solidification system is simulated. The results show the feasibility of the proposed model to predict the fluid flow. The porosity and macrosegregation prediction for different casting conditions are performed. The results confirm the necessity of including solid phase deformation in the prediction of porosity and centerline macrosegregation. The results also reveal the relations between different operating conditions (such as degree of bulging, soft reduction, and casting speed) and the porosity/macrosegregation defects in the final product.

Abstract Approved: _____
Thesis Supervisor

_____
Title and Department

_____
Date

NUMERICAL MODELING OF POROSITY AND MACROSEGREGATION IN CONTINUOUS CASTING OF STEEL

by

Pengfei Du

A thesis submitted in partial fulfillment
of the requirements for the Doctor of
Philosophy degree in Mechanical Engineering
in the Graduate College of
The University of Iowa

May 2013

Thesis Supervisor: Professor Christoph Beckermann

Graduate College
The University of Iowa
Iowa City, Iowa

CERTIFICATE OF APPROVAL

_____

PH.D. THESIS

_____

This is to certify that the Ph.D. thesis of

Pengfei Du

has been approved by the Examining Committee
for the thesis requirement for the Doctor of Philosophy
degree in Mechanical Engineering at the May 2013 graduation.

Thesis Committee: _____
Christoph Beckermann, Thesis Supervisor

_____
Colby C. Swan

_____
Jia Lu

_____
Albert Ratner

_____
Richard Hardin

ACKNOWLEDGMENTS

I am grateful to my advisor, Professor Chiristoph Beckermann, for his valuable and constructive suggestions during last five years. His willingness to guide me through the dark has been very much appreciated. This work would not have been possible without his support.

I would like to thank Dr. Richard Hardin. His earlier work provides the starting point of current research. Throughout these years, he is always ready to help with suggestions. Also, I would like to thank him for maintaining the computers in the lab.

I would also like to extend my thanks to the committee members: Professor Colby C. Swan, Professor Albert Ratner, Professor Jia Lu, and Dr. Richard Hardin for their valuable time and helpful comments.

I would like to express my gratitude to all my friends and colleagues in solidification lab, Dr. Kent Carlson, Dr. Masashi Yamaguchi, Mr. Daniel Galles, Mr. Greg Samuels, Mr. Jacob Thole, Mr. Matt Pokorny and lots of others for their suggestions and accompanying.

Finally, I would like to give my special thanks to my parents and my sister for their constant love and encouragement throughout my life.

ABSTRACT

The continuous casting process is a widely used technique in modern steel plants. However, it is a complicated process that is not well understood. The objective of this research is to model the porosity and macrosegregation due to shrinkage related effects and solid deformation in the continuous casting of steel.

Solid phase movements due to bulging and variable roll gap are modeled with a simple algebraic equation based on assumed slab surface deflection. A simplified single domain fluid flow model is derived to predict the pressure field. When liquid pressure drops to zero, porosity starts to form. The distribution of porosity is calculated using the porosity equation which is based on the mass conservation. A macrosegregation model based on the species conservation is derived. With the relative velocity calculated from the pressure results and the solid velocity, macrosegregation is obtained. Since the solid phase velocity is not zero and mixture density is not assumed to be constant, porosity and macrosegregation due to both solid deformation and shrinkage effects are incorporated.

In order to validate the model, the pressure field of a three-dimensional pure metal solidification system is simulated. The results show the feasibility of the proposed model to predict the fluid flow. The porosity and macrosegregation prediction for different casting conditions are performed. The results confirm the necessity of including solid phase deformation in the prediction of porosity and centerline macrosegregation. The results also reveal the relations between different operating conditions (such as degree of bulging, soft reduction, and casting speed) and the porosity/macrosegregation defects in the final product.

TABLE OF CONTENTS

LIST OF TABLES

Table

LIST OF FIGURES

Figure

LIST OF NOMENCLATURE

a	Constant
x, y, z	Spatial coordinates (m)
T	Temperature (K)
T_m	Melting temperature of the pure material (K)
T_{liq}	Liquidus temperature (K)
T	Time (s)
V	Volume (m^3)
$\mathbf{v}$	Velocity vector (m/s)
$\mathbf{v}_{rel}$	Relative velocity (m/s)
v_{cast}	Casting speed (m/s)
ρ	Density ($kg \bullet m^{-3}$)
$\vec{n}$	Unit normal vector
g	Volume fraction
$\vec{g}$	Acceleration vector ($m \bullet s^{-2}$)
H	Enthalpy ($J \bullet kg^{-1}$)
L	Latent heat ($J \bullet kg^{-1}$)
κ	Partition/Segregation coefficient (wt%/wt%)
C_{mix}	Chemical composition concentration (wt%)
$C_{nominal}$	Nominal chemical composition concentration (wt%)
c	Specific heat ($J\ kg^{-1}\ K^{-1}$)
k	Thermal conductivity ($W\ m^{-1}\ K^{-1}$)
ω	Thermal conduction enhancement factor

T_{ext}	The external temperature (K)
h	Heat transfer coefficient ($W \bullet m^{-2} \bullet K^{-1}$)
w	Spray cooling flux ($L/m^2 \bullet s$)
ε	Emissivity
σ	Stefan-Boltzmann constant ($W \bullet m^{-2} \bullet K^{-4}$)
$\mathbf{K}^{[2]}$	Second order permeability tensor (m^2)
K	Permeability (m^2)
G	Thermal gradient ($K \bullet m^{-1}$)
$\dot{T}$	Cooling rate ($K \bullet s^{-1}$)
β	Coefficient of thermal expansion (K^{-1})
λ_1	Primary dendrite arm spacing (μm)
λ_2	Secondary dendrite arm spacing (μm)
μ	Dynamic viscosity ($kg \bullet m^{-1} \bullet s^{-1}$)
f	Friction factor
G	Thermal gradient ($K \bullet m^{-1}$)
$\boldsymbol{\sigma}$	Cauchy stress tensor
$\boldsymbol{\tau}$	Viscous stress tensor
$\mathbf{b}$	Body force vector
$\mathbf{M}$	Interfacial momentum transfer ($N \bullet s$)
p	Pressure (Pa)
Δp	Pressure drop
γ_{lg}	Liquid-gas interfacial energy
D	Diffusion coefficient ($m^2 \bullet s^{-1}$)
δ_b	Surface deflection due to bulging (m)

δ_g	Surface deflection due to variable roll gap (m)
$\delta_{\max}$	Maximum bulging (m)

Superscripts

d	Dissipative terms
T	Transpose

Subscripts

s	Solid phase
l	Liquid phase
m	Mushy zone
p	Quantity of pore phase
i	Phase *i*
spray	Quantities related to spray cooling

CHAPTER I

INTRODUCTION

1.1 Background and Motivation

In order to stay competitive in the worldwide market, steel producers are improving steel quality at lowest costs. The percentage of steel manufactured by continuous casting has been regularly increasing, reaching an average of 66% worldwide (over 98% in Japan and 90% in Europe).

According to a report from American Iron and Steel Institute in 2005 [1], it is estimated that a 1% reduction of scrapped product due to casting related defects (such as slab cracking from improper cooling, porosity, etc.) can result in an annual energy saving of 0.147 trillion kJ for a single steel plant in our region of the United States. Continuous caster operation and practice depend heavily on workers' experience, and are carried out by trial and error. To achieve optimum operating conditions, such industrial experiments can be extremely expensive. Therefore, it is important that the steel producers understand the effects of each operating parameter and can improve product quality with a high yield through computer experiments. With the assistance of mathematical models, phenomena like energy transportation, fluid flow and solid deformation can be determined prior to the actual casting. The effects of the operating conditions can be investigated through numerical study. This method greatly facilitates the optimization of the industrial practice by increasing energy efficiency and avoiding defects with less cost.

Two common defects appearing during the casting processes are porosity and macrosegregation. A porosity defect is either a gas entrapment or a void area in the casting product. Macrosegregation is a spatial uneven distribution of compositions in the casting process. Both of these defects are able to undermine the product quality and can even cause casting rejection. It will be a great advantage if these defects can be predicted. However, there are difficulties in the modeling of related phenomena appearing in the

continuous casting of steel. One of those challenges is the solid phase deformation due to thermal and mechanical stresses. It is essential to the understand defect formation and to improve the continuous caster machine design [2-4]. Since the solid deformation behavior is not well understood, there is no work published on porosity modeling in the continuous casting process. Available models on macrosegregation consider solid movement; however neglect the presence of porosity. Therefore, to predict porosity and macrosegregation defects in the continuous casting process more sophisticated models are needed.

1.2 Introduction to the Continuous Casting Process

Continuous casting is a process that molten melt is solidified into a semi-finished bloom, billet or slab. There are different continuous casting installations in use today as shown in Figure 1.1. The choice of arrangement is simply based on the ease of process handling and consideration of safety. The curved continuous casting is the one widely used in steel making companies and will be discussed in detail in this work. Compared to the ingot casting, the benefits of continuous casting process are: 1, higher yield; 2, semi-finished products; 3, less segregation; 4, better surface finish.

The typical continuous casting process for steel slabs is illustrated in Figure 1.2. In the continuous casting process the steel melt is poured from the ladle into a container known as a tundish and then flows through a submerged nozzle into the mold where the molten steel is subjected to "primary cooling" by the mold surface. The mold is initially sealed with a dummy bar to prevent the liquid melt to flow out. Due to the energy extraction from the water-cooled mold, a thin solidified shell starts to form at this stage. When the solid shell thickness is sufficient to support the liquid core, the steel is withdrawn out of the mold at the casting speed. Below the mold, the solid outer shell is cooled with water spray along the strand, which is known as secondary cooling. Liquid melt is continuously poured into the mold to replenish the steel withdrawn at the same

rate. Below the mold, the metal strand passes through a series of water-cooled rolls which support the strand against gravity. Between each pair of successive rolls along casting direction, the liquid core exerts ferrostatic pressure causing the bulging of slab surface (Figure 1.3). The strand is solidified until the liquid core disappears and finally cut to desired length and sent to further processing or storage.

Continuous casting of steel and other metal alloys is a multicomponent phase change problem that differs in many ways from the phase change of pure substances. The solidification of metal alloys takes place over a temperature range within which the solid and liquid phase can coexist. The solidification path of the multicomponent system can be determined from the phase diagram. A typical equilibrium phase diagram of a binary system is shown in Figure 1.4. When the liquid metal with composition C_0 is cooled, the solid phase starts to form at the liquidus temperature according to the composition C_0. At any temperature within the solidification temperature range, the solid phase has a composition C_s different from liquid composition C_l as solid and liquid have different solubilities of solute. Since the liquid phase is richer in solute, the buildup of the solute at the solidification front leads to instabilities which drive the formation and growth of complex microstructures called dendrites. The dendrites can be divided into two classes: columnar dendrite and equiaxed dendrite. The dendrites and the liquid melt surrounding them form a multiphase zone called mushy zone. Figure 1.5 shows the solid, liquid and mushy zone appearing during the solidification of metal alloys. For the diagram shown in Figure 1.4, the solidification ends when the temperature of the system drops to the eutectic temperature.

There are a numerous physical phenomena involved in the continuous casting of steel and require investigations to formulate accurate mathematical model. Modelers in metal casting field need broad knowledge in energy/species transportation, thermodynamics, fluid flow in bulk liquid and mushy zone, and solid deformation. In the continuous casting process, several operating conditions, including the geometry of the

mold, the heat extraction from the mold, the secondary cooling water quantity, the distribution of spray nozzles (spray pattern), the spatial arrangement of the supporting rolls and the casting speed, affect the quality of the final product. However, each of these factors can be complex and their influences on the quality of final product are not thoroughly understood. The interactions between them make the problem even more complicated. Numerical modeling of the continuous casting is becoming a very useful tool to design the casting process and minimize industrial trials to optimize caster operation. With increasing power of the computer, numerical experiment is the best, if not only, way to study the effect of each parameter and to determine an optimized combination of them.

1.3 Defects

Many research in metal casting aim to increase the productivity and minimize defects. To achieve this goal, one has to identify the defects and understand the causes. Since the objective of this research concentrates on mathematical modeling of porosity and macrosegregation, in this section, these two defects are described in detail, and others are briefly mentioned.

1.3.1 Porosity

Porosity is one of the major defects in metal casting. Porosity formed in the product will decrease the mechanical performance of the material significantly. For example, porosity degrades properties like fatigue resistance and tensile strength. Thus it is important to know when porosity forms and how to minimize the negative effects.

When the engineers encounter a porosity problem, the first task is deciding the type of porosity and then determine the solutions [5, 6]. Based on its size, porosity is divided into two types: micro-porosity and macro-porosity. Micro-porosity is small and almost invisible to the naked eye, while macro-porosity is a large scale defect in the castings visible to the naked eye. All porosity is believed to be the result of either poor

feeding or gas bubble formation. When the poorly fed region is large and cut off of liquid feeding, for example when pouring is stopped at the free surface, the resulting void is called macro-porosity; if the poorly fed region appears at the scale of dendrites, micro-porosity forms. The macro-porosity can be eliminated by changing the design of the mold or operating method, while the micro-porosity resides in the casting. There are no fundamental differences between these two types of porosities: one can gradually transform to the other as the unfed region can grow to a macroscopic volume or shrink (due to compression) to a microscopic one.

It is more meaningful to classify porosity into gas porosity, shrinkage porosity and porosity due to solid deformation based on the mechanism of their formation. The gas porosity occurs because the liquid melt can hold more dissolved gas than the solid phase. As the liquid melt cools down, the newly formed solid phase starts to reject gas content into the surrounding liquid. When the concentration of gas molecules reaches a critical value, a distinct phase, i.e., porosity, forms. Nitrogen, oxygen and hydrogen are the most common gases causing the gas porosity. Gas porosity can be trapped inside of the metal or appear on the surface of the casting. Gas porosity forms in the early stage of solidification, its growth is not restricted by the dendrite structure and the surface is smooth as shown in Figure 1.6. The main cause of shrinkage porosity is that the phase transformation induces volume difference inside of the material and the mass flow is inadequate in filling this volume difference. Shrinkage porosity grows at the dendrite root where the phase transformation happens. The shape of shrinkage porosity is irregular, which can be clearly seen from Figure 1.7. Whereas gas porosity can be minimized by degassing treatment of the liquid melt or by preparing the melt in an environment of low solubility gases, such as argon, to prevent contact with air; the shrinkage porosity is more of an intrinsic defect that can only be eliminated by compressing stress. However, in most situations, only tensile stress is present.

The presence of tensile stress will introduce another kind of porosity: porosity due to solid deformation/movement. This is another type of porosity defect commonly encountered in metal casting, especially alloys with long freezing ranges and castings under tensile stress. It is believed to be a type of porosity initiated at high solid fraction region during solidification. The cause of porosity due to solid deformation is similar to that of shrinkage porosity. Both of them are due to a lack of feeding in the mushy zone. If liquid feeding is not adequate under tensile loading, in addition to shrinkage porosity, porosity due to solid deformation starts and propagates. More commonly, porosity due to solid deformation is encountered in complex shape casting where the free contraction is hindered by the mold and the large scale castings with severe temperature gradients. Since porosity due to solid deformation occurs late at solidification, it is along the grain boundary and with complex shapes. Figure 1.8 shows a typical porosity due to deformation in billets.

Porosity in the continuous casting process mainly associated with the presence of the deep liquid crater and complex dendrite structure. At the solidification front around the center plane region, liquid is not able to penetrate the dendrite structure to feed the shrinkage. Also, due to the bulging effect, the ferrostatic pressure tends to split the solidification front apart. One of the most effective ways of mitigating the porosity in the product is by applying mild roll tapering, which is the principle behind soft reduction. The reduced roll gap squeezes solid shell toward the center and thus the solid phase feeds and reduces the porosity level.

1.3.2 Macrosegregation

Segregation is defined as non-uniform distribution of chemical composition in solidification process. It is classified into two categories: micro- and macro- segregation. While microsegregation initiates from the different solubility of chemical composition in solid and liquid phase, macrosegregation is closely related to the macroscopic

transportation of the chemical composition. Microsegregation appears on the length scale of the dendrites, typically 10-100 μm. Macrosegregation demonstrates itself on a scale from several millimeters to centimeters or even larger. Compared to microsegregation, macrosegregation is more harmful because microsegregation can be eliminated by homogenization treatment, but macrosegregation cannot be eliminated due to the large diffusion length required.

The main pre-condition of macrosegregation is that a relative velocity exits between the liquid phase and the solid phase. The relative velocity transports the solute-rich liquid away from the solid phase which is in equilibrium with the liquid. There are three main origins of the relative flow: fluid flow in the bulk liquid region caused by the feeding of molten steel from the ladle; fluid flow driven by density change due to temperature and concentration differences; deformation of the columnar dendrite or sedimentation of equiaxed dendrites.

Figure 1.9 shows the macrosegregation pattern in a steel ingot. Several typical modes of macrosegregation can be observed: 1) the dendrite solidified in the early stage with poor solute content settles down to the bottom of the ingot and forms a negative segregate cone; 2) the positive segregation (the hot-top segregation) near the top appears at the final stage of solidification due to buoyancy and shrinkage driven flow; 3) the V-segregation due to the equiaxed grains settling in the center and the deformation induced feeding of solute enriched liquid; 4) the A-segregation which is a solute enriched segregation due to the convection pattern; 5) the bands near the surface of the ingot which is due to the unsteady heat transfer of fluid flow in the early stage of solidification .

Macrosegregation patterns are also observed in continuous castings. Figure 1.10 shows a longitudinal section of a carbon steel product produced by continuous casting. The V-segregation can still be observed in the central area. White bands are also visible. Here in this case the white bands are raised from intense liquid flow with respect to the solidification front. The most harmful segregation in the continuous casting is the

centerline segregation (a positive segregation in nature). This centerline segregation is believed to be caused by the bulging effect which draws solute enriched liquid into the center of the casting [7].

Efforts are made to control the fluid flow and the solid phase movement so as to reduce the macroscopic species transportation during the continuous casting process. One of the promising techniques is to use electromagnetic stirring [8-10]. Also, it is known that the centerline macrosegregation can be reduced by mechanical soft reduction process [11, 12]. Research has shown that the efficiency of soft reduction depends on the reduction rate, contents of liquid phase, as well as various operating conditions.

1.3.3 Other Common Defects

There are many other defects that are commonly observed in the continuous casting of steel. To meet the increasing demand for high quality products, they all attract researchers' attention.

Non-metalic inclusions are significant problems that can lead to rejected castings. Ginzburg and Ballas [13] pointed out that many defects in cast slab and hot rolled products are directly related to inclusions. The inclusions, for example oxides or sulphides, can considerably decrease the ductility of metal. Inclusions can act as stress raisers and also decrease metal's resistance to corrosion.

Distortion is a common shape defect. Due to the large thermal gradients in a casting, different parts experiences different thermal strain. As a result of this inhomogeneous straining of the solid, the final shape can be different from the intended shape.

Table 1.1 summarizes some common defects found in the continuous casting process. In order to produce metal casting products with decent quality at high speed, a wide range of subjects need to be considered.

1.4 Aim of the Research

For the past few decades, porosity formation and macrosegregation in casting processes has been active fields of research. Both experimental and theoretical efforts have been made to achieve better understanding of these topics. As will be evident in Chapter 2, all available mathematical models for porosity assume that the solid phase does not deform and thus only predict shrinkage or gas porosity. However, in the continuous casting of steel, the solid shell and the mushy zone deform and contribute to the porosity formation. Unfortunately, no work has been published on porosity calculation for the continuous casting of steel. To this end, this research intends to construct a mathematical model for the calculation of shrinkage porosity and porosity due to solid deformation in continuous casting of steel. Meanwhile, the existing models for macrosegregation in continuous casting of steel neglect the formation of porosity. In current proposed study, the influence of both shrinkage effects and solid deformation on macrosegregation will be modeled. The presence of porosity phase is also considered. Hence, our model is very general. However, the solid deformation modeling is based on simple algebraic model which is not a thermo-mechanical analysis and has lots of assumptions. As a result of this, the prediction could not be perfect.

1.5 Outline of Content

Chapter II provides a review of literatures related to thermal field, fluid flow, solid deformation, porosity and macrosegregation modeling. It outlines the literatures related to porosity and macrosegregation modeling of the continuous casting process. In Chapter III, mathematical models for porosity and macrosegregation prediction are derived. Chapter IV summarizes the computational setup for a standard testing case. Derived liquid flow model is validated in Chapter V and computational grid dependency study is performed to find a reasonable grid size to run the general calculations. Chapter VI explores the importance of solid deformation in porosity and macrosegregation

modeling. Effects of different operating conditions on porosity and macrosegregation level are also investigated. Finally, conclusions are drawn and future research is recommended in Chapter VII.

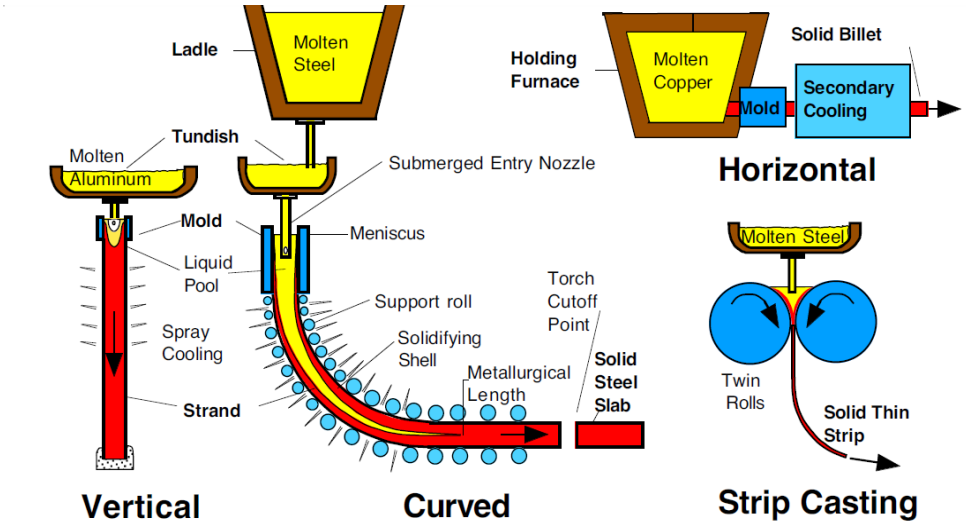

Figure 1.1 Various continuous casting processes [14].

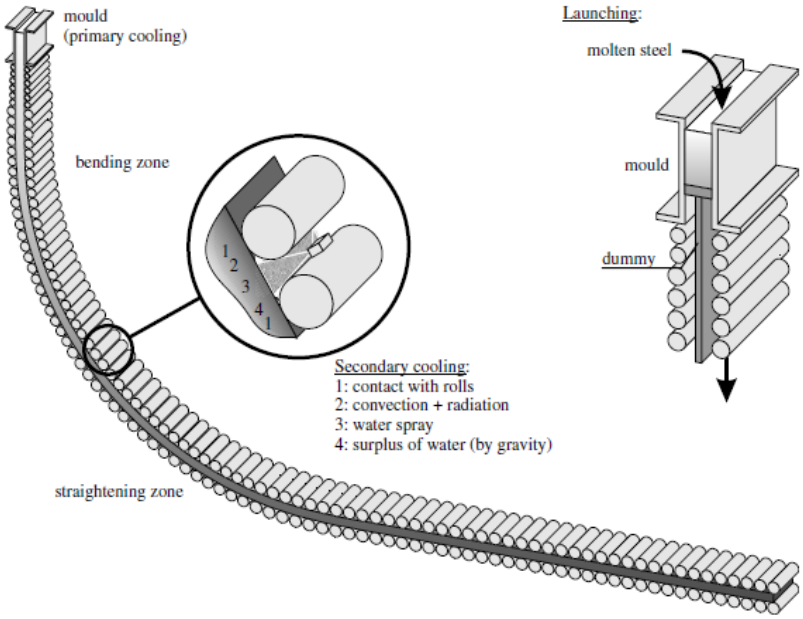

Figure 1.2 Three-dimensional sketch of continuous casting of steel [15].

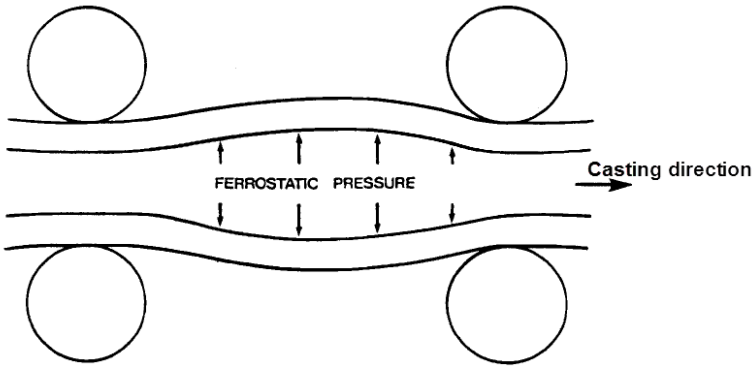

Figure 1.3 Schematic of slab bulging [16].

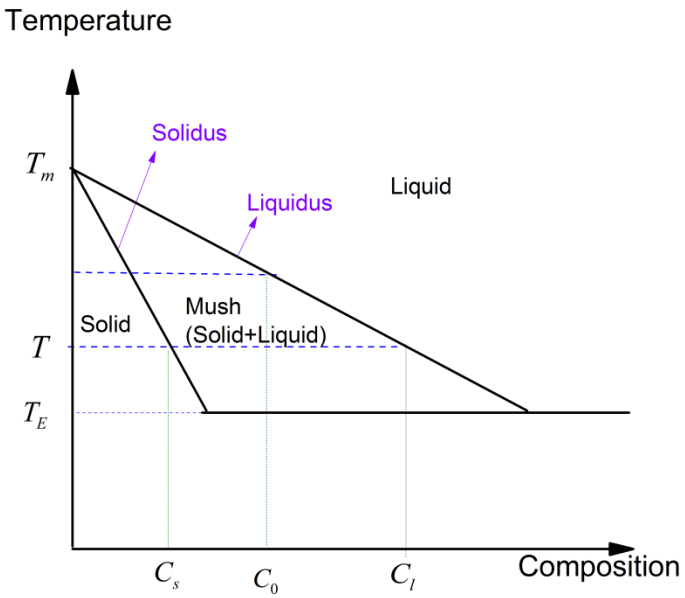

Figure 1.4 Typical phase diagram for binary alloy systems.

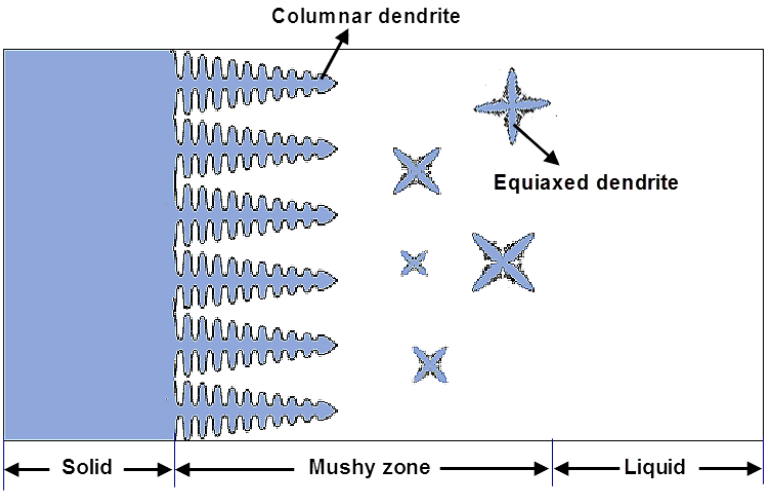

Figure 1.5 Solid, liquid, and mushy zone for alloys solidification.

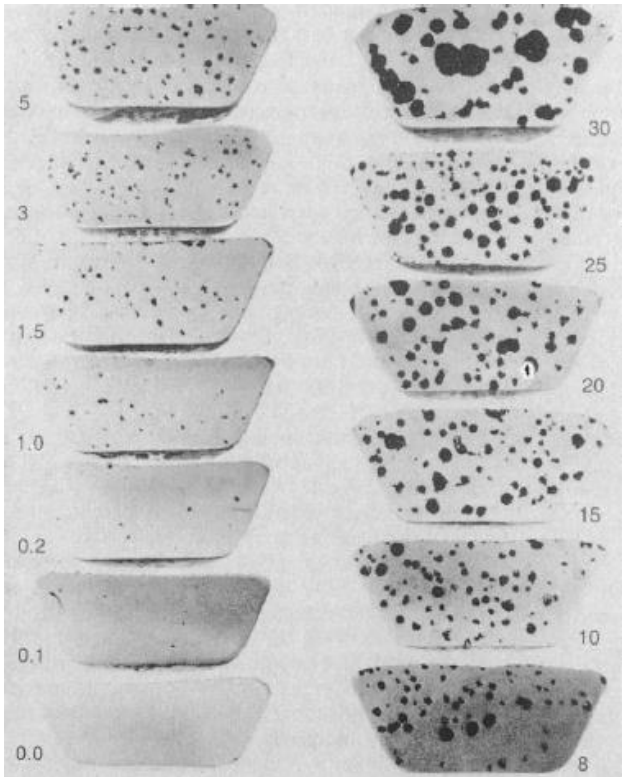

Figure 1.6 Gas porosity at various percentage levels [17].

Figure 1.7 Radiograph of shrinkage porosity in a carbon steel [17].

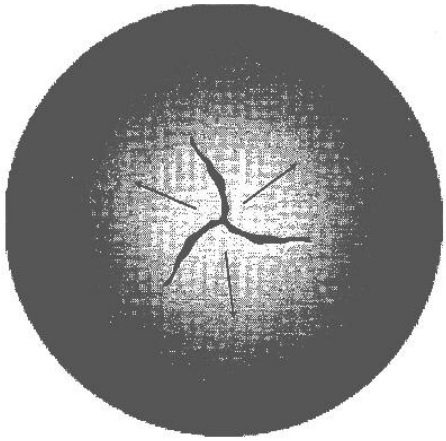

Figure 1.8 Typical porosity due to solid deformation in billet extrusion [18].

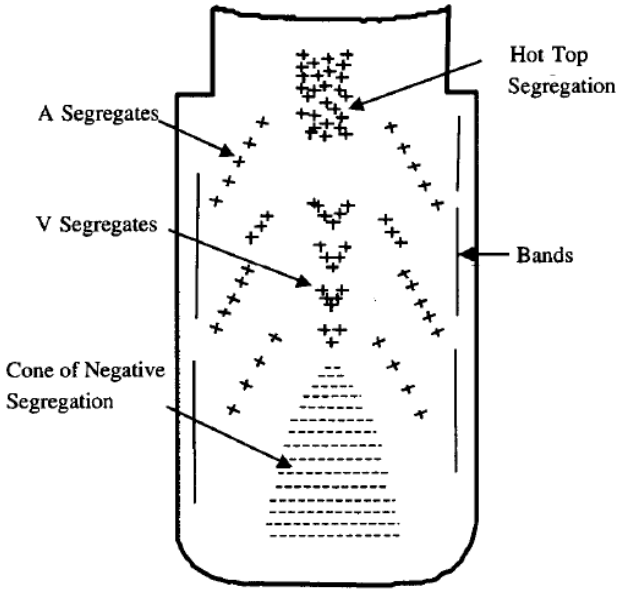

Figure 1.9 Schematic of macrosegregation in a steel ingot [19].

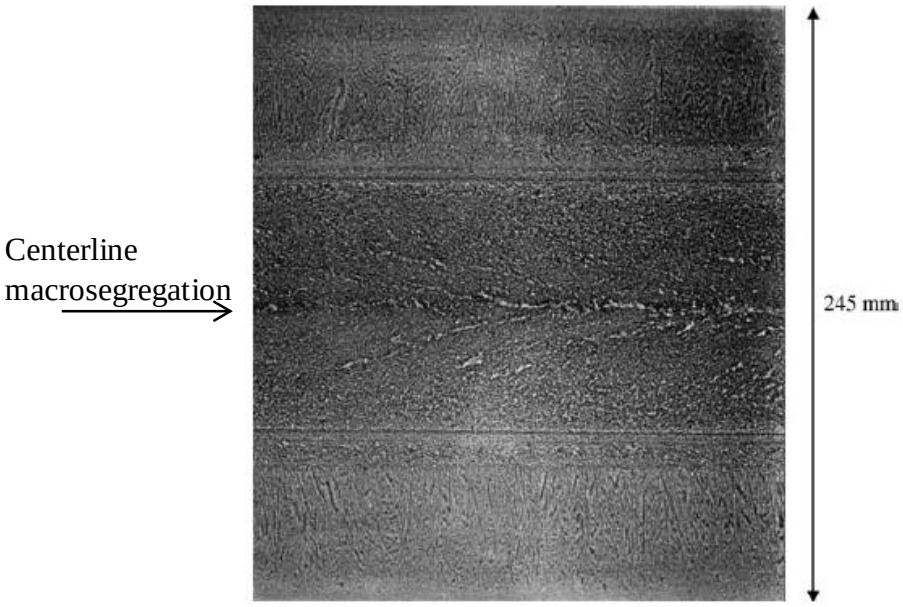

Figure 1.10 Longitudinal section of carbon steel by continuous casting [20].

Table 1.1 Common defects in continuous casting.

Internal defects	Surface defects
Hot tears (porosity due to deformation)	Oscillation mars
Shrinkage and gas porosity	Exudations or bleed-outs
Micro/Macrosegregation	Transversal corner or center cracks
Inclusions	Longitudinal center crack
Blow holes	Longitudinal depression, butt-curl, butt-swell

CHAPTER II

REVIEW OF LITERATURE

2.1 Introduction

Chapter I emphasized the importance of continuous casting of steel. Basic concepts and knowledge of the continuous casting process are illustrated. It is clear that it is of great advantage to use mathematical model to direct industrial production. In order to predict the defects in the final product in advance, it is necessary to model the heat transfer, fluid flow, and the deformation of the solid phase. Because of the complexity of the actual operating conditions and solidification phenomenon, no analytical solution exists for a real continuous casting process. Researchers today, using the various mathematical models together with the growing power of the computers, are able to solve complex problems with numerical methods, e.g., finite difference (FD) method, finite element (FE) method, and finite volume (FV) method. In this chapter, the mathematical models available for the simulation of phenomena related to the formation of porosity and macrosegregation occurring in the continuous casting process are reviewed.

2.2 Thermal Analysis

Fundamentally, to predict the defects occurring in the continuous casting process, the first thing we have to deal with is thermal analysis. For solidification problems, thermal analysis consists of temperature distribution and phase change. Temperature calculation is not an independent problem. Thermal energy is carried by fluid convection and solid movement, and for system with phase change, the latent heat is generated. A complete derivation of the energy equation for the solidification system can be found in many previous works [21-23] either using mixture theory or volume-averaged method. Beside the energy equation, a relationship between temperature and solid fraction is needed. The relationship can be established from a known data base or by certain simple

functions [24] which incorporate the effects of cooling rate and chemical contents. If both of the two are not available, microsegregation models [25-28] based on solute conservation are needed. The energy equation and the supplementary temperature-solid fraction relation described by microsegregation model are iteratively solved.

When applying the general energy equation to the continuous casting of steel, a couple of assumptions are made to simplify it. In most available work, energy transport due to convection is approximated by a thermal conductivity enhancement factor and energy transportation by solid phase movement is totally neglected.

By assuming that the heat flow along the casting direction is negligibly small comparing to that along the cross-sectional direction, Louhenkilpi [29] proposed a two-dimensional slice model which calculates the temperature field and the solid shell thickness in the cross-sections of the strand. The two-dimensional calculation domain is shown in Figure 2.1. Time is treated as a third dimension with the calculation domain running through the casting direction of the strand at the casting speed, v_{cast}. The work by Alizadeh [30] is another example of this type. This approach neglects the heat flow along the casting direction and thus only suitable for continuous casting of materials with relatively low thermal conductivity.

Louhenkilpi [31] presented a real-time heat-transfer model for continuous casting slab with example given for a casting of stainless steel. The model calculated the temperature field on a longitudinal cross section through the mid-width plane of the strand, as shown in Figure 2.2. Temperature-solid fraction relationship is prescribed using the model developed by Miettinen [32]. The spray cooling correlations depend on several variables like steel grade, slab surface temperature and spray water flux and are determined through a curve fitting procedure based on measured temperature values. The model is also able to do real-time calculation for changing in casting speeds, spray water flow rates for different steel grades. Hardin *et al.* [33] developed a two-dimensional transient heat transfer model called "DYSCOS" for continuous casters at IPSCO Inc. The

model also modeled the same domain as that in Louhenkilpi's model. Their model can use either known temperature-solid fraction relation or a microsegregation model. The model can predict the real-time temperature in response to dynamic changing of casting conditions (casting speed, spray cooling water flow rate, steel chemistry, pouring and ambient temperature) and also a control methodology is established that is able to control the surface temperature profile by dynamically adjusting the secondary cooling water flux. Since the longitudinal cross slice models consider heat transfer along casting direction, these models are suitable for the cases when longitudinal heat conduction is significant; however, these models neglect heat flow along the width direction. Therefore they are not applicable to slab casting but not for blooms or billets.

Three-dimensional steady state (TEMPSIMU3D) and dynamic(DYN3D) heat transfer models had been used by Louhenkilpi and coworkers [34]. The calculation domain extends from the meniscus to a predefined length. Their predicted liquid pool depth was good, but for the thermocouple measurements the agreement was not so good. There could be many reasons, e.g. the reliability of the measurements and the boundary conditions used are not locally accurate enough.

All previously mentioned work considered simple boundary that the local spray water and individual roll contact are not considered. The effect of spray cooling, roll contact, thermal radiation and natural convection are assumed to be constant or determined by some averaged heat transfer coefficient. A typical boundary condition setup is shown in Figure 2.3. Bealy *et al.* [35] studied the individual roll contact cooling. The model proposed by Hardin *et al.* [36-38] was the first to consider more realistic boundary conditions by dealing with the complex spray cooling pattern. Their model is a three-dimensional steady state model for continuous casting of steel neglecting heat conduction along the casting direction. The energy equation describing the continuous casting process used in their work is

$$\rho c v_{cast} \frac{\partial T}{\partial z} = \frac{\partial}{\partial x}\left(k_{\text{eff}} \frac{\partial T}{\partial x} \right) + \frac{\partial}{\partial y}\left(k_{\text{eff}} \frac{\partial T}{\partial y} \right) + S \tag{2.1}$$

where

$$\rho c = g_l \rho_l c_l + g_s \rho_s c_s$$

$$k_{\text{eff}} = \left[k_s g_s + k_l g_l \right]\left[1 + \omega g_l^2 \right]$$

$$S = v_{cast} \frac{\partial \left(g_s \rho_s \right)}{\partial z}\left[L + \left(c_l - c_s \right)\left(T - T_{ref} \right) \right]$$

where x and y are coordinates along width and thickness direction respectively, z is the coordinate along length (casting direction), T is temperature, v_{cast} is the casting speed, ρ is density, L is latent heat, c is specific heat, k_{eff} is effective thermal conductivity, T_{ref} is a reference temperature, ω is a thermal conduction enhancement factor, S is the energy source term, and subscripts "l" and "s" denote liquid and solid phase, respectively.

Their model featured the calculation of realistic spray cooling pattern such that issues of spray distribution and overlap can be investigated by modeling each spray nozzle used in the caster according to information provided by the caster operators. The spray nozzle information provided by the caster operators includes: the positions of the nozzles across (width direction) and along the strand (casting direction), the nozzle type, the fan angle and distribution of the spray flux from each nozzle, the distance of the nozzle from the slab surface, and the spray water temperature. The spray water of each nozzle is mapped onto the slab surface to mimic a real spray water pattern. An example of the resulting spray cooling pattern is shown in Figure 2.4. By parametric study and calibration, the following correlation of the heat transfer coefficient, h_{spray}, due to water cooling is used:

$$h_{spray} = \frac{1570.0 w^{0.55}\left[1 - 0.0075\left(T_{spray} - 273.15 \right) \right]}{\alpha} \tag{2.2}$$

where w is the spray cooling flux, T_{spray} is the temperature of the spray cooling water and α is a machine dependent calibration factor. For the bottom surface, the coefficient is

modified to include the effect of plate orientation by multiplying the expression for the top surface by $(1-0.15\cos\theta)$, where θ is the slab surface angle from horizontal. The solid fraction-temperature relationship during solidification is determined from a microsegregation model [39] that simultaneously solved with Equation 2.1. The model is proved to be ideal for optimizing caster operation, for example, adjustment of spray pattern, water flow rates, casting speed, etc.

Remarks

In continuous casting process simulation, instead of direct coupling between temperature field and fluid convection, a thermal conductivity enhancement factor is used. The thermal field models in current available literatures neglect solid deformation. To predict more accurate temperature and solid fraction fields, energy transport due to fluid flow and solid movement have to be considered. The boundary conditions play an important role in the prediction of temperature and solid fraction field. A good microsegregation model for solid fraction-temperature relationship is also essential.

2.3 Fluid Flow

Knowledge of multiphase fluid flow has increased significantly in the past few decades. Mehrabian *et al* .[40] were the first to introduce Darcy's law in the context of fluid flow in solidification. In their work, the energy equation was decoupled from the momentum equation and the temperature profile was required as an input. Fujii [41] extended the work by Mehrabian and for the first time that the momentum equation (Darcy's law) and energy equation were solved simultaneously in the mushy zone. However, during this infant stage, the fluid flow in the pure liquid area was not considered.

The multi-domain method was proposed to couple the fluid flow in the mushy zone and bulk liquid zone [42-44]. Since the fluid flow in bulk liquid and porous media are described by different equations (Navier-stokes equations for bulk liquid and Darcy's

law for the mushy zone), in the multi-domain approach, the momentum equation for mushy zone and bulk liquid were written and solved separately, but coupled through certain interfacial conditions.

Two methods were proposed to deal with the difficulty of different natures of the flow in liquid and mushy zone and more importantly to incorporate more physics of solidification. The first one is the mixture theory [21, 45] and the second one is based on the idea of volume-averaged method [46].

The second approach is more sophisticated but has greater insight into the physics relating the macroscopic and microscopic phenomena. The continuity equation and the momentum equation derived using the volume-averaged method from the reference [46] are listed below.

Continuity equation

$$\frac{\partial}{\partial t}\left(g_i \rho_i\right) + \nabla \cdot \left(g_i \rho_i \left\langle \mathbf{v}_i \right\rangle^i\right) = \Gamma_i \tag{2.3}$$

Momentum equation

$$\begin{aligned}\frac{\partial}{\partial t}\left(g_i \rho_i \left\langle \mathbf{v}_i \right\rangle^i\right) + \nabla \cdot \left(g_i \rho_i \left\langle \mathbf{v}_i \right\rangle^i \left\langle \mathbf{v}_i \right\rangle^i\right) = -\nabla\left(g_i \left\langle p_i \right\rangle^i\right) + \nabla \cdot \left(\left\langle \boldsymbol{\tau}_i \right\rangle + \left\langle \boldsymbol{\tau}_i \right\rangle^t\right) \\ + \mathbf{M}_i + g_i \left\langle \mathbf{b}_i \right\rangle^i\end{aligned} \tag{2.4}$$

where $\mathbf{v}_i$ is the velocity vector of phase i , Γ_i is the interfacial mass transfer due to phase change, $\mathbf{M}_i$ is the interfacial momentum transfer, $\mathbf{b}$ is the body force vector, $\left\langle \boldsymbol{\tau}_i \right\rangle$ is the macroscopic viscous stress, $\left\langle \boldsymbol{\tau}_i \right\rangle^t$ is the dispersive flux. In Equation 2.4, $\left\langle \phi_i \right\rangle$ is the volume average of some quantity ϕ in phase i defined as

$$\left\langle \phi_i \right\rangle = \frac{1}{V_0}\int_{V_0} X_i \phi_i dV \tag{2.5}$$

where V_0 is the volume of representative control volume and X_i is a phase function, being one in phase i and zero otherwise. The $\left\langle \phi_i \right\rangle^i$ term represents the intrinsic volume average of some quantity ϕ defined as

$$\langle \phi_i \rangle^i = \frac{1}{V_i} \int_{V_i} X_i \phi_i dV \tag{2.6}$$

where V_i is the volume of phase i.

In Equation 2.4, viscous stress is modeled as

$$\langle \boldsymbol{\tau}_i \rangle = \mu_i^* \left\{ \nabla \left(g_i \langle \mathbf{v}_i \rangle^i \right) + \left[\nabla \left(g_i \langle \mathbf{v}_i \rangle^i \right) \right]^T - \langle \mathbf{v}_s \rangle^s \nabla g_i - \nabla g_i \langle \mathbf{v}_s \rangle^s \right\} \tag{2.7}$$

where μ_i^* is a macroscopic or effective viscosity. The dispersive flux $\langle \boldsymbol{\tau}_i \rangle^t$ is the treated as negligible for laminar flow.

$\mathbf{M}_i$ is the interfacial momentum transfer due to phase change, interfacial stresses and other transfers. According to Ni and Beckermann [46]

$$\mathbf{M}_i = \mathbf{M}_i^d + \mathbf{M}_i^p \tag{2.8}$$

where the first term on the right hand side is the contribution of deviatoric stresses and the second one is the isotropic part. It is obvious that

$$\mathbf{M}_l^d + \mathbf{M}_s^d = 0 \text{ and } \mathbf{M}_l^p + \mathbf{M}_s^p = 0 \tag{2.9}$$

It is assumed that the pressure equilibrium is reached instantaneously. Therefore, $\mathbf{M}_i^p$ can be expressed as [46]

$$\mathbf{M}_s^p = -\mathbf{M}_l^p = -p_l \nabla g_l = p_l \nabla g_s \tag{2.10}$$

The dissipative terms $\mathbf{M}_i^d$ can be determined by assuming the mushy zone as a porous media. In analogy with the Darcy's law

$$\mathbf{M}_l^d = -\mathbf{M}_s^d = -g_l^2 \mu_l \left(\mathbf{K}^{[2]} \right)^{-1} \left(\langle \mathbf{v}_l \rangle^l - \langle \mathbf{v}_s \rangle^s \right) \tag{2.11}$$

where $\mathbf{K}^{[2]}$ is a second order symmetric permeability tensor. As indicated by the experimental study, the mushy zone can be treated as an isotropic porous media, and then the permeability can be well described as a scalar function K. Many relations [47, 48] are in use. One commonly used is the Carman-Kozeny relation [49]

$$K = \frac{(1-g_s)^3}{g_s^2} \frac{\lambda^2}{180} \tag{2.12}$$

where λ is a representative length scale of the dendrite structure [50].

It is clear that the model based on volume-averaged method is a true-two velocity model which allows the liquid flow with the presence of both solidification and solid phase deformation. It is a single domain model allows us to simulate the fluid flow in both bulk liquid and mushy zone at the same time.

2.4 Solid Deformation

In continuous casting, thermal-mechanical behavior of solid phase is essential to the quality of the final product. Solid deformation is directly linked to gap formation in the mold region [51], stress, and cracks (surface or internal cracks) [52], bulging between supporting rolls [53], centerline macrosegregation [2, 54, 55], and final size of the product. An accurate solid deformation is guaranteed only when the following are considered: solid-liquid interaction, creep behavior of mushy zone and solid shell, the loading history and a coupled thermal-mechanical calculation. Usually, the thermal field and the solid deformation are calculated sequentially and iterated to obtain a self-consistent solution, i.e., thermal and stress analysis are iteratively coupled to consider feedback. The liquid phase and mushy zone are more often substituted by a pressure boundary.

There are many mathematical models investigating the thermal stress during the continuous casting of steel, including models for billet [56-59], beam blank [60], slab [61, 62] and thin-slab casting [63, 64]. Brimacombe and coworkers [65, 66] were the first to apply a transverse two-dimensional billet section under plane stress as it moves down the caster. Due to lack of material properties at elevated temperature, only simple elastic or plastic constitutive models were used. Rammerstrofer *et al.* [62] considered the creep and relaxation in developing of a thermo-visco-elastic-plastic stress model for a one-dimensional domain running down the mid-width plane of a slab. Kristiansson [67] and Boehmer and co-workers [57] proposed two-dimensional transverse-cross-slice models that coupled the thermal and mechanical calculation. Pascon [68] had extended the slice

model by assuming a state of generalized plane strain and was able to cope with the bending and unbending of the strand. The 2D calculation domain for these transverse slice models is shown in Figure 2.5.a). The liquid region and mushy zone are stripped off from the finite element mesh and replaced with a ferrostatic pressure boundary. The slice run through the strand domain and the mechanical stress is calculated either coupled or uncoupled with the thermal analysis. The stress and strain at time t are the sum of former values at time $(t-\Delta t)$ and the increment values for the past time interval Δt. The transverse-slice models neglect the compatibility between successive slices and thus were not able to deal with complex deformation such as bulging.

Inoue *et al.* [61] used finite element method to calculate the steady state two-dimensional bulging during a vertical continuous casting slab using the entire longitudinal cross section from the mid-width plane as the calculation domain, which is shown in Figure 2.5.b). Their model featured a material constitutive model capable to describe both elastic-viscoplastic solid behavior and the viscous fluid flow, thus the calculation domain include the solid, liquid and mushy zone. Grill and Schwerdtfeger [69] were the first to consider the effect of creep on a moving longitudinal section to predict bulging in the continuous casting process. Their calculation domain, as shown in Figure 2.5.c), is the solid shell from the mid-width slice between two successive rolls and the liquid and mushy zone are removed. During each small movement in a short interval along casting direction, the elastic deformation is assumed to be stationary and only deformation due to creep is transferred to the downstream material.

The methods used by Boehmer and co-workers [57] and Grill and Schwerdtfeger [69] can be referred to as "non-steady state slice methods". They are able to provide valuable information for bulging deformation, however, have their limitations. To limit the number of unknowns, the slice methods consider only a portion of entire physical domain conveyed along casting direction to record the deformation history. The boundary conditions are based on unrealistic assumptions and the result cannot be accurate. And if

the length of the calculation domain is too small, these slice models cannot be used to predict bulging.

Bellet and coworkers [71, 72] proposed a Global Non Steady-state (GNS) approach which overcomes the limitations of traditional non-steady state slice methods and allows more accurate prediction of bulging. This approach features, firstly, a hybrid liquid-solid constitutive model which includes a description of the behavior of the bulk liquid zone and allows a global calculation; secondly, partially remeshing of the growing domain. The key point of this approach is the management of the mesh. As shown in Figure 2.6, only the first row grid is fixed in space. All other grids are shifting downward with casting speed. In this way, the calculation domain is growing corresponding to the increasing length of the physical strand. Since the shifting of the grid point below the upper surface elongates the mesh near the surface, to avoid degeneracy, remeshing is required. It should be noticed that, only the mesh near the top surface is affected by the grid transport, remeshing is only necessary for the distorted mesh. During the remeshing, new grid points are generated. They pointed out that the grid transportation might generate significant error and thus add an additional "buffer zone" on the top of the actual meniscus. This approach is close to a physical continuous casting process and can be easily extended to three-dimensional calculation. Above solidus temperature, a pure thermo-viscoplastic model was used to describe the deformation behavior of mushy zone and pure liquid; below solidus temperature, a thermo-elastic-viscoplastic model is used to represent the behavior of solid phase. To predict bulging and air gap formation, the model needs the ability to deal with contact problems. They assumed the mold and rolls to be rigid confinements. The contact boundary condition of the cast product with either the muld or supporting rolls is defined as

$$\begin{cases} \boldsymbol{\sigma}\vec{n}\cdot\vec{n} \le 0 \\ d \ge 0 \\ \left(\boldsymbol{\sigma}\vec{n}\cdot\vec{n}\right) d = 0 \end{cases} \tag{2.13}$$

where σ is the Cauchy stress tensor, d is a signed distance to the obstacle (≥ 0 for no penetration), $\vec{n}$ is the local outward normal vector on the cast product surface. The fulfillment of this contact condition is done with a penalty method which applies a repulsive normal stress vector when penetration occurs [71]. Their model was used to study the air gap formation in the mold and bending strain [56] and the computational results are in good agreement with the experiments.

2.5 Porosity

For most cases, it is not practical to observe porosity *in-situ* practically in an industrial casting. So mathematical modeling is the only tool available. As long as a mathematical model about porosity formation is constructed, an industrial practitioner can calculate when porosity forms and its size and distribution. This helps people choose better operating conditions to minimize pore defects in advance.

For the last few decades, considerable effort has been made to predict the porosity nucleation and growth. Those models include analytical models, criterion functions and complex numerical models. Lee [73] had described a standard that an ideal porosity prediction model should satisfy. However, due to the complexity, all available models consider only some aspects of the problem while taking some other effects as negligibly small. In this section, a short review of available porosity studies is presented. To the author's knowledge, there is no quantitative work available for porosity formation due to solid deformation in the continuous casting process.

2.5.1 Analytical Models

Analytical models are either exact mathematical solutions or approximate solutions using asymptotic analysis. The analytical models apply to idealized physical system with simplifying assumptions. Historically, the analytical models were proposed to solve porosity due to shrinkage. The formation of a single centerline pore in a long tube solidifying in the radial direction for pure metal has been investigated by many

researchers. The schematic diagram of the problem is given in Figure 2.7.a). Walther *et al.* [74] proposed that the pressure drop of the laminar flow could be calculated based on the assumption that the flow through the dendrites is analogous to flow through a pipe which can be described by Hagen-Poiseuille equation. If the metal is pure and the solidification rate is low, the center tube will have a smooth surface, the pressure drop is given by

$$\Delta p = \frac{\rho}{g}\frac{64\beta a^4 L^2}{r^4}\left(\frac{1}{2}+\frac{\beta fL}{3r}\right) \tag{2.14}$$

where Δp (Pa) is the pressure drop of liquid phase, g (m/s^2) is acceleration due to gravity, L (m) is the length of the casting, r (m) is the radius of the liquid center core, a is a constant value, β is the volumetric change due to solidification, ρ (kg/m^3) is material density and f is a friction factor. The porosity is assumed to form when the pressure drop reach a critical value. And once formed it will occupy all the volume previous present with liquid. Piwonka and Flemings [75] extended this work to the solidification of a long cylinder of alloy with dendrite structure which is shown in Figure 2.7.b). They revised Equation 2.14 by suggesting that the cylinder can be replaced by a bundle of n tubes, where n is the reciprocal of the square of the primary dendrite arm spacing, λ_1. With this assumption, an additional parameter, the tortuosity factor, ζ is used to compensate for the liquid flow channels not being straight. The pressure drop is then

$$\Delta p = p_a - p_l = \frac{32\mu\beta c^2 L^2}{r^4}\left(\frac{\zeta^2}{\pi R^2 n}\right) \tag{2.15}$$

where p_a (Pa) is the ambient pressure, p_l (Pa) is the metallic pressure at L (the end of the cylinder), μ (kg•m^{-1}•s^{-1}) is the viscosity, c is a constant, n is the number of liquid channel per unit cross section of the cylinder, r (m) is the radius of liquid channel, R (m) is the radius of the cylinder. When the pressure drop reaches a critical value the pore form and grows to a radius of r (radius of liquid channel). They found that the pore size of this result is under-predicted comparing to experimental results. To get a better fit,

they included the effect of dissolved gas on the pressure at which pore will form then they predicted more reasonable result. The limitation of these analytical models is that they are only applied to solidification with very simple configuration.

2.5.2 Criteria Functions

The Niyama criterion is the most famous criterion function of porosity formation. Niyama *et al.* [76] showed that the temperature gradient can be an effective parameter to predict shrinkage. They [77] concluded that porosity is most likely to form where the following relation is satisfied

$$G/\sqrt{\dot{T}} < constant, \tag{2.16}$$

where G (K cm^{-1}) is the thermal gradient and $\dot{T}$ (K min^{-1}) is the cooling rate. The right-hand-side constant value depends on the alloy being cast. For steel casting, the constant is $1\left(\mathrm{K}^{1/2}\,\mathrm{min}^{1/2}\,\mathrm{cm}^{-1}\right)$. This criterion is also used for other alloys but with the constant being different values.

Another criterion is proposed by Hansen and Sahm [78]. They used a more complex function

$$G/\left[\dot{T}^{1/4}v_l^{1/2}\right] < constant, \tag{2.17}$$

where v_l is the flow velocity through the mushy zone. This criterion is more complicated than Niyama criterion, because the flow velocity is needed.

There are other criteria functions [79]. The criteria functions are used to predict where there is a higher probability for pore to present; however, the criteria functions do not represent the physics and are not quantitative tools for calculation of fraction or size of the porosity. According to their derivation, criteria functions only predict the possibility of shrinkage porosity. The criterion functions are highly dependent on the materials and casting conditions. Lots of experiments need to be done to provide data to find proper constants in the criteria functions. So, the usage of criteria functions is limited.

2.5.3 Models Based on Darcy's Law

The basic assumptions in the group of Darcy's law approaches are: 1), the melt is a Newtonian fluid and flow through mushy zone is creeping flow; 2), convective transport of energy is neglected, which means that the energy is uncoupled from fluid motion. Kubo and Pehlke [80] were the first to report such model. The temperature result gives fraction liquid that will be used. They combine Darcy's law (Equation 2.18) with the continuity Equation 2.19

$$\mathbf{v}_l = -\frac{K}{\mu g_l}\left(\nabla p_l - \rho \bar{\mathbf{g}}\right) \tag{2.18}$$

$$\left(\frac{\rho_s}{\rho_l} - 1\right)\frac{\partial g_l}{\partial t} - \frac{\partial g_l v_{l,x}}{\partial x} - \frac{\partial g_l v_{l,y}}{\partial y} + \frac{\partial g_p}{\partial t} = 0 \tag{2.19}$$

where $\mathbf{v}_l$ is liquid velocity vector, $v_{l,x}$ and $v_{l,y}$ are liquid velocity components in x and y direction respectively, K is the permeability of the mushy zone, μ is dynamic viscosity, $\rho_{i(i=s,l)}$ is density of phase i, $g_{i(i=p,l)}$ is the volume fraction of phase i, x and y are coordinates, t is time. To consider the effect of gas content, they first relate the liquid pressure p_l to the pore phase pressure p_p by

$$p_l = p_p - \frac{2\gamma_{lg}}{R_p} \tag{2.20}$$

where γ_{lg} is the liquid-gas interfacial energy and R_p is the radius of the pore phase, p_l and p_p are the pressures in liquid and pore phase, respectively. The radius of the pore phase is assumed to be the same as the dendrite size.

Consider the main origin of gas content in steel is CO gas, the gas pressure of CO is

$$p_p = [C_l][O_l] / K_{CO} \tag{2.21}$$

Assuming complete equilibrium, the mass balance of carbon and oxygen can be expressed by

$$\left[C_0\right] = g_s\left[C_s\right] + g_l\left[C_l\right] + \alpha_c \frac{p_p g_p}{T} \tag{2.22}$$

$$\left[O_0\right] = g_s\left[O_s\right] + g_l\left[O_l\right] + \alpha_o \frac{p_p g_p}{T} + a\Delta SiO_2 \tag{2.23}$$

with

$$\left[C_s\right] = k_{Fe-C}\left[C_l\right] \text{ and } \left[O_s\right] = k_{Fe-O}\left[O_l\right],$$

where p_p is pressure of pore phase, $\left[C_0\right]$ and $\left[O_0\right]$ are the initial concentration of carbon and oxygen, $\left[C_i\right]$ and $\left[O_i\right]$ are carbon and oxygen content in phase "i" (i= 's' for solid or 'l' for liquid), K_{CO} is an equilibrium constant, $\alpha_c = \left(0.146/\left(g_l\rho_l + g_s\rho_s\right)\right)$ and $\alpha_o = \left(0.390/\left(g_l\rho_l + g_s\rho_s\right)\right)$, a is a constant and ΔSiO_2 is content of deoxidation product by silicon, k_{Fe-C} and k_{Fe-O} are the equilibrium partition ratio of carbon and oxygen in steel, respectively.

At first, $\partial g_l / \partial t$ is calculated from the temperature result for each volume element. If the volume element is in the mushy zone, the porosity is calculated in the following manner.

If no porosity has formed, liquid pressure is calculated from Equation 2.18 and 2.19 assuming no occurrence of porosity using explicit method. Gas pressure is calculated from Equation 2.20 by assuming the diameter of the pore is the same as the dendrite cell size. A new amount of porosity is calculated from Equation 2.21 through 2.23. When porosity has already formed, the interdendritic flow is calculated using explicit finite difference from Equation 2.18 and 2.19. If the interdendritic flow is positive, liquid pressure is calculated from Equation 2.18 and 2.19 using gas porosity from last step. The porosity is then updated from Equation 2.21 through 2.23. If interdendritic flow velocity is negative, new porosity is calculated from Equation 2.18 and 2.19 using pressure value from last step. Then, pressure is updated using Equation 2.22 and 2.23. When g_p and p_l become negative, they are forced to be zero. When the increase of porosity becomes greater than liquid fraction, it is set to be equal to the liquid

fraction. Their results for percentage porosity were logical and they claimed good qualitative agreement with experiments.

There are many papers published similar to this approach [81-83]. However, currently there is no quantitative work published on prediction of porosity due to solid deformation. So, to predict porosity in continuous casting of steel, new models need to be derived.

2.6 Macrosegregation

Macrosegregation calculation is still a challenge for two reasons: firstly, it is difficult to maintain the mass balance; secondly, macrosegregation has various origins (shrinkage, forced/shrinkage convection, free dendrite sedimentation, solid deformation).

The first few papers published on the calculation of macrosegregation were from Flemings and his coworkers [40, 84] during late 1960s. In their work, they neglected the transport of the solid phase, and diffusion in the liquid phase was not considered. Thus, only fluid flow due to solidification shrinkage was considered. Instead of positive centerline segregation, Flemings found a negative one. Hence, he concluded that the density change upon solidification is not the main cause of the centerline segregation. Since Flemings work ruled out the possibility of shrinkage flow as the cause of centerline macrosegregation, Miyazawa *et al.* [2] studied the influence of solid deformation due to supporting rolls. He expressed the solid shell surface velocity as a function of casting speed, maximum slab surface deflection and roll spacing; the calculated surface velocity is interpolated to the inner mushy zone to get solid velocity in the mushy zone. Based on this prescribed solid deformation, fluid flow and macrosegregation were calculated. Miyazawa was the first one to achieve a good agreement between numerical prediction and experimental results. Following Miyazawas's work, Kajitani *et al.* [85] proposed a similar numerical model with strong assumption on the solid phase motion.

In the case of continuous casting of billets and bloom, there are only a few supporting rolls, Janssen *et al.* [86] consider the thermal/internal deformation other than the mechanical/external deformation as considered by Miyazawa to be the main cause of macrosegregation. They assumed that the inner part shrinks significantly. Since the inner and outer parts are connected, the inner part shrinks towards the outer part resulting in the composition enriched liquid flow toward center line and cause a high concentration there. To account for solid deformation due to shrinkage, the bloom was divided into four zones and each of them deform in its own way. With this solid deformation field known, the liquid flow is calculated and furthermore the macrosegregation is obtained using mass balance equation.

A simple slice model for estimating the macrosegregation in continuously cast strand has been reported by I Vušanović [87]. The main feature of the model is its simplicity which allows it to be used in the on-line mode. The macroscopic model is based on continuum mixture theory, while the microsegregation model is based on the Scheil rule. Instead of direct calculation of liquid velocity, the fluid flow effects on the species transportation have been approximated by the increased solute diffusivity in the liquid phase within the slice. Their model is able to predict the qualitative features of the macrosegregation pattern.

The earlier models either neglect solid deformation or the solid velocity is calculated based on reasonable assumed deformation pattern. None of them predicts solid deformation using thermal mechanical model. As has been discussed in section 2.4, the most advanced solid deformation model is by Bellet and coworkers, so the prediction of macrosegregation in their work [88] should be more reliable.

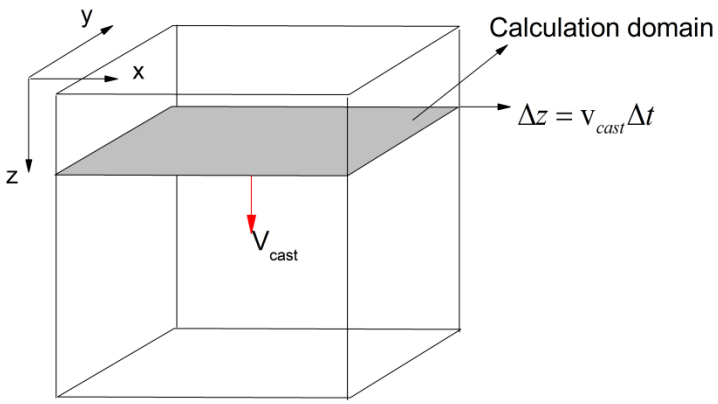

Figure 2.1 Schematic diagram of the coordinate system and calculation domain for transverse slice method [29, 30].

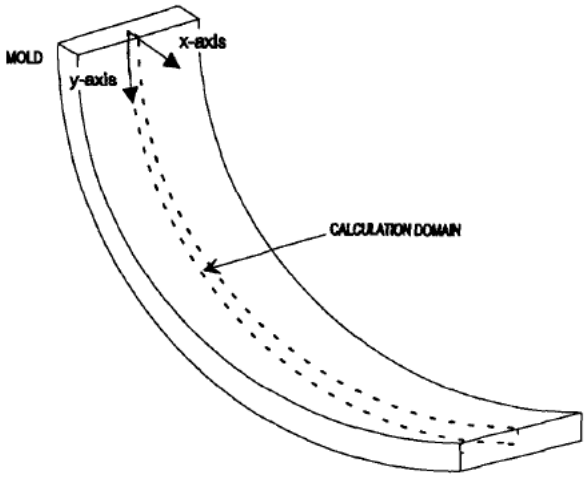

Figure 2.2 Schematic diagram of the calculation domain for longitudinal slice method used in reference [31, 89].

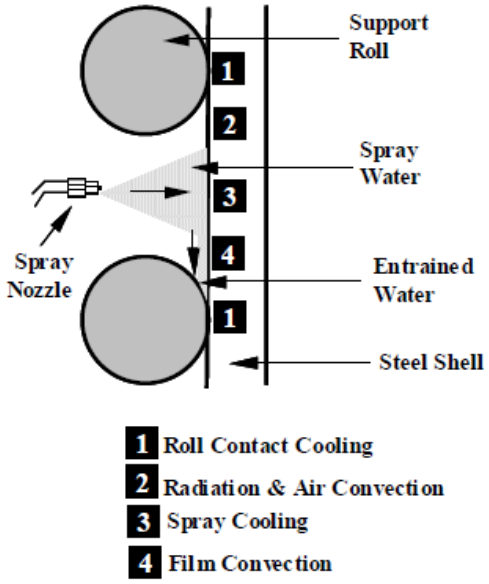

Figure 2.3 Typical boundary conditions for temperature calculation. The heat transfer coefficient in each area is an averaged value over the area surface [90].

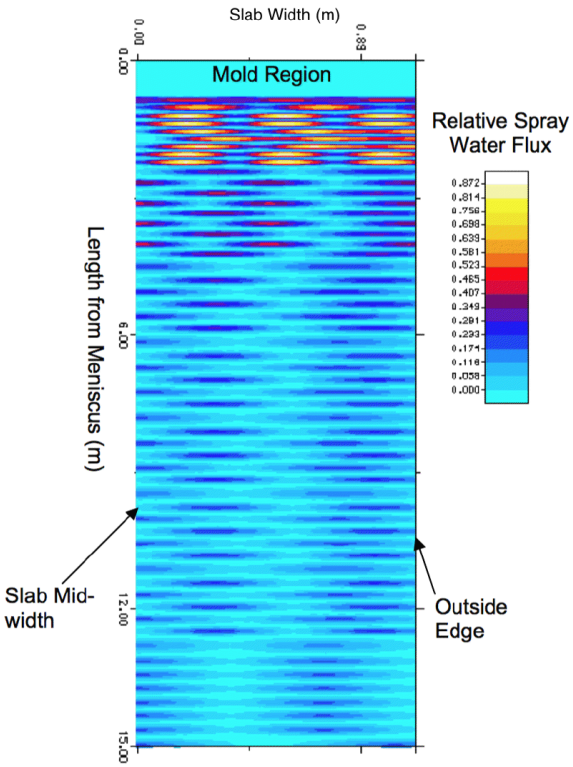

Figure 2.4 Relative secondary spray cooling water flux (spray flux on surface divided by maximum spray flux) for half of slab width from 0 to 15 m from meniscus. Spray is symmetric about mid-width of slab [38].

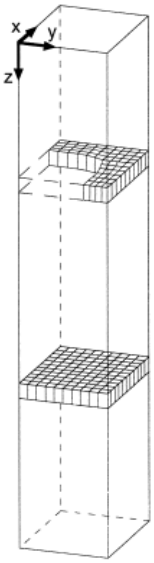

a) Calculation domain of transverse-slice method [68].

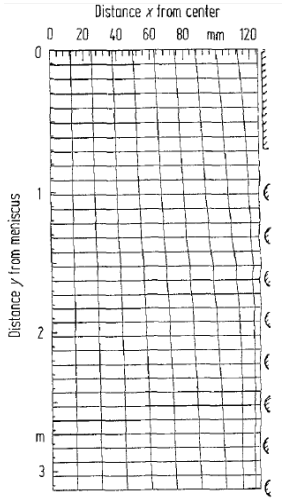

b) Calculation domain (grid area) of longitudinal-slice method used in [61].

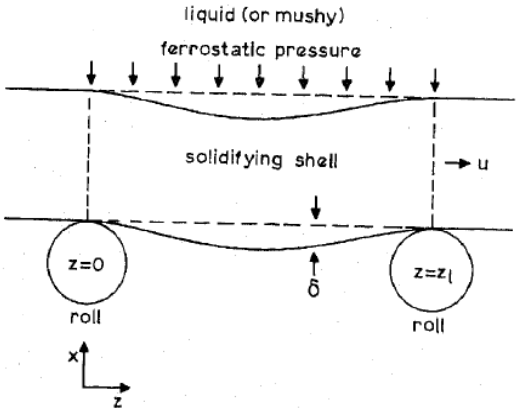

c) Calculation domain (between the dash-lines) of longitudinal-slice method [69].

Figure 2.5 Calculation domains of different slice models.

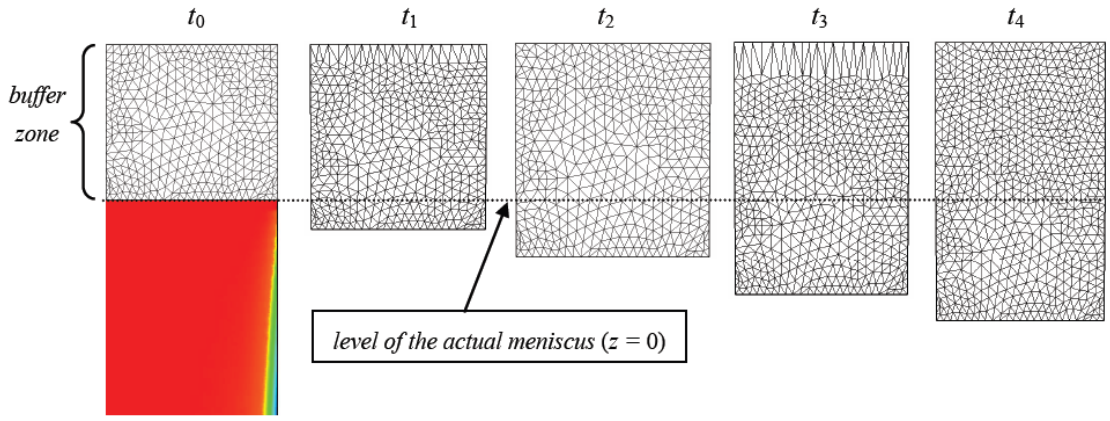

Figure 2.6 Schematic of mesh growing process. At time t_0, the mesh occupies the buffer zone on the top of the actual meniscus. At t_1, the grid points below the top surface shift down. The mesh elongation of the first row below the top surface can be seen. Remeshing is performed at t_2. This growing-remeshing consequence is repeated [71].

a)

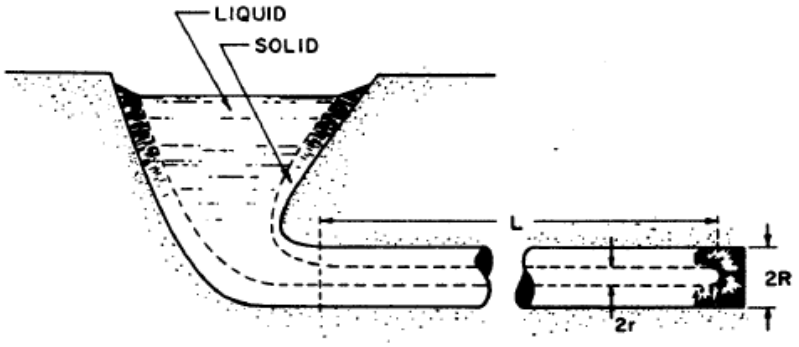

b)

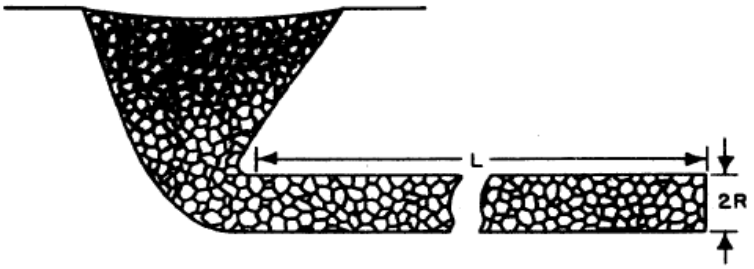

Figure 2.7 Sketch of solidification of a long cylinder of pure metal (Top) and "mushy" freezing alloy (Bottom) [75].

CHAPTER III

MATHEMATICAL MODEL

3.1 Introduction

The aim of formulating a mathematical model is to get a better understanding of the different physical phenomena, their interaction and the influence. For our case, numerical simulation is a powerful tool that gives us more insight into the porosity and macrosegregation dependencies on the operating parameters. In this chapter, the mathematical model for porosity and macrosegregation will be presented in detail. Concerning the available work in the literature, porosity formations and macrosegregation in continuous casting are mostly in two dimensional. And most importantly, as emphasized in Chapter II, there is no available mathematical model on the calculation of porosity considering the solid phase deformation. For macrosegregation, presence of porosity is always neglected. Here in this work, porosity and macrosegregation due to both shrinkage effect and solid deformation are modeled.

3.2 Model Derivation

A schematic diagram of the continuous casting of steel slab is shown in Figure 3.1.a). The geometric parameter θ describing the curve of the strand is illustrated in Figure 3.1.b). The geometric parameter θ is defined as the angle between the tangent of the strand and the vertical direction. The physical strand is mapped onto a regular cuboid domain which is shown in Figure 3.2. Even though solid metal is continuously being withdrawn from the bottom at a constant speed during the continuous casting process, the temperature field and the interfaces (solid-mush and liquid-mush interfaces) are in steady-states relative to an observer standing aside. Given this steady state nature, the continuous casting process can be modeled with a steady model and thus the time derivative terms in the governing equations are neglected. Current model assumes that

the temperature, the solid fraction and the pore-free material density field are read-in values from temperature simulation.

3.2.1 Mass Conservation

Consider a representative volume element composed of any possible combination of solid phase (*s*), liquid phase (*l*) and porosity (*p*), such that the volume fractions of the three phases satisfy $g_s + g_l + g_p = 1$. It is assumed that the density of pore is negligible. The continuity equation is given by

$$\nabla \cdot \left(\rho_l g_l \mathbf{v}_l + \rho_s g_s \mathbf{v}_s \right) = 0 \tag{3.1}$$

where ρ_i is material density, g_i is the volume fraction of the phases and $\mathbf{v}_i$ is the velocity vector, with subscript '*i*' denoting phase *i* (*i*=*l* for liquid, *i*=s for solid and *i*=p for porosity). Note that the $\nabla \cdot \left(\rho_l g_l \mathbf{v}_l \right)$ term represents the material feeding/extraction due to liquid flow and the $\nabla \cdot \left(\rho_s g_s \mathbf{v}_s \right)$ term represents the material feeding/extraction due to solid phase movement (by tensile or compression stress). The porosity terms are not presented in this continuity equation because the density of porosity is negligible. To avoid porosity, the void due to density change must be compensated by the inward liquid flow or solid compression. With applied tensile stress, the interdendritic liquid flow must compensate extra volume to avoid porosity. Once the liquid feeding fails, the pore phase nucleates and grows due to solidification shrinkage and furthermore solid deformation.

By replacing the solid density with the mixture density in Equation 3.1, the following form of continuity equation is obtained

$$\nabla \cdot \left(\rho_l \, g_l \mathbf{v}_{rel} + \rho_m \mathbf{v}_s - \rho_l \, g_p \mathbf{v}_s \right) = 0 \tag{3. 2}$$

where ρ_m is the porosity-free mixture density and $\mathbf{v}_{rel} = \left(\mathbf{v}_l - \mathbf{v}_s \right)$ is the relative velocity.

It is further assumed that, the liquid density is a constant value at liquidus temperature, such that $\rho_l = \rho_l \left(T_{liquidus} \right)$. Equation 3.2 is rewritten as

$$\nabla \cdot \left[g_l \mathbf{v}_{rel} \right] = -\frac{1}{\rho_l} \nabla \cdot \left[\rho_m \mathbf{v}_s - \rho_l g_p \mathbf{v}_s \right] \quad (3.2)'$$

Assume that the relative velocity only exists where the where $g_p = 0$, then the continuity equation can be further simplified as

$$\nabla \cdot \left[g_l \mathbf{v}_{rel} \right] = -\frac{1}{\rho_l} \nabla \cdot \left[\rho_m \mathbf{v}_s \right] \quad (3.3)$$

3.2.2 Pressure and Relative Velocity Equation

Consider the liquid flow in continuous casting as steady state creeping flow, the liquid momentum equation can be expressed as

$$0 = -g_l \nabla p + g_l \rho_l \mathbf{g} - g_l^{\,2} \mu_l K^{-1} \left(\mathbf{v}_l - \mathbf{v}_s \right) \quad (3.4)$$

which can also be written as

$$0 = -\nabla p + \rho_l \mathbf{g} - g_l \mu_l K^{-1} \mathbf{v}_{rel} \quad (3.4)'$$

where p is liquid pressure, K is the permeability, μ_l is the dynamic viscosity of liquid phase, $\mathbf{g}$ is the gravitational acceleration vector. The permeability, K, is the measurement of the flow conductance of a porous medium and is given by the Kozeny-Carman correlation [91] as

$$K = K_0 g_l^3 / (1 - g_l)^2 \quad (3.5)$$

where $K_0 = \lambda_2^2 / 180$, in which λ_2 is the secondary dendrite arm spacing (SDAS). The SDAS is given by [92]

$$\lambda_2(\mu m) = \begin{cases} (-169.1 - 720.9 \cdot C_c) \cdot T_c^{-0.4935} & 0 < C_c \le 0.15 \\ 143.9 \cdot T_c^{-0.3616} \cdot C_c^{(0.5501 - 1.996 C_c)} & 0.15 < C_c \end{cases} \quad (3.6)$$

where $T_c \left({}^{o}C / s \right)$ is average cooling rate in the mushy zone, $C_c \left(wt\% \right)$ is the weight percentage of carbon content. When the solid fraction is below 0.01, the permeability obtained by substituting 0.01 into Equation 3.5 is used and when the solid fraction is higher than 0.99, the permeability is set to the value obtained by substituting 0.99.

To take into the contribution of the curved shape on the pressure field, the gravitational acceleration vector is now $\mathbf{g} = \left[-a \cdot \sin\theta, 0, a \cdot \cos\theta\right]^T$, with a =9.8m/s^2, where θ is the geometric parameter.

Comparing with the general volume-averaged momentum equaiton, three terms are neglected in Equation (3.4)': time dependent term (due to steady nature of continuous casting process), the convective term (flow in the continuous casting process is creeping flow with low Reynolds number) and the diffusion of momentum in the liquid phase (which is negligiable compared to the momentum dissipation due to interfacial forces).

By manipulating and combining the Equation 3.3 and (3.4)', the liquid phase pressure equation is derived as:

$$\nabla \cdot \left(\frac{K}{\mu_l} \nabla p \right) = \frac{1}{\rho_l} \nabla \cdot \left[\rho_m \mathbf{v}_s \right] + \nabla \cdot \left(\frac{K \rho_l \bar{g}}{\mu_l} \right) \tag{3.7}$$

This equation has only unknown, *i.e.*, liquid pressure. It can be solved by using finite difference scheme with proper boundary conditions.

Since the continuity equation and the pressure equation are valid throughout the calculation domain, the boundary conditions are only needed at the exterior boundaries. The boundary conditions for pressure calculation are given below:

At z = 0: $p = p_{atm}$ =1 bar (3.8)

Other boundaries: $\partial p / \partial \vec{n} = 0$ (3.9)

where $\vec{n}$ denotes the unit normal vector on the slab surfaces.

Shrinkage porosity and porosity due to solid deformation, which are assumed to be at zero pressure. So when porosity is present, the liquid pressure in equilibrium should also be zero. With Equation 3.7, the calculated pressure at the end of the mushy zone can be several GPa below zero. Then the large source term technique proposed by [93] is employed to force the pressure that lower than 0 Pa to be 0 Pa.

It should be noticed that once the pressure field is calculated, the relative velocity field is also known. When pressure is not zero, the relative velocity is simply given by

$$\mathbf{v}_{rel} = \frac{\nabla p - \rho_l \vec{g}}{-g_l \mu_l K^{-1}} \tag{3.10}$$

When the pressure is zero, porosity forms and the relative velocity is set to zero.

3.2.3 Porosity Equation

Once the pressure condition (p=0) for porosity formation is satisfied, the volume fraction of the pore phase can be calculated from the continuity Equation (3.2)' with zero relative velocity. The porosity equation is simply:

$$\nabla \cdot \left[g_p \mathbf{v}_s \right] = \frac{1}{\rho_l} \nabla \cdot \left[\rho_m \mathbf{v}_s \right] \tag{3.11}$$

For the region where pressure is positive, the porosity is forced to be zero. For the region where the solid fraction equals to one, the porosity no longer grows.

The porosity calculation is closed by the following boundary conditions:

At z = 0: g_p=0 (3.12)

Other boundaries: $\partial g_p / \partial \vec{n} = 0$ (3.13)

where $\vec{n}$ denotes the unit normal vector on the slab surfaces.

3.2.4 Solid Velocity

One term always assumed known, however remains to be specified, is the solid velocity $\mathbf{v}_s$. As discussed in Chapter II, the solid deformation has been well studied using finite element method. In current work, the methodology by Schwerdtfeger [2] is used with additional consideration about solid deformation due to the variable roll gap.

The surface of the billet is confined by the supporting rolls. The roll spacing information and roll distribution along length direction are read-in values from the actual machine design.

The total surface deflection of the slab is a combination of the deflection due to bulging (Figure 3.3.a)) and the deflection due to variable roll gap (Figure 3.3.b)) in such a way that

$$\delta = \delta_b + \delta_g = \frac{\delta_{max}}{2}\left[1-\cos\left(\frac{2\pi z'}{l_B}\right)\right] + \frac{x_a - x_b}{l_B} z' \tag{3.14}$$

where δ, δ_b, δ_g are the total surface deflection, the surface deflection due to bulging and the surface deflection due to variable roll gap, respectively; δ_{max}, z' and l_B denote the maximum value of bulging at the midpoint between two rolls, the distance from the upper roll and the distance between two rolls; x_a and x_b are half of the roll gap at any two successive roll 'a' and roll 'b'.

The x direction velocity (thickness direction) of the solid shell surface $v^*_{s,x}$ is expressed by

$$v^*_{s,x} = v_{cast}\frac{d\delta}{dz} \tag{3.15}$$

The x-component solid velocity anywhere inside of the mushy zone, $v_{s,x}$, is calculated by

$$\begin{cases} \text{If slab thickness increases:} & v_{s,x} = v^*_{s,x} \\ \text{If slab thickness decreases:} \begin{cases} v_{s,x} = v^*_{s,x}\dfrac{g_s - g_s^c}{1-g_s^c}; & \text{if } g_s^c \neq 0 \\ v_{s,x} = v^*_{s,x}; & \text{if } g_s^c = 0 \end{cases} \end{cases} \tag{3.16}$$

where g_s^c is the solid fraction on the mid-thickness plane.

3.2.5 Macrosegregation Equation

Only the macrosegregation of carbon is considered. Carbon is a fast diffusive species so it is assumed that there is no concentration gradient in each representative control volume (RCV) in liquid phase. The concentrations in solid and liquid phase within the same RCV are related by the equilibrium condition

$$C_s = C_s^* = \kappa C_l \tag{3.17}$$

where C_s^* is the concentration on the solid-liquid interface, κ is the partition coefficient.

The mass balance of carbon content is given by:

$$\nabla \cdot \left(\rho_l g_l C_l \mathbf{v}_l + \rho_s g_s C_s \mathbf{v}_s \right) = 0 \tag{3.18}$$

Since the mixture density is defined as $\rho_m = \rho_l g_l + \rho_s g_s$ and with the definition $\mathbf{v}_{rel} = \left(\mathbf{v}_l - \mathbf{v}_s \right)$, Equation 3.18 written in terms of mixture density and relative velocity is:

$$\nabla \cdot \left(\rho_l g_l \mathbf{v}_{rel} + \left(\rho_m \kappa + \rho_l g_l \left(1 - \kappa \right) \right) \mathbf{v}_s \right) C_l = 0 \tag{3.19}$$

Define the mixture carbon content as

$$C_{mix} = \left(\rho_l g_l C_l + \rho_s g_s C_s \right) / \rho_m \tag{3.20}$$

Substitute Equation 3.17 into Equation 3.20 and rearrange to express C_l with C_{mix}:

$$C_l = \frac{\rho_m}{\rho_l g_l + \rho_s g_s \kappa} C_{mix} = \frac{\rho_m}{\rho_m \kappa + \rho_l g_l \left(1 - \kappa \right)} C_{mix} \tag{3.21}$$

By substituting Equation 3.21 into Equation 3.19, the final macrosegregation equation for carbon is derived:

$$\nabla \cdot \frac{\left(\rho_l g_l \mathbf{v}_{rel} + \left(\rho_m \kappa + \rho_l g_l \left(1 - \kappa \right) \right) \mathbf{v}_s \right) \rho_m}{\rho_m \kappa + \rho_l g_l \left(1 - \kappa \right)} C_{mix} = 0 \tag{3.22}$$

Or

$$\nabla \cdot \left(\mathbf{M} C_{mix} \right) = 0 \tag{3.23}$$

where $\mathbf{M} = \dfrac{\left(\rho_l g_l \mathbf{v}_{rel} + \left(\rho_m \kappa + \rho_l g_l \left(1 - \kappa \right) \right) \mathbf{v}_s \right) \rho_m}{\rho_m \kappa + \rho_l g_l \left(1 - \kappa \right)}$.

Equation 3.23 is solved to get the mixture composition of carbon. To make sure that there is no further macrosegregation when relative velocity becomes zero, it is forced that $\partial C_{mix} / \partial z = 0$ where $g_p > 0$ or $g_s = 1$. The boundary conditions for macrosegregation calculation are given below:

At inlet (z = 0), the concentration is the nominal composition, that is,

$$C_{mix} = C_{nominal} \tag{3.24}$$

All other boundaries' conditions are given by

$$\partial C_{mix} / \partial \vec{n} = 0 \tag{3.25}$$

where $\vec{n}$ denotes the unit normal vector on the slab surfaces.

3.3 Summary

The model proposed in this chapter deals with three-dimensional porosity formation and macrosegregation during the continuous casting of steel with considering solid deformation and shrinkage effect. Due to the steady state nature, the initial stage and final stage of the continuous casting process are not considered. The pore growth due to the contribution of the gas element diffusion is neglected. The model is able to predict porosity and carbon content distribution in the final product of the continuous casting of steel.

In summary, the porosity formation and macrosegregation can be calculated by combining the momentum equation and the mass/species conservation equation. Among all of the variables presenting, the solid fraction field and the thermal field are read-in values. The thermal field is calculated using an in-house code. The solid phase velocity is calculated from Equation 3.16. The proposed fluid flow equation is valid not only in the mushy zone, but also valid in the liquid and solid regions with the permeability reduced to reasonable limits. Therefore, no boundary conditions are needed at the solid/mush and liquid /mush interfaces. This allows the equations to be solved on a regular mesh subject to the boundary conditions only on the exterior boundaries. The porosity and macrosegregation equations are also applicable on the entire domain with proper boundary condition on the slab surface. There are three unknowns, the liquid pressure, pore fraction, carbon concentration, and three equations. So, the problem is closed and can be solved in the following way:

The pressure is solved using Equation 3.7. When the liquid pressure drops below zero, it is set to be zero and the porosity is calculated from the Equation 3.11. The relative velocity can be determined using Equation 3.10. The relative velocity is further imported to Equation 3.23 to predict macrosegregation.

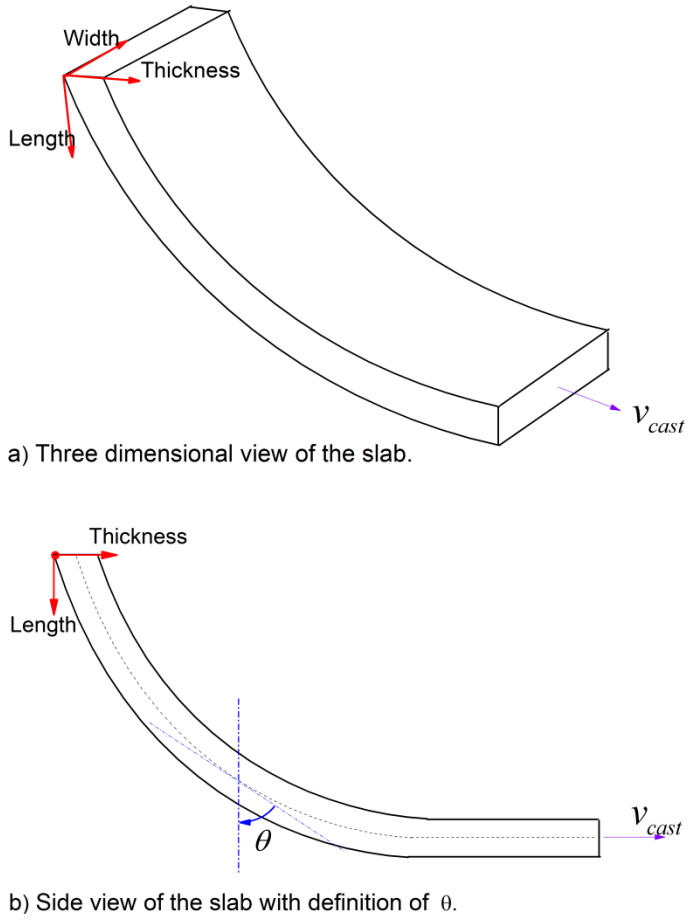

Figure 3.1 Schematic of the physical slab with definition of geometric parameter θ.

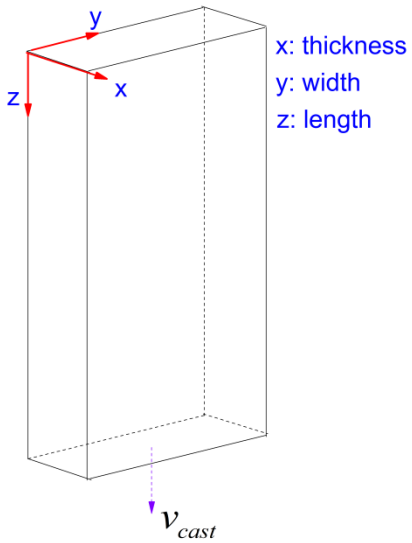

Figure 3.2 Definition of the numerical calculation domain.

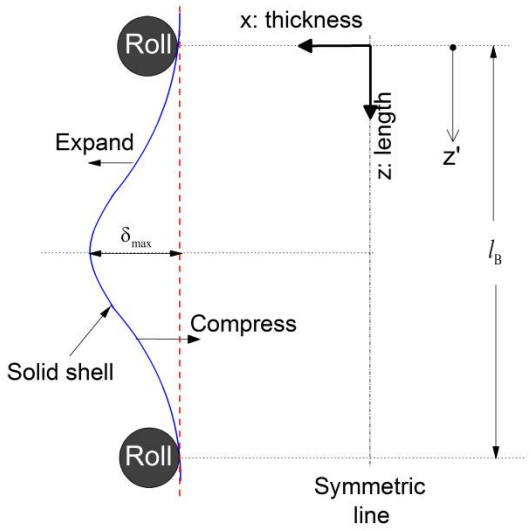

a) Schematic of solid deformation due to bulging

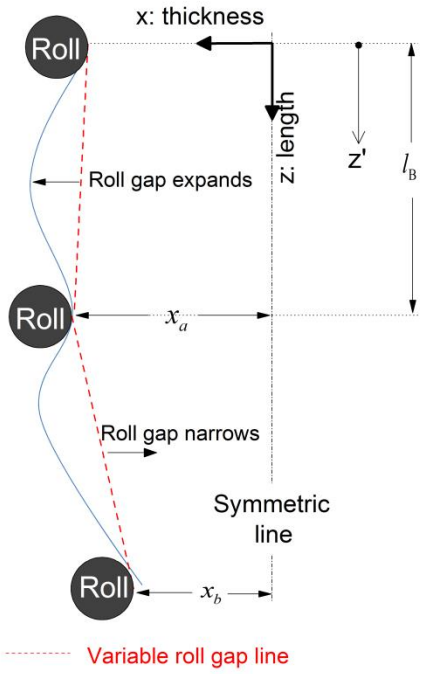

b) Schematic of solid deformation due to variable roll gap.

Figure 3.3 Schematic of solid deformation due to different mechanisms.

CHAPTER IV

COMPUTATIONAL SETUPS

To run the simulation, all parameters defining the continuous casting process have to be available in detail. The parameters for a typical industrial casting are listed in the following sections. A standard case is defined as a case including curved strand and solid deformation due to both bulging and variable roll gap. The results presented in chapter V and VI are either based on the setups in this chapter or with one or more parameters changed.

4.1 Geometry Parameters

The size of the slab is 0.152 m × 2 m × 20 m (thickness × width × length) with a casting speed of casting speed 1.3 m/min. The geometric parameter θ, which describes the shape of the curved strand, is shown in Figure 4.1. The maximum bulging is assumed to be 0.2 mm, which is a typical value from numerical simulation [71].

4.2 Material Properties

The material chosen for current study is steel A36. The nominal chemical composition is as follows (in weight percentage): C: 0.152, S: 0.003, Si: 0.041, Ni: 0.122, Sn: 0.015, Mo: 0.038, Ti: 0.013, P: 0.013, V: 0.008, N: 0.009, Fe: Balance.

The temperature dependent thermophysical properties were generated using IDS [94]. Figure 4.2 shows the variation of material density and partition coefficient of carbon content. For the liquid phase, both density and partition coefficient are corresponding values at the liquids temperature. The liquid dynamic viscosity is 0.0049 ($kg \cdot m^{-1} \cdot s^{-1}$).

4.3 Temperature and Solid Fraction Fields

The temperature and solid fraction field are calculated from an in-house code called Iowa-Caster. It is a model based on three-dimensional steady state model

developed by Hardin *et al.* [36, 37]. When the cooling boundary conditions are fixed, the temperature and solid fraction distribution are functions of casting speed. In Figure 4.3, the temperature and solid fraction fields at a casting speed of 1.3 m/min are shown. With other casting speeds, the contours are similar, only that the extents of the liquid cores are different.

4.4 Solid Velocity

The solid velocity is calculated using Equation 3.16. To calculate the solid velocity, the arrangement of rolls in space (i.e., roll spacing and roll gap) has to be specified. The roll gap and roll spacing information are shown in Figure 4.4 and Figure 4.5, respectively. The maximum bulging is assumed to be 0.2 mm. Based on the given thermal fields in Figure 4.3, the calculated solid velocity along x axis (thickness direction) caused by variable roll gap (Figure 4.6), bulging (Figure 4.7) and the combined effect (Figure 4.8) are shown on the mid-width plane. Solid velocity component on the width direction is assumed to be zero and that along length direction is casting speed.

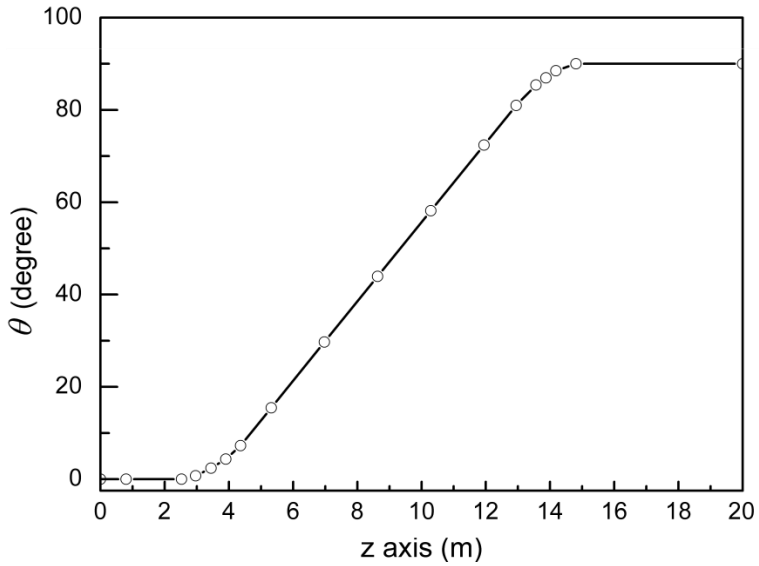

Figure 4.1 Geometric parameter along z axis.

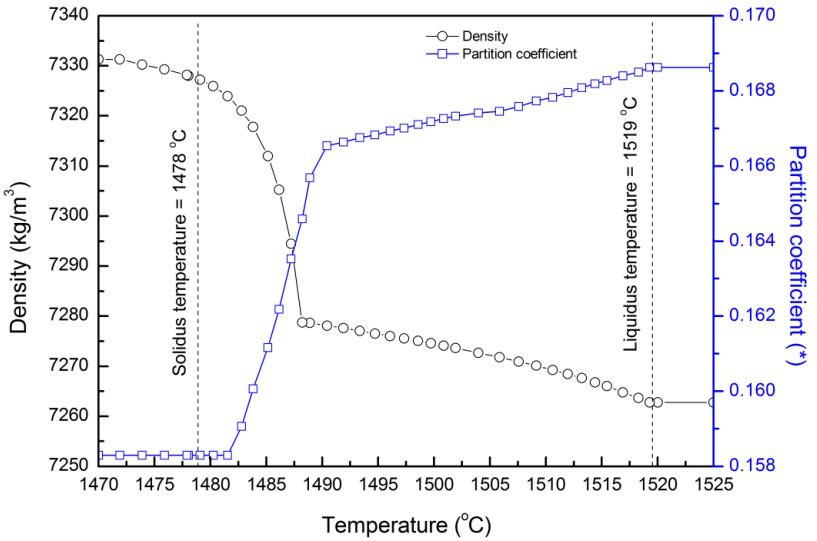

Figure 4.2 Material density and partition coefficient of carbon content of steel A36.

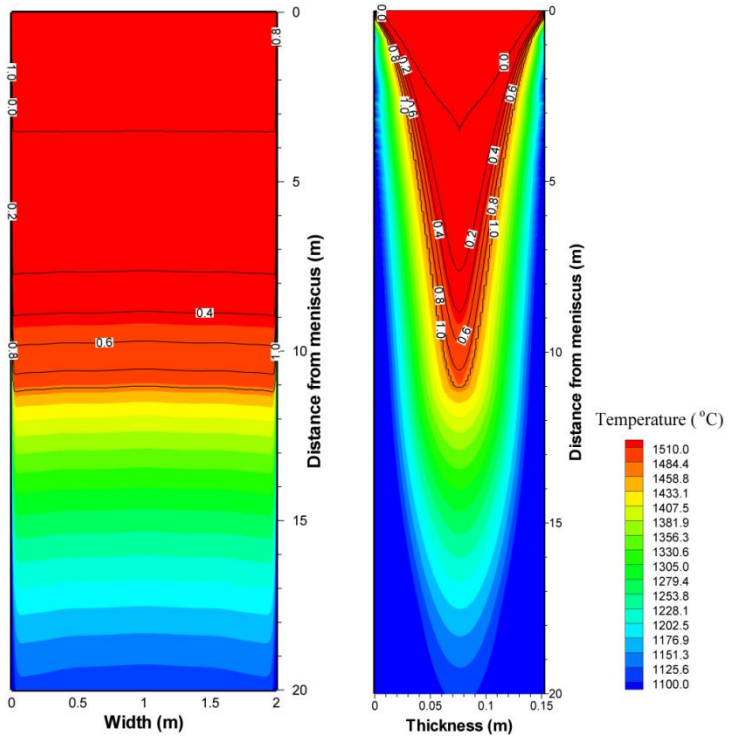

Figure 4.3 Solid fraction and temperature fields for a casting speed of 1.3 m/min.

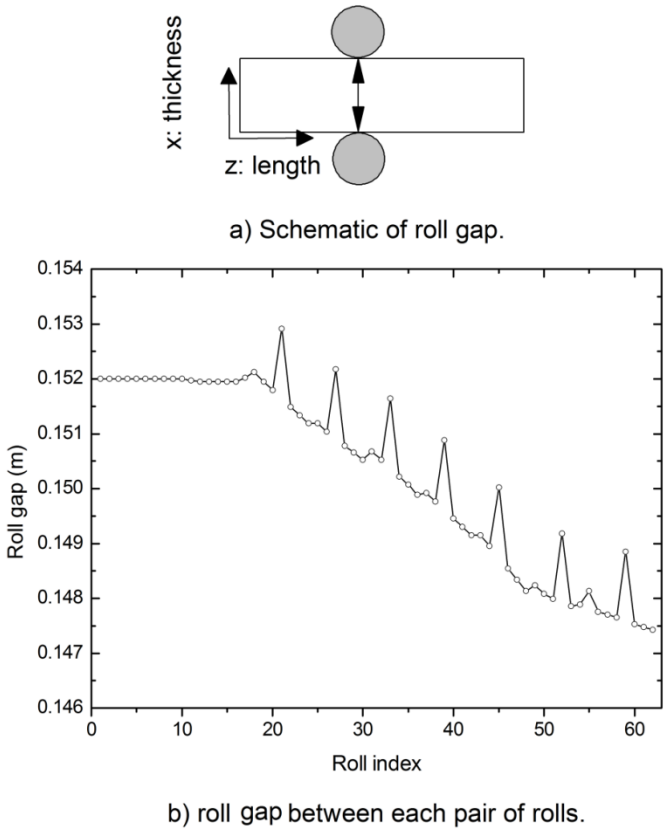

Figure 4.4 Roll gap information.

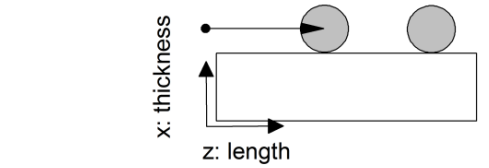

a) Schematic of roll arrangement along length direction.

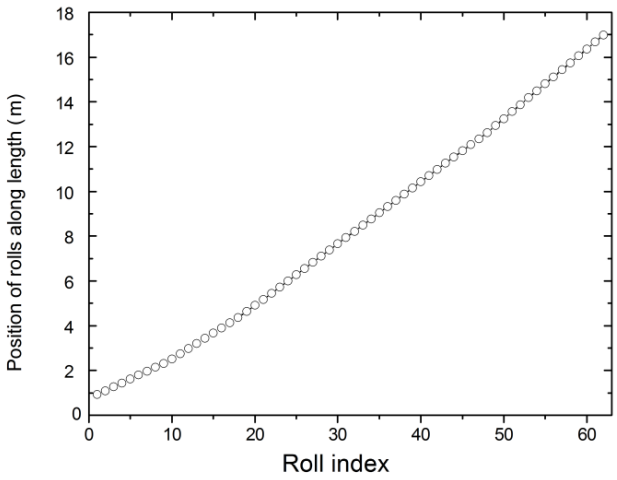

b) Roll distribution along length direction.

Figure 4.5 Roll distribution along length direction.

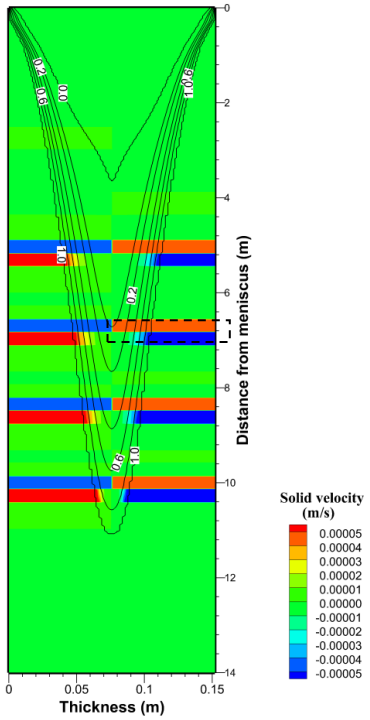

a) Solid velocity contour on mid-width plane
(Lined with solid fraction)

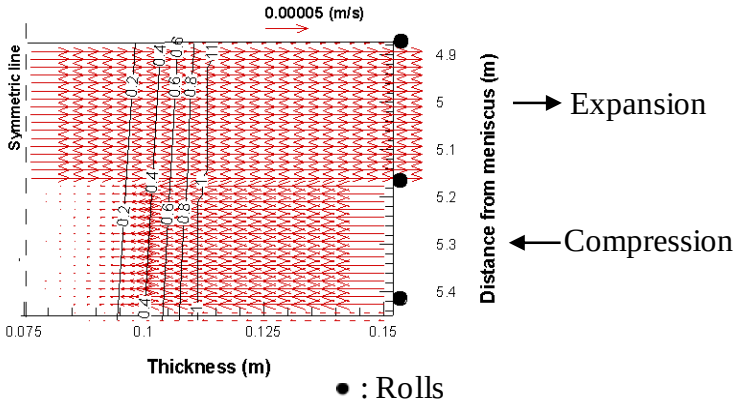

b) Enlarged view of solid velocity
on the mid-width plane

Figure 4.6 Calculated solid velocity due to variable roll gap (lined with solid fraction).

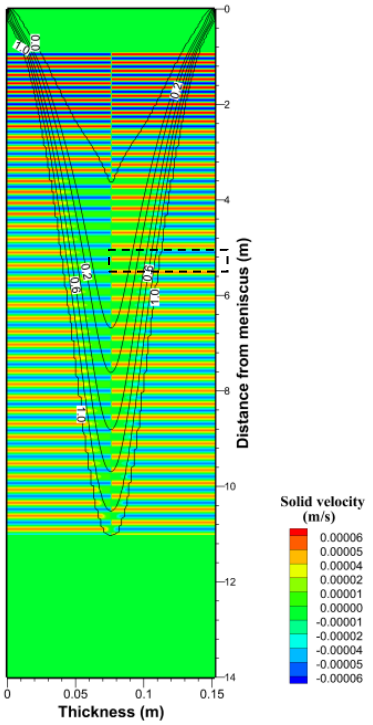

a) Solid velocity contour on mid-width plane (Lined with solid fraction).

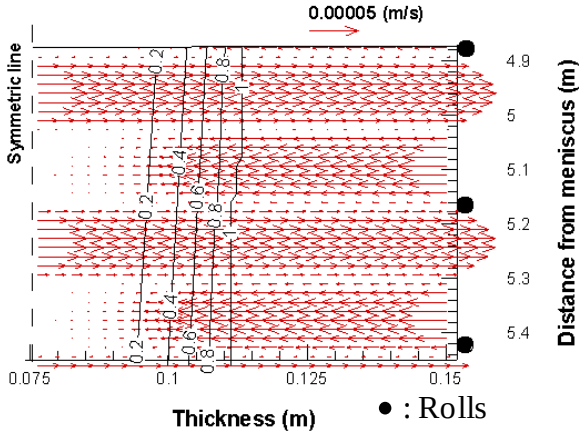

b) Enlarged view of solid velocity on the mid-width plane.

Figure 4.7 Calculated solid velocity due to bulging (lined with solid fraction).

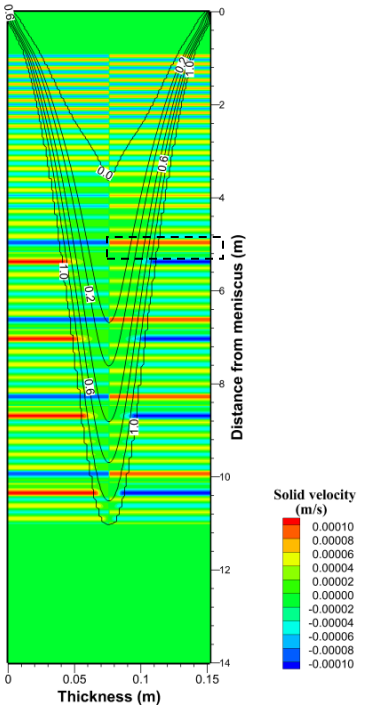

a) Solid velocity contour on mid-width plane (Lined with solid fraction).

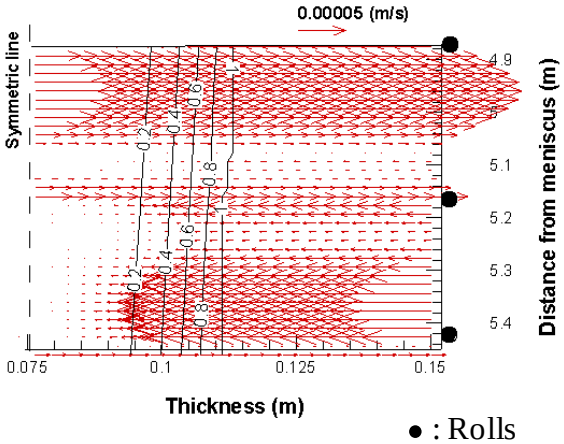

● : Rolls

b) Enlarged view of solid velocity on the mid-width plane

Figure 4.8 Total solid velocity due to both variable roll gap and bulging (lined with solid fraction)

CHAPTER V

MODEL VALIDATION AND GRID STUDY

5.1 Introduction

Given the model proposed in Chapter 3, the liquid flow, porosity formation and macrosegregation can be investigated. Before applying the model to different casting conditions, it has to be verified using simplified numerical test. Also, a full featured casting case is studied on different meshes to determine a suitable grid size to run the simulation.

5.2 Validation

The proposed model is tested using a simple three-dimensional solidification problem that a column of liquid melt sitting on top of a solid base which is moving down at 1 m/min as shown in Figure 5.1.a). Even though the solid base is moving at a constant velocity downward, the solid-liquid interface is stable due to solidification. Since there is no mushy zone involved, this is a casting process of a pure metal. The solid and liquid densities are both 6500 kg/m^3. The atmospheric pressure is 10000 Pa. The gravitational acceleration is 9.8 m/s^2 along the vertical direction. The permeability of liquid and solid are 10^{-4} m^2 and 10^{-17} m^2, which are common values for liquid and solid for a real casting calculated using Equation 3.5. The calculated pressure filed is shown in Figure 5.1.b). Given that the pressure result is constant within the transverse cross section, the calculated and theoretical pressure and relative velocity along the centerline are compared in Figure 5.2. As expected, the liquid pressure is linearly increasing and the relative velocity is zero everywhere. The results validate the current fluid flow model.

5.3 Grid Dependency Study

The calculation was run with different grid sizes to test the grid dependency of the proposed models. The testing cases used here is the standard case defined in Chapter IV.

5.3.1 Results with Different Grid Sizes along Length

The temperature and solid fraction contours calculated using different grid size along length direction are shown in Figure 5.3 and Figure 5.4, respectively. The temperature and solid fraction values along the centerline are compared in Figure 5.5 and Figure 5.6, respectively. A closer observation of solid fraction along center line (as shown in Figure 5.6.b)) indicates the difference of solidification ends calculated on meshes with varying grid sizes along length direction falls into a range of 0.08 m.

The porosity and macrosegregation contours are shown in Figure 5.7 and Figure 5.9, respectively. The averaged porosity and macrosegregation along thickness direction are compared in Figure 5.8 and Figure 5.10. It is clear from Figure 5.8 that the first refinement from 800 to 1200 grid points along length direction increases pore fraction noticeably. Porosity results on further refined mesh (from 1200 to 1500 grid points along length) do not change much. Likewise, the macrosegregation result does not change much when the grid size along length is changed from 1200 to 1500 as observed in Figure 5.10.

5.3.2 Results with Different Grid Sizes along Width

The temperature and solid fraction contours calculated using different grid sizes along width direction are shown in Figure 5.11 and Figure 5.12, respectively. The values along the centerline are compared in Figure 5.13 and Figure 5.14. It can be seen that the solid fraction and temperature field on the two grid sizes are almost identical.

The porosity and macrosegregation contours in the final product are shown in Figure 5.15 and Figure 5.17. The averaged porosity and macrosegregation along thickness direction on the exit plane are compared in Figure 5.16 and Figure 5.18, respectively. All of these results show good agreement on different meshes which means they are not sensitive to grid sizes along width direction.

5.3.3 Results with Different Grid Sizes along Thickness

The temperature and solid fraction contours calculated using different grid sizes along thickness direction are shown in Figure 5.19 and Figure 5.20, respectively. The values along the centerline are compared in Figure 5.21 and Figure 5.22. A closer observation of solid fraction along center line in Figure 5.22.b) shows the difference of solidification end extension is now increased to 0.3m which is larger than results obtained with different grid sizes along length and width direction.

The porosity and macrosegregation contours are shown in Figure 5.23 and Figure 5.25, respectively. The averaged porosity and macrosegregation along thickness direction are compared in Figure 5.24 and Figure 5.26, respectively. The dramatic jump in the porosity and macrosegregation results from coarse mesh to fine mesh is because that the solidification ends and solid deformation environments are quite different on different meshes. The results indicate that fine mesh is needed along thickness direction. When the thickness direction grid size reaches 150, the results will not change much with further refinement.

5.4 Summary

In this chapter, the fluid flow model has been validated using a very simple case which has an analytical solution. The numerical calculation based on the proposed model gives identical results to the theoretical values. Also, a typical case with real casting conditions is investigated on meshes with different grid sizes. By changing the grid size, we can see that the results are not sensitive to the grid size along width and length direction; changing of the grid size along thickness direction has a greater effect. It is desirable to have fine mesh along thickness direction. It is obvious from the comparison of results that a good choice of grid size should be no smaller than 150×100×1200 (thickness × width× length). A finer mesh will not change the results by much.

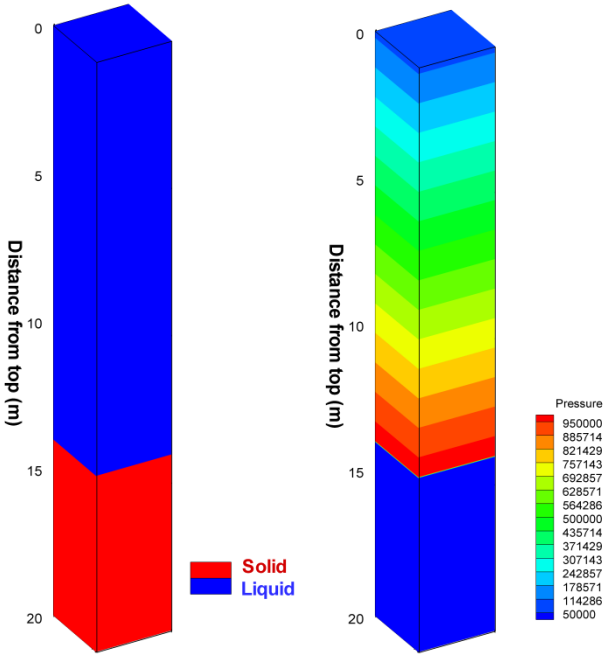

a) Liquid and solid domain b) Pressure result (Pa)

Figure 5.1 Solid fraction setup and pressure results.

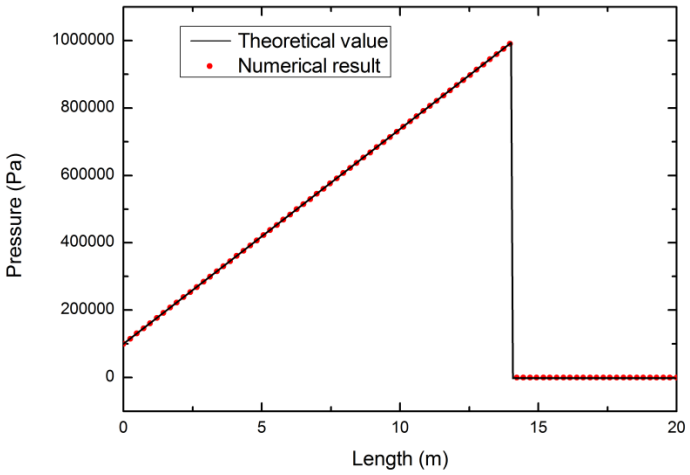

a) Pressure result

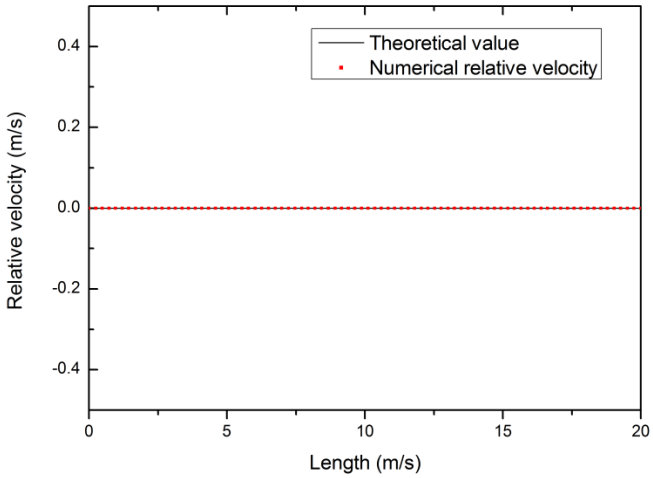

b) Relative velocity result

Figure 5.2 Pressure and relative velocity along vertical direction.

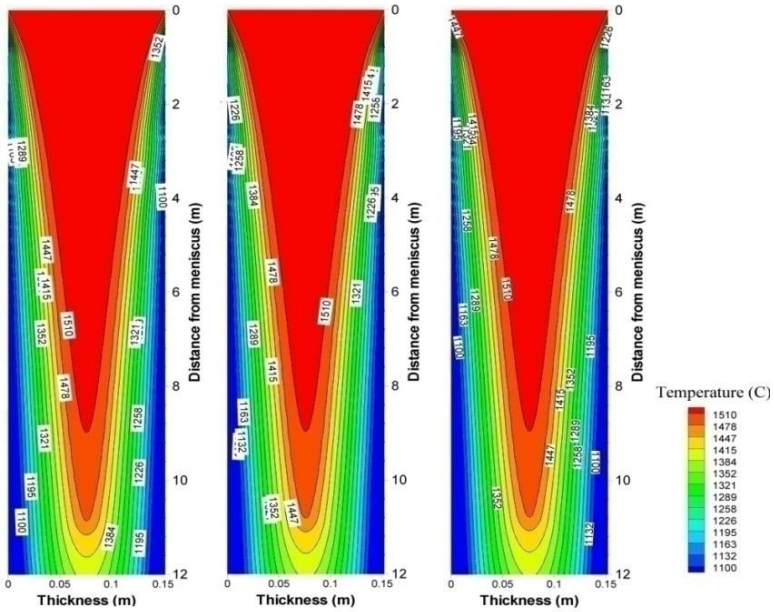

Grid size: 100×100×800 100×100×1200 100×100×1500

Figure 5.3 Temperature results on the mid-width plane with different grid sizes (thickness×width×length) along length.

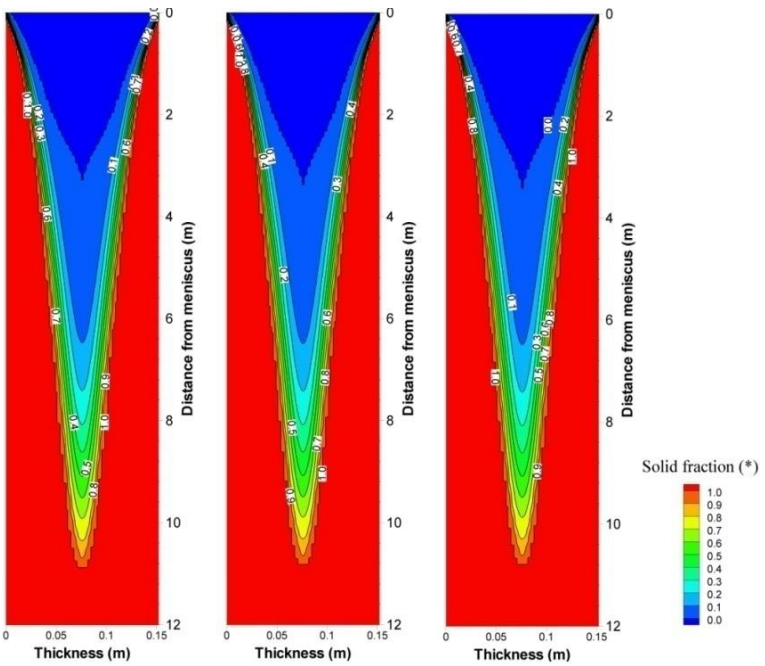

Grid size: 100×100×800 100×100×1200 100×100×1500

Figure 5.4 Solid fraction results on the mid-width plane with different grid sizes (thickness×width×length) along length.

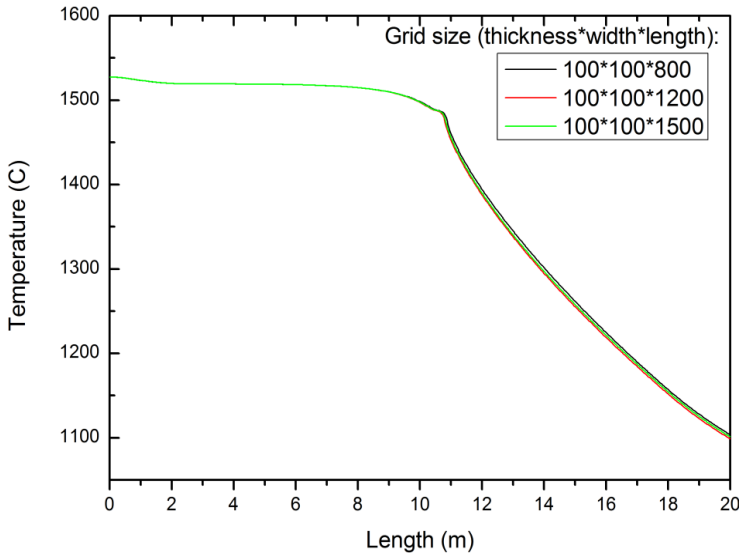

Figure 5.5 Temperature results along center line with different grid sizes along length.

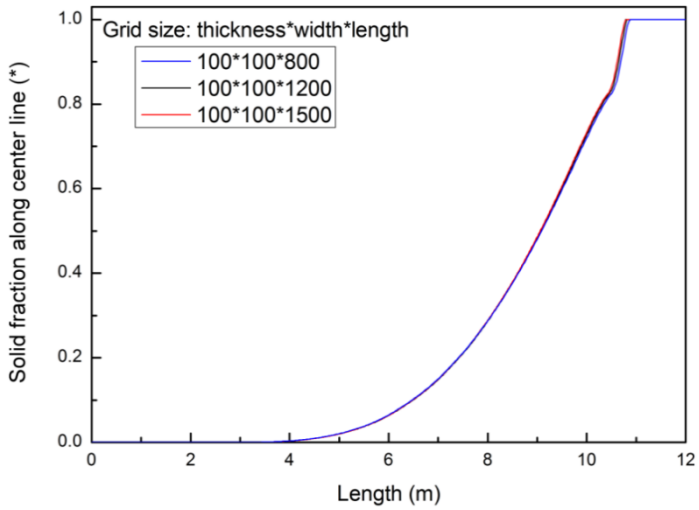

a) Solid fraction results along centerline.

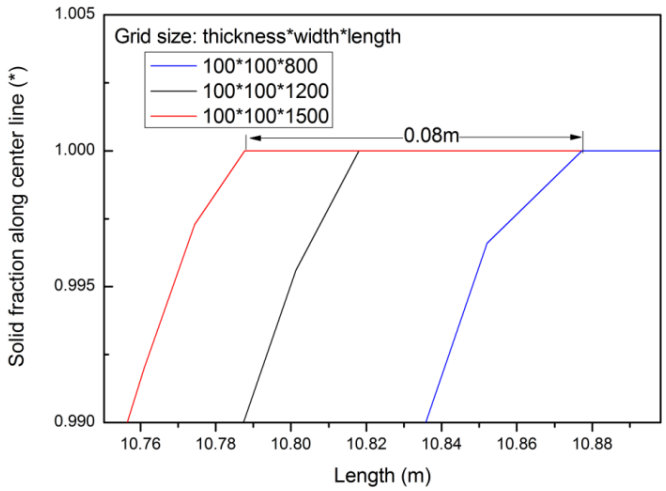

b) Enlarged view of solid fraction results along centerline.

Figure 5.6 Solid fraction results along center line with different grid sizes along length.

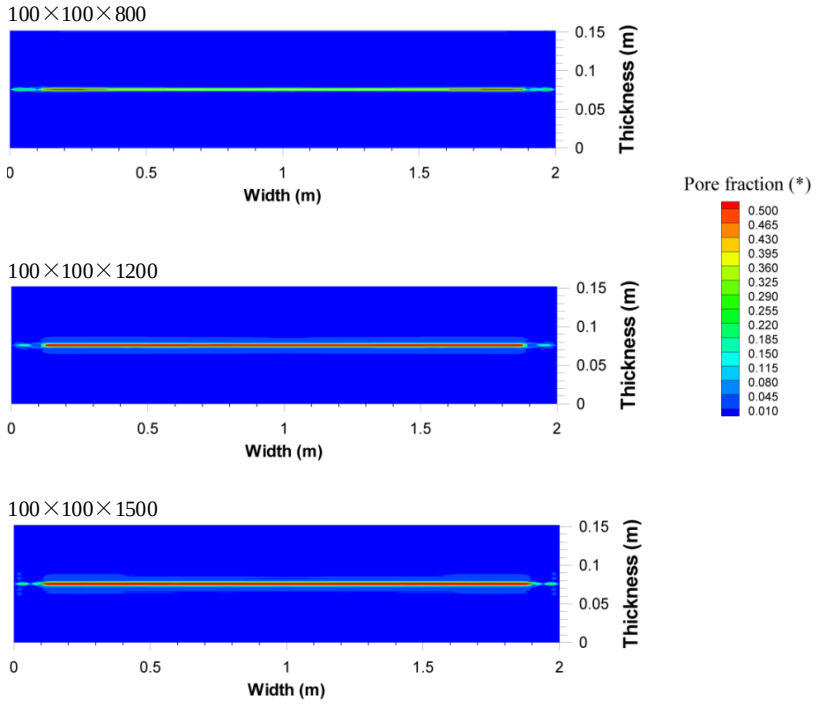

Figure 5.7 Pore fraction results on exit plane with different grid sizes (thickness×width×length) along length.

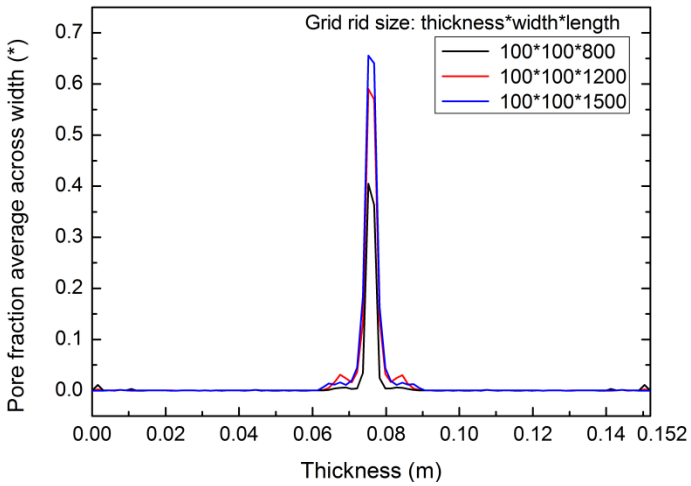

Figure 5.8 Averaged pore fraction along thickness direction on exit plane with different grid sizes.

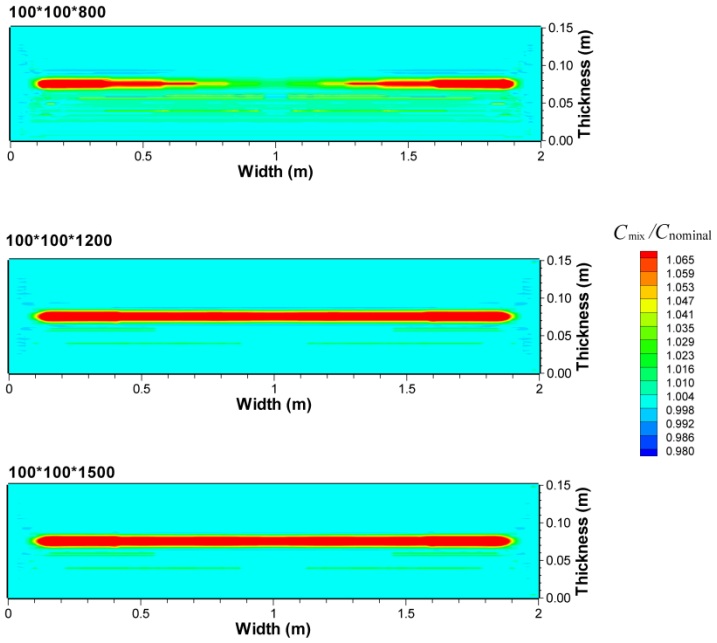

Figure 5.9 Carbon concentration ($C_{mix}/C_{nominal}$) on exit plane with different grid sizes (thickness×width×length) along length.

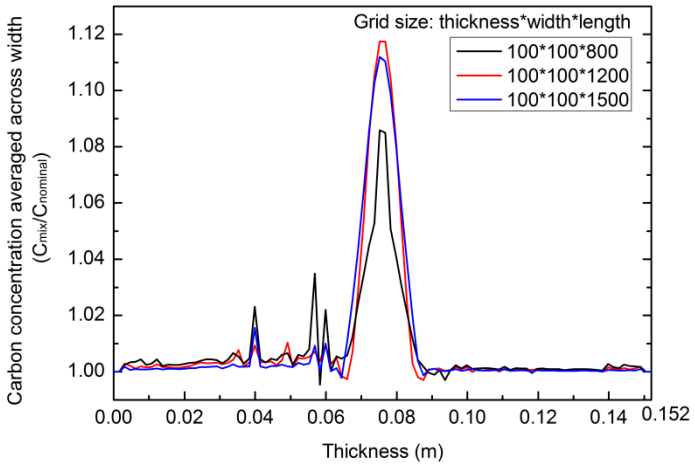

Figure 5.10 Averaged carbon concentration (C_{mix} /$C_{nominal}$) along thickness direction on exit plane with different grid sizes.

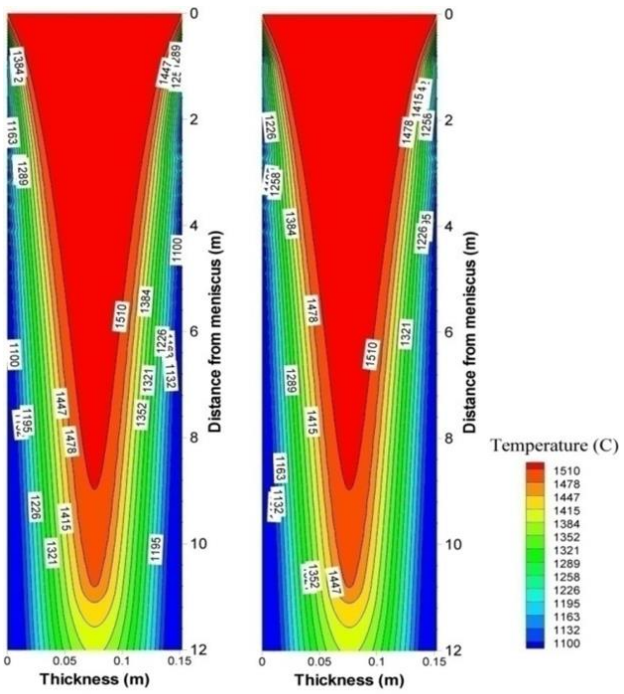

Grid size: 100×76×1200 100×100×1200

Figure 5.11 Temperature results on the mid-width plane with different grid sizes (thickness×width×length) along width.

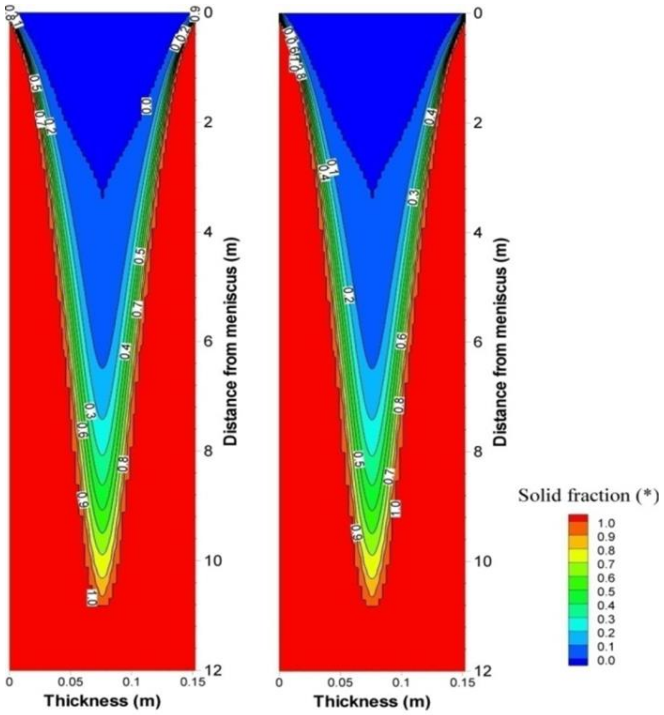

Grid size: 100×76×1200 100×100×1200

Figure 5.12 Solid fraction results on the mid-width plane with different grid sizes (thickness×width×length) along width.

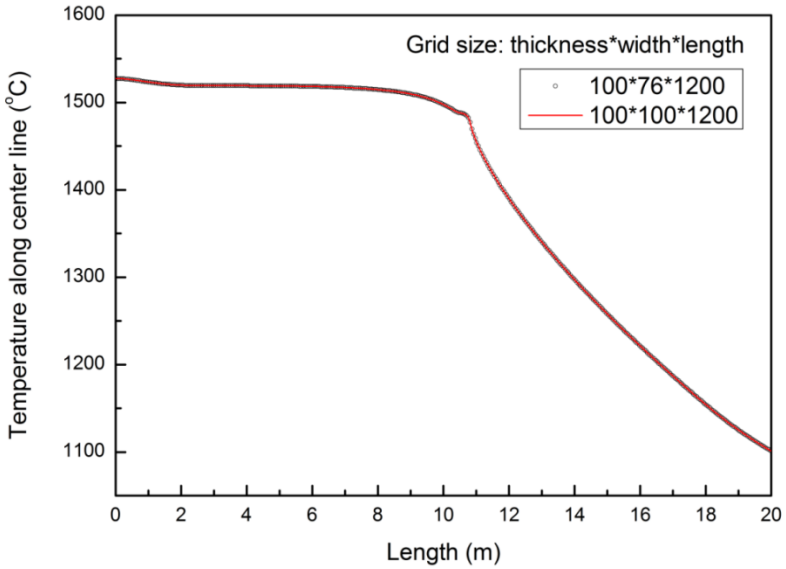

Figure 5.13 Temperature results along centerline with different grid sizes.

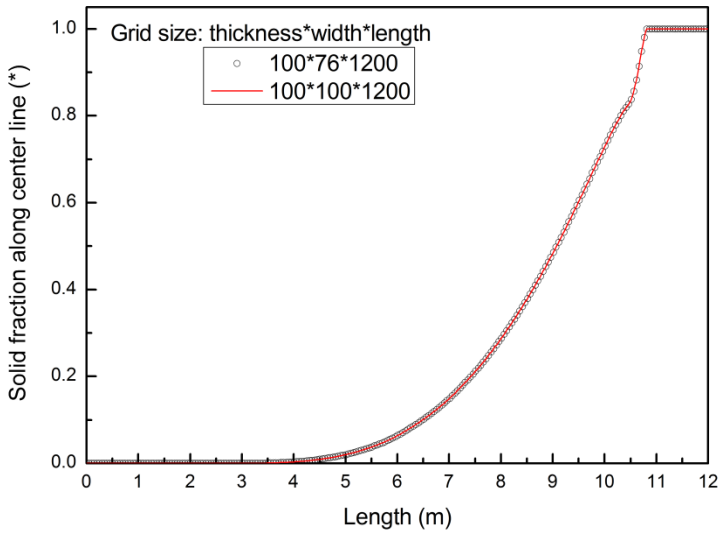

a) Solid fraction results along centerline.

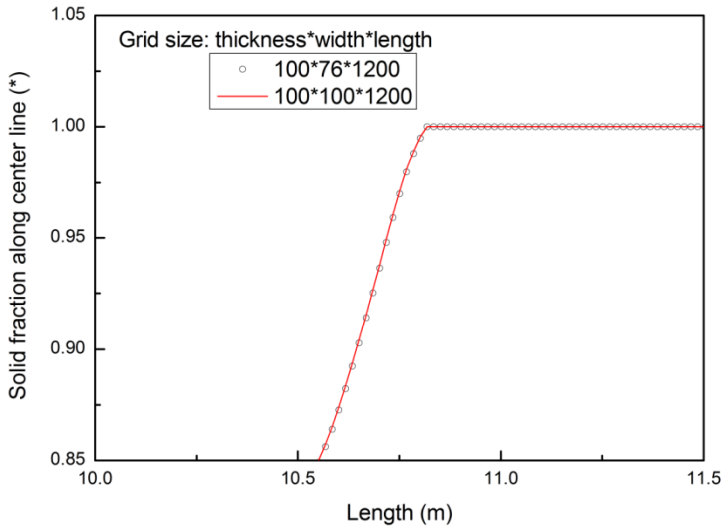

b) Enlarged view of solid fraction results along centerline.

Figure 5.14 Solid fraction results along centerline with varying grid sizes.

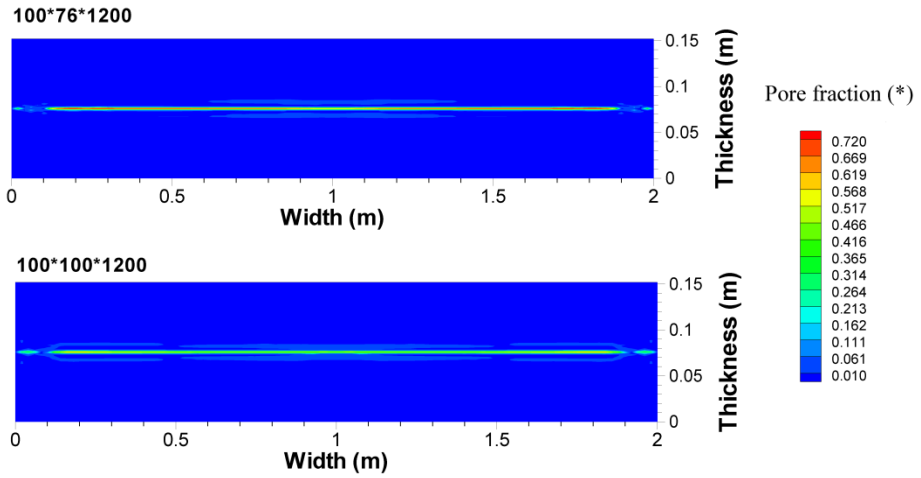

Figure 5.15 Pore fraction results on exit plane with different grid sizes (thickness×width×length)along width.

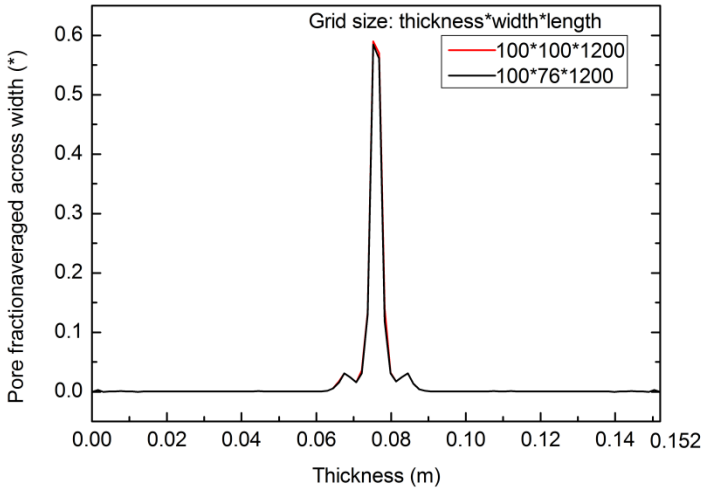

Figure 5.16 Averaged pore fraction along thickness on exit plane with different grid sizes.

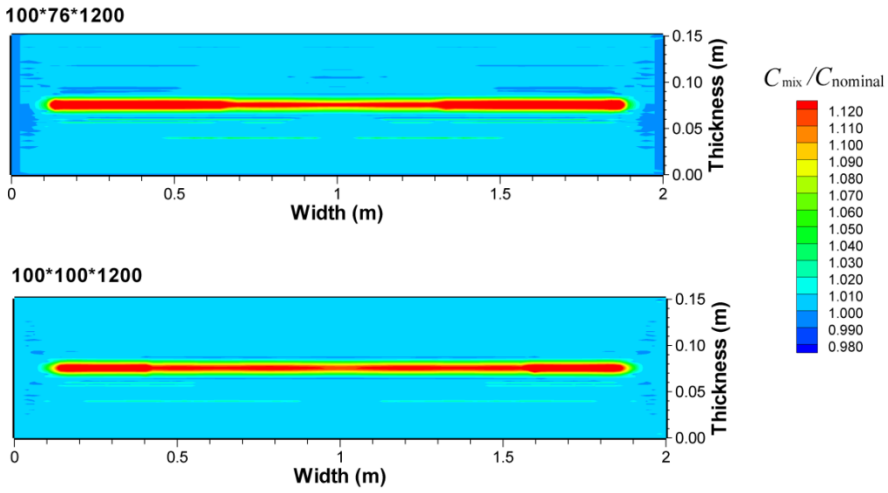

Figure 5.17 Carbon concentration ($C_{mix}/C_{nominal}$) on exit plane with different grid sizes (thickness×width×length).

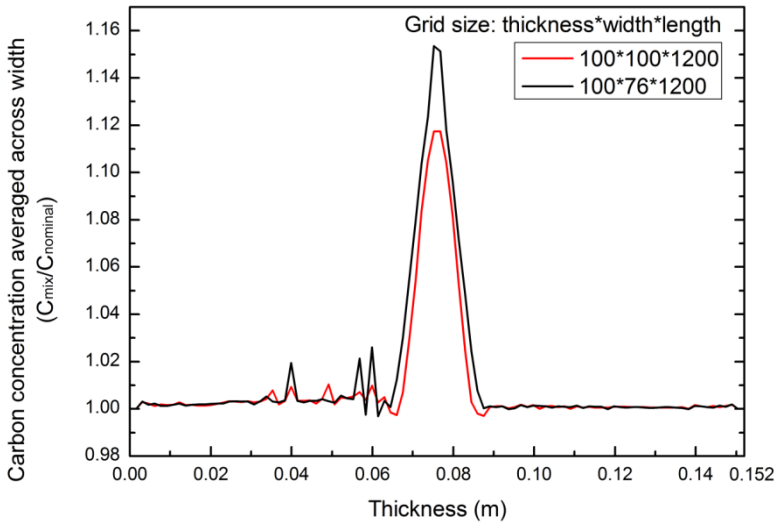

Figure 5.18 Averaged Carbon concentration (C_{mix} /$C_{nominal}$) along thickness direction on exit plane with different grid sizes.

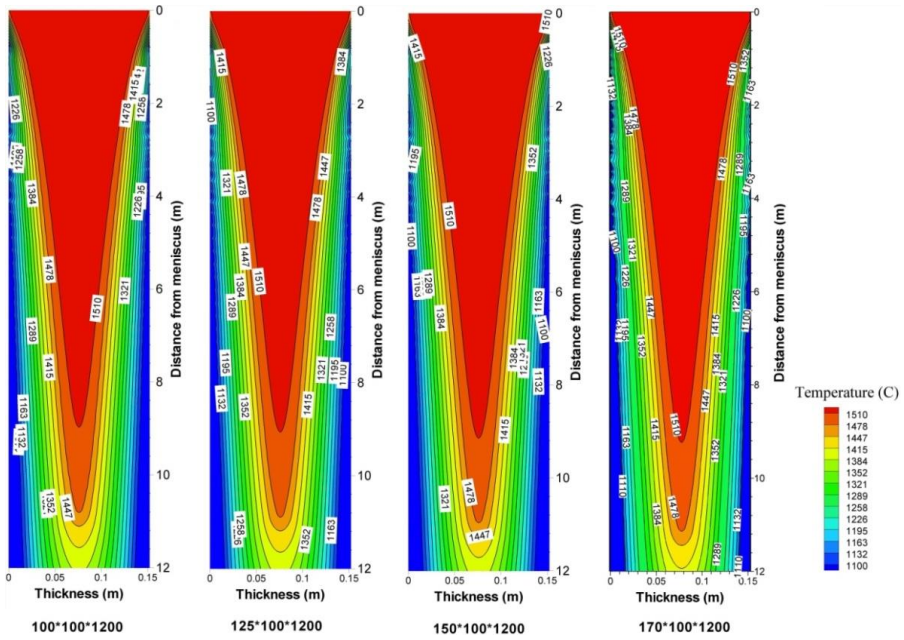

Figure 5.19 Temperature results on the mid-width plane with different grid sizes (thickness×width×length) along thickness.

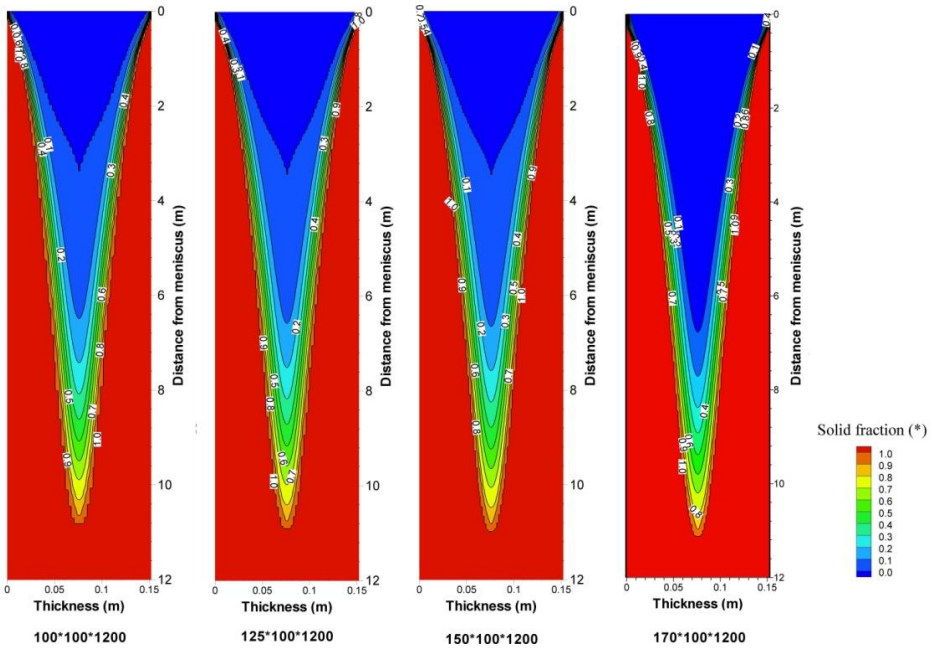

Figure 5.20 Solid fraction results on the mid-width plane with different grid sizes (thickness×width×length) along thickness.

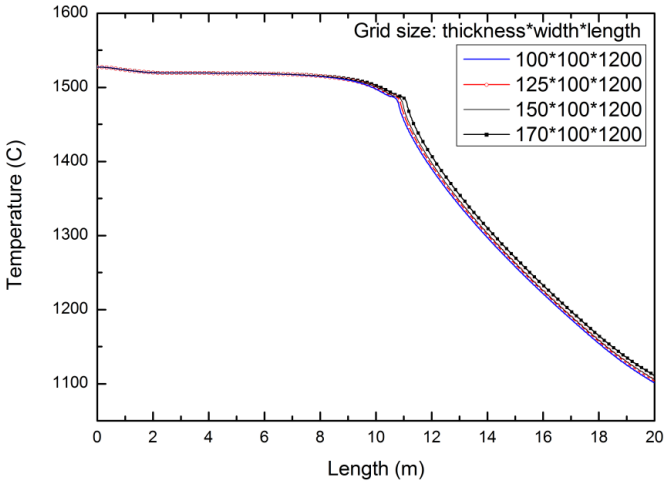

Figure 5.21 Temperature results along centerline with different grid sizes along thickness.

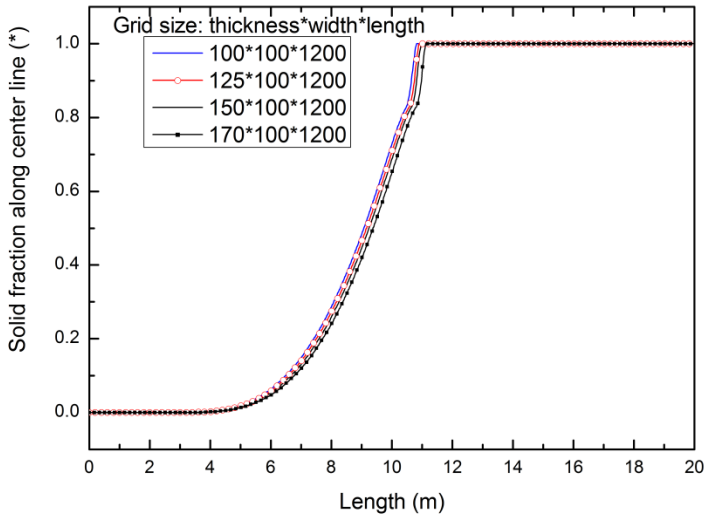

a) Solid fraction results along centerline.

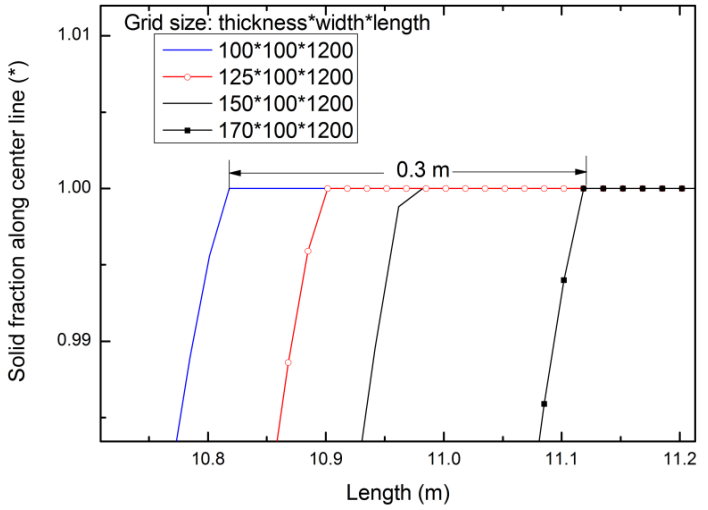

b) Enlarged view of solid fraction results along length.

Figure 5.22 Solid fraction results along centerline with different grid sizes along thickness.

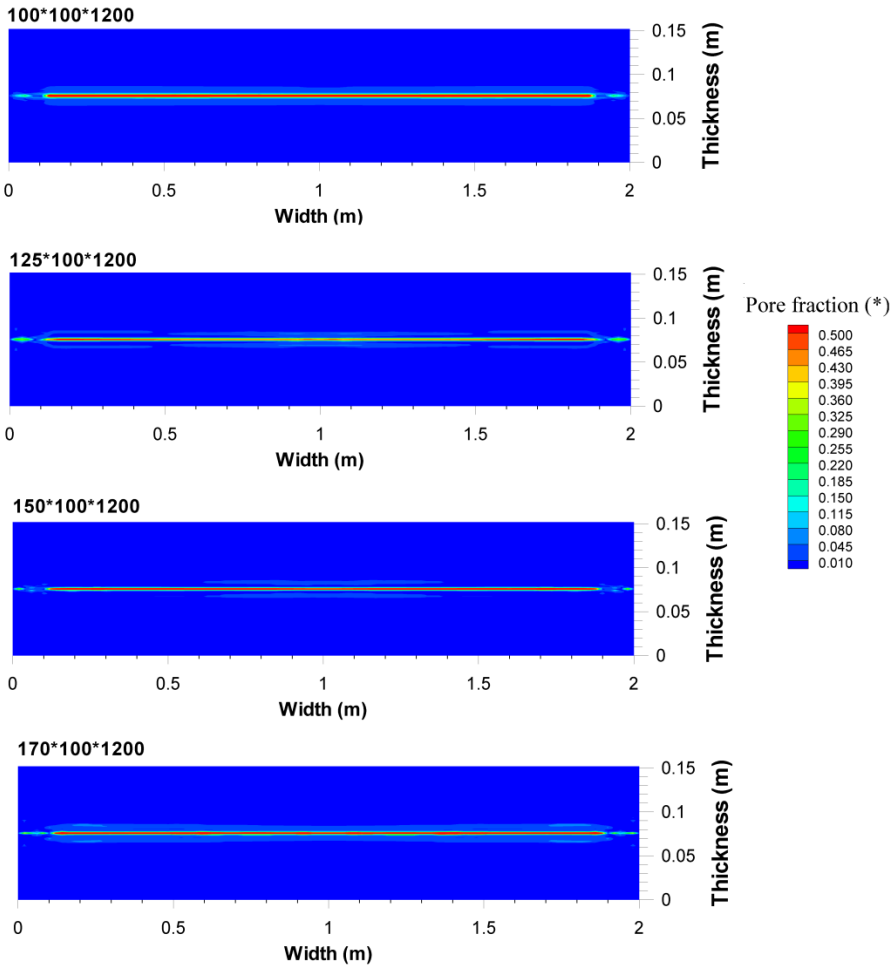

Figure 5.23 Pore fraction results on exit plane with different grid sizes (thickness×width×length) along thickness.

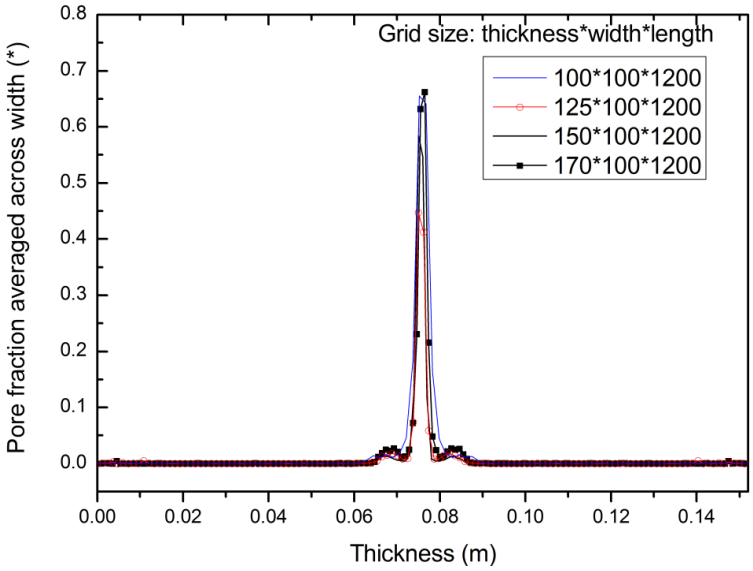

Figure 5.24 Averaged pore fraction along thickness direction on exit plane with different grid sizes.

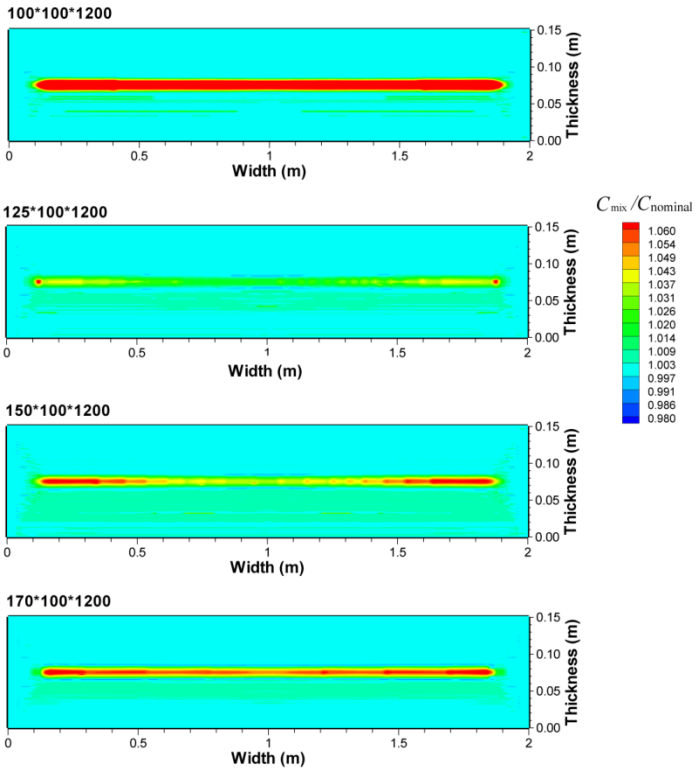

Figure 5.25 Carbon concentration ($C_{mix}/C_{nominal}$) on exit plane with different grid sizes (thickness×width×length) along thickness.

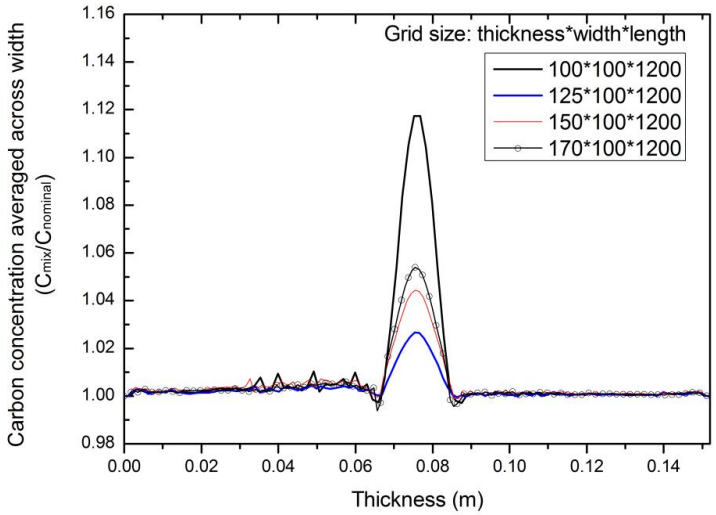

Figure 5.26 Averaged carbon concentration (C_{mix} /C_{nominal}) along thickness direction on exit plane with different grid sizes.

CHAPTER VI

CASE STUDIES AND RESULTS

The mathematical models have been for porosity and macrosegregation calculation in continuous casting of steel. In this chapter, cases with different operating conditions are investigated. The aim is to find the relationship between each operating condition and the product quality. The first section demonstrates the importance of solid deformation for both porosity and macrosegregation prediction. Then the rest of this chapter will discuss how degree of bulging, soft reduction and casting speed influence the porosity and macrosegregation in the final products. All of the calculations presented here are performed on a mesh size of 150×100×1200 (thickness × width × length).

6.1 Effect of Solid Deformation

In this part, five numerical testing cases with different operating conditions are performed. The computational setups are based on the standard case in Chapter IV with one or more conditions changed. The operating conditions for each case are listed in Table 6.1 in detail.

6.1.1 Results for Case 1

This case considers a vertical strand with no solid deformation.

The pressure and relative velocity results for this case are shown in Figure 6.1. The pressure increases in low solid fraction region and drop dramatically until zero in mushy zone. Since for this case the solid phase is rigid, the fluid flow is simply driven by shrinkage upon solidification. It can be seen that the relative velocity vectors point from the center to the periphery to compensate the space left by phase change. Porosity results are shown in Figure 6.2. As expected, the porosity mainly forms around high solid fraction region along the centerline, where the liquid feeding is most difficult. The

porosity is totally shrinkage porosity and its magnitude is low, an average of 0.24% in the final product for this case.

Figure 6.3 shows the macrosegregation contours on the mid-width plane, exit plane and the averaged carbon concentration along thickness direction. It is clear that the macrosegregation of carbon content caused by shrinkage flow is very small. The deviation of carbon concentration from the nominal value is below 0.5%. The standard deviation of carbon concentration is 0.2% of the nominal composition. We can conclude that shrinkage flow is not the main reason of centerline macrosegregation.

6.1.2 Results for Case 2

This case considers a curved strand with no solid deformation.

The pressure result and relative velocity result for this case are shown in Figure 6.4. Since the strand is curved, the gravitational force has a nonzero component along thickness direction. As a result of this, the tangent of the pressure contour near the centerline is no longer horizontal and the pressure gradient drives the liquid flow in a circular form in the bulk liquid region as observed in Figure 6.4.b). In the mushy zone, the liquid flows toward the solidification front to feed the volume difference upon phase change. Figure 6.5 shows the porosity results and Figure 6.6 shows the macrosegregation results. The average porosity and standard deviation of carbon concentration are 0.24% and 0.21%, respectively. Comparing with case 1, even though there is a significant difference in the bulk liquid flow, the porosity and macrosegregation results are very close. This tells us that the fluid flow in the bulk liquid region is less important than the flow in mushy zone with regard to the porosity and macrosegregation defects.

6.1.3 Results for Case 3

This case considers a vertical strand with solid deformation due to variable roll gap only. The solid deformation field due to variable roll gap is given in Figure 4.6.

The pressure and relative velocity results for this case are shown in Figure 6.7. Comparing with case 1, solid deformation due to variable roll gap is considered. As expected, when roll gap narrows, the liquid is driven toward center plane by compression; when roll gap expands, the liquid floods the center region and then moves toward periphery to fill the space left behind by shrinkage and solid movement. The porosity result is presented in Figure 6.8. The average porosity in the final product is 0.22%. This value is very close to the cases without solid deformation; however, the porosity distribution patterns are quite different. Figure 6.9 shows the macrosegregation results on mid-width plane, exit plane, and the averaged carbon concentration along thickness. The standard deviation of carbon concentration is 2.2% of the nominal composition. A carbon concentration peak sitting at the centerline is observed which tells us that the solid deformation is the main cause of macrosegregation.

6.1.4 Results for Case 4

This case considers a vertical strand with solid deformation due to bulging only. The solid deformation field due to bulging is given in Figure 4.7.

The pressure and relative velocity results are shown in Figure 6.10. The velocity results follow the same principle as that in case 3. It can be clearly seen from Figure 6.10.c) that, the solid shell expands at the top half of the region between each two successive rolls, the liquid flow toward the periphery; The solid shell is compressed at the bottom half region and the compression drives the liquid flow toward the center plane. The porosity result is shown in Figure 6.11 and macrosegregation result is shown in Figure 6.12. The average porosity in the final product is 1.5% and the standard deviation of carbon concentration is 2.4% of nominal composition. Comparing with case 3, the porosity and macrosegregation in the final product are further increased which indicates that solid deformation due to bulging has a stronger effect than variable roll gap in case 3.

6.1.5 Results for Case 5

This case considers a curved strand with solid deformation due to both bulging and variable roll gap. The solid deformation field is as given in Figure 4.8. This is a case with real casting conditions.

The pressure and relative velocity results for this case are shown in Figure 6.13. The porosity and macrosegregation results are shown in Figure 6.14 and Figure 6.15, respectively. The phenomena met in this case are nothing special but a combined effect of case 2 to case 4. The average porosity and standard deviation of carbon concentration are 1% and 1.1% of nominal composition, respectively.

The velocity of bottom slab surface (x coordinate is 0) and carbon concentration along centerline for this case is shown in Figure 6.16, where negative slab surface velocity indicates slab expansion and positive slab surface velocity indicates slab compression. It can be seen from there that when the slab surface is compressed, solute-poor solid phase moves to the centerline, the macrosegregation is decreased; when the slab surface expands, the solid is pulled out and the liquid phase is sucked into centerline region to increase macrosegregation.

6.1.6 Comparison of Case 1 to 5

A comparison of averaged pore fraction along thickness direction on the exit plane is shown in Figure 6.17. It can be seen that, the solid deformation due to bulging and variable roll gap tend to change the porosity (both magnitude and distribution) in the final product. With current roll arrangement, bulging has a more noticeable effect. This comparison shows the necessity of including solid deformation in prediction of porosity. Figure 6.19 is a schematic drawing of the critical region for porosity formation. The porosity mainly forms over the span between the positive pressure end (see Figure 6.19) and solidification end along the centerline. The length between these two critical points is

called "length of porosity formation (LPF)". Two factors influence the magnitude of porosity in the final product:

1. When the LPFs vary by large amounts for different cases, the longer the LPF is, the higher the porosity level is. This is because the porosity has a longer region to develop.

2. When the LPFs for different cases are very close, the magnitude of solid deformation plays a major role. Higher expanding deformation will cause more net outward mass flow and thus higher porosity.

Figure 6.18 shows the averaged carbon concentration along thickness direction for different cases. It is clear that without solid deformation, the distribution of carbon is almost homogeneous. When the solid deformation is included, the centerline macrosegregation is observed. Solid deformation seems to be the major cause of centerline macrosegregation. Moreover, the macrosegregation in the final product highly depends on the solid deformation field around the positive pressure end.

6.2 Effect of Degree of Bulging

Four different degrees of bulging ($\delta_{\max} = 0.2$ mm, 0.5 mm, 0.8 mm and 1.0mm) are implemented for case 5 listed in Table 6.1. The pore fraction distributions on the exit plane for different degrees of bulging are shown in Figure 6.20. The average and maximum pore fraction values in the final product are listed in Figure 6.21. It can be seen that the high porosity area extends with increasing degree of bulging, as a result of which the average pore fraction increases.

Figure 6.22 shows the pressure and solid fraction along centerline. It can be seen that the LPF is increasing with higher degree of bulging. At the same time, higher degree of bulging also increases outward mass flow. According to Equation 3.16, the mass leave the centerline with the same velocity as slab surface in region A (as in Figure 3.3); however, the mass return to the centerline with a velocity smaller than the velocity of slab

surface in region B. The volume difference caused by this inward and outward mass flow is filled with porosity. With higher degree of bulging, the net outward mass flow is increased, thus the final porosity is higher.

It has been discussed in Section 6.1.6 that macrosegregation is sensitive to solid deformation around the positive pressure end. As shown in Figure 6.22, the positions of positive pressure ends are different and thus the macrosegregation is case sensitive. From the macrosegregation contour and standard deviation of carbon composition in the final product we can see that, with increasing degree of bulging, macrosegregation is first increased and then decreased.

6.3 Effect of Soft Reduction

Calculations are performed on three roll arrangements with different soft reductions (as shown in Figure 6.26). Other computational setups are the same as for case 5 in Section 6.1.

Figure 6.27 shows porosity in the final product with different soft reductions. The average and maximum porosity value for different cases are listed in Figure 6.28. It can be seen from the results that from soft reduction case 1 (SR1) to soft reduction case 3 (SR3) the maximum and average value of porosity both have been reduced.

Figure 6.29 shows macrosegregation contours in the final product with different soft reductions. The maximum and standard deviation of macrosegregation are listed in Figure 6.30. Likely, the centerline macrosegregation is smaller and the overall carbon concentration is more homogeneous (smaller standard deviation) with further soft reduction. These trends are the same as observed in experiments.

Figure 6.28 and Figure 6.30 indicate that, for both porosity and macrosegregation alleviation, the soft reduction applied to the segment around solidification end is more effective than applied to the prior caster segment.

6.4 Effect of Casting Speed

Five cases with different casting speeds are calculated. The casting speeds used are 1.1 m/min, 1.2 m/min, 1.3 m/min, 1.4 m/min and 1.5 m/min. The temperature and solid fraction contour for all these cases are shown in Figure 6.31. The operating conditions for all cases in this section are the same as for case 5 in Section 6.1.

The porosity and macrosegregation contours in the final products are compared in Figure 6.32 and Figure 6.34, respectively. Maximum and average porosity in the final product are shown in Figure 6.33. Maximum and standard deviation of macrosegregation are listed in Figure 6.35.

We can tell that both the porosity and macrosegregation present no clear trend with casting speed. The reason is that with different casting speeds, the solidification ends fall into different regions where the solid deformation environments are quite different. As has been discussed in Section 6.1, the solid deformation plays a major role in both porosity formation and centerline macrosegregation. So, the porosity and macrosegregation in the final products for different casting speeds are very case dependent.

6.5 Summary

New mathematical models are developed to investigate porosity formation and macrosegregation in the continuous casting of steel. Case studies with and without solid deformation are performed. The comparison of results highlights the necessity of including solid deformation in the prediction of both porosity and macrosegregation. Different operating conditions are performed and compared. It can be seen that higher degree of bulging tends to increase porosity while soft reduction can reduce porosity. For different casting speeds, both the lengths of porosity formation and positive pressure end lay in different solid deformation environments. So, there is no obvious relation between

casting speeds and porosity. Macrosegregation can also be mitigated by soft reduction however it is case dependent regarding to the degree of bulging and casting speed.

Table 6.1 Operating conditions for different cases.

	Variable roll gap	Bulging	Curved strand
Case 1	N	N	N
Case 2	N	N	Y
Case 3	Y	N	N
Case 4	N	Y	N
Case 5	Y	Y	Y

N=No, Y=Yes

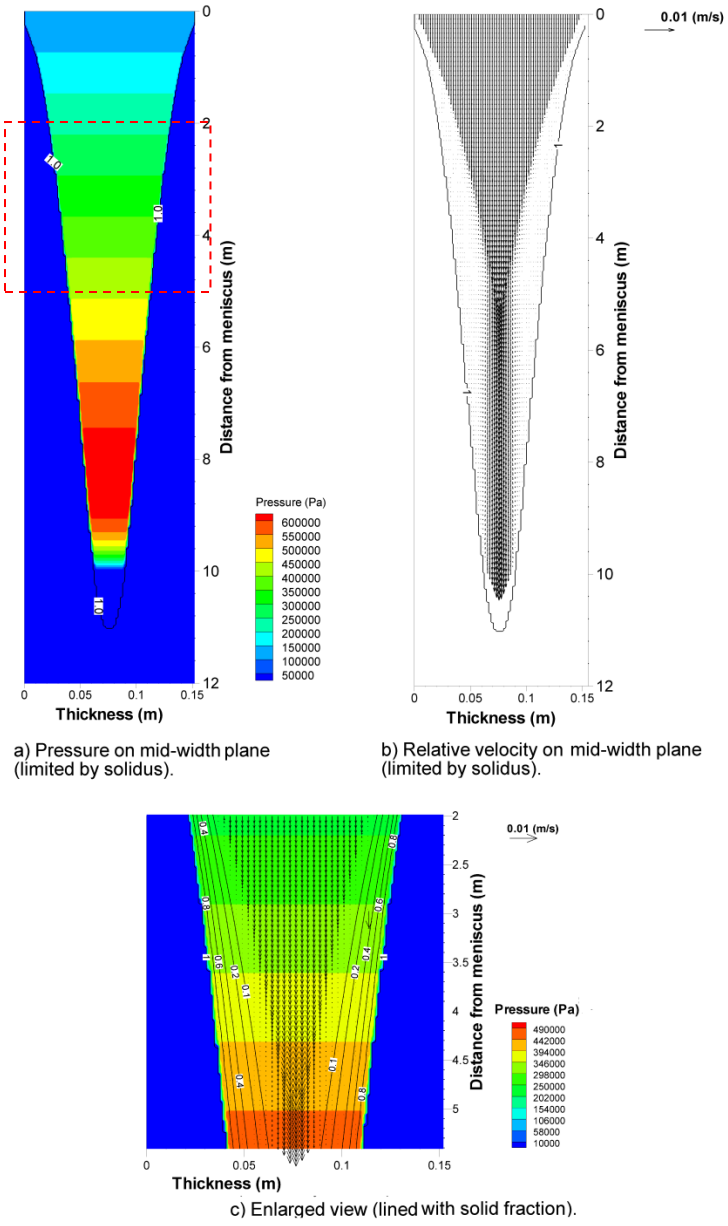

a) Pressure on mid-width plane (limited by solidus).

b) Relative velocity on mid-width plane (limited by solidus).

c) Enlarged view (lined with solid fraction).

Figure 6.1 Relative velocity and pressure field for case 1.

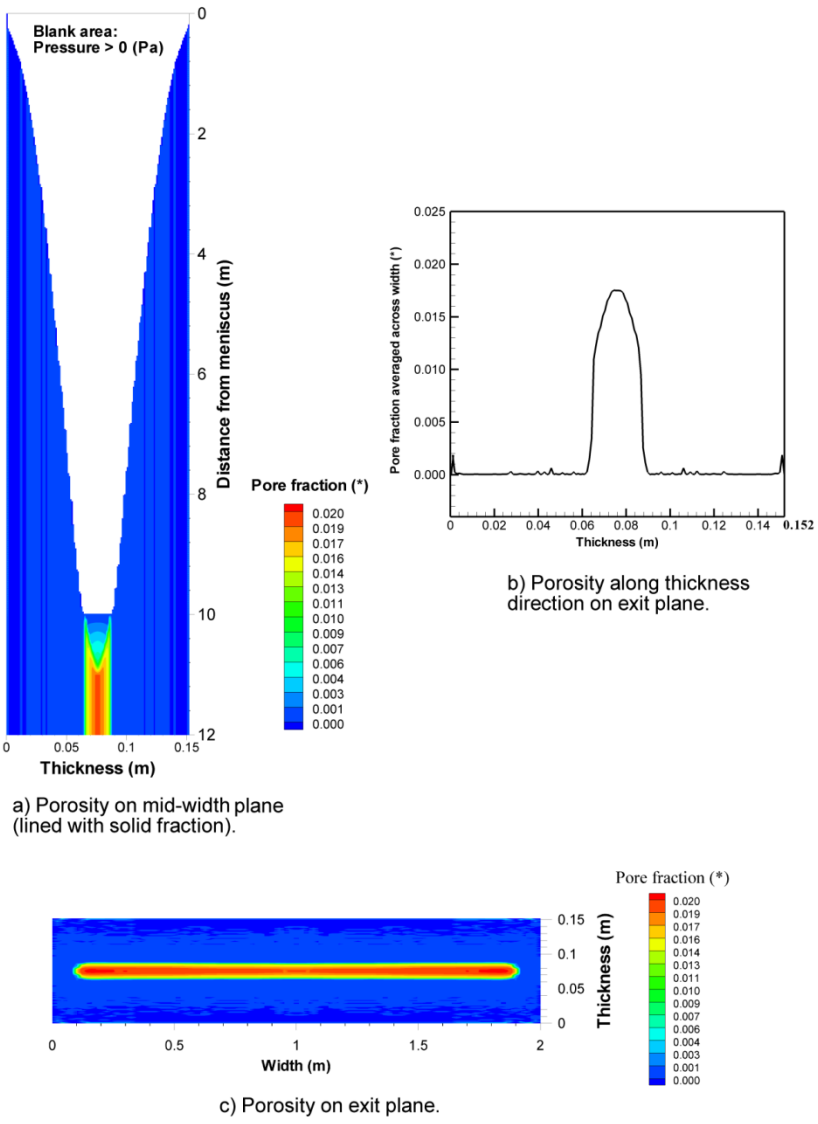

a) Porosity on mid-width plane (lined with solid fraction).

b) Porosity along thickness direction on exit plane.

c) Porosity on exit plane.

Figure 6.2 Porosity results for case 1.

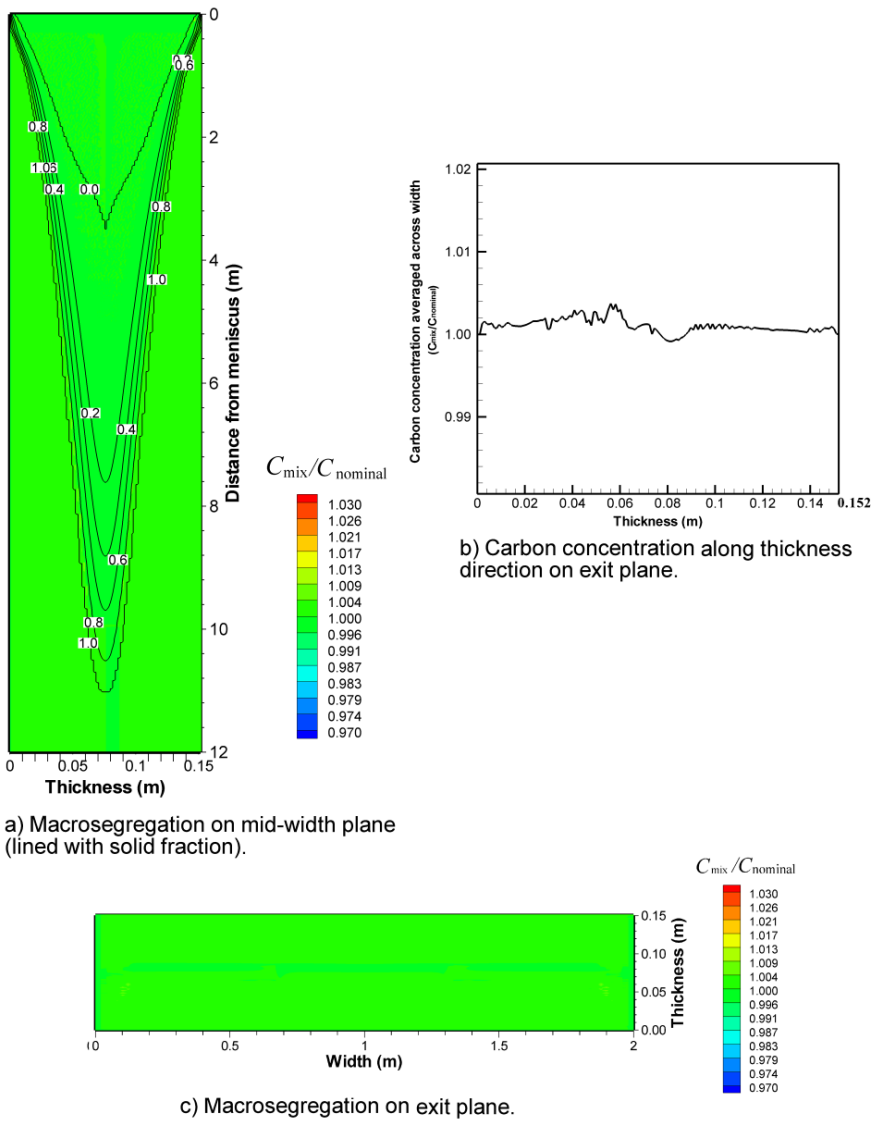

a) Macrosegregation on mid-width plane (lined with solid fraction).

b) Carbon concentration along thickness direction on exit plane.

c) Macrosegregation on exit plane.

Figure 6.3 Macrosegregation results for case 1.

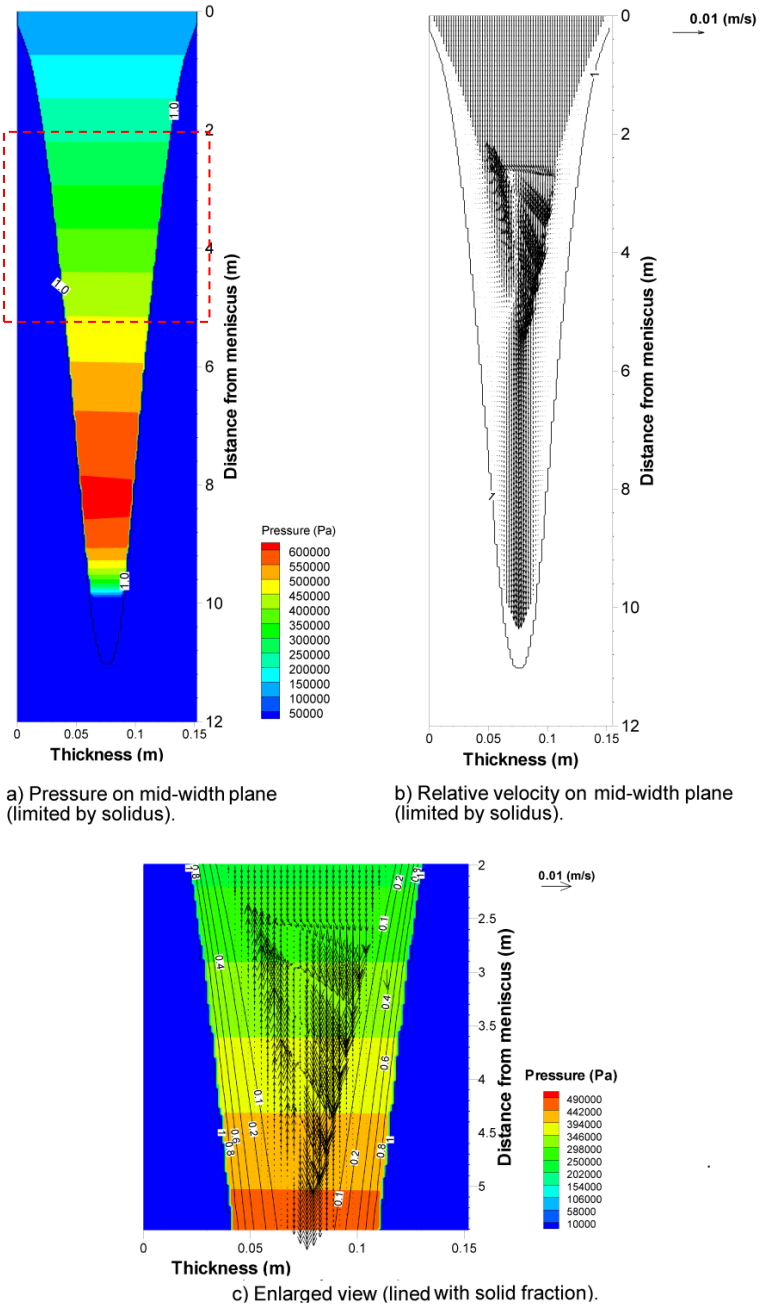

a) Pressure on mid-width plane (limited by solidus).

b) Relative velocity on mid-width plane (limited by solidus).

c) Enlarged view (lined with solid fraction).

Figure 6.4 Relative velocity and pressure field for case 2.

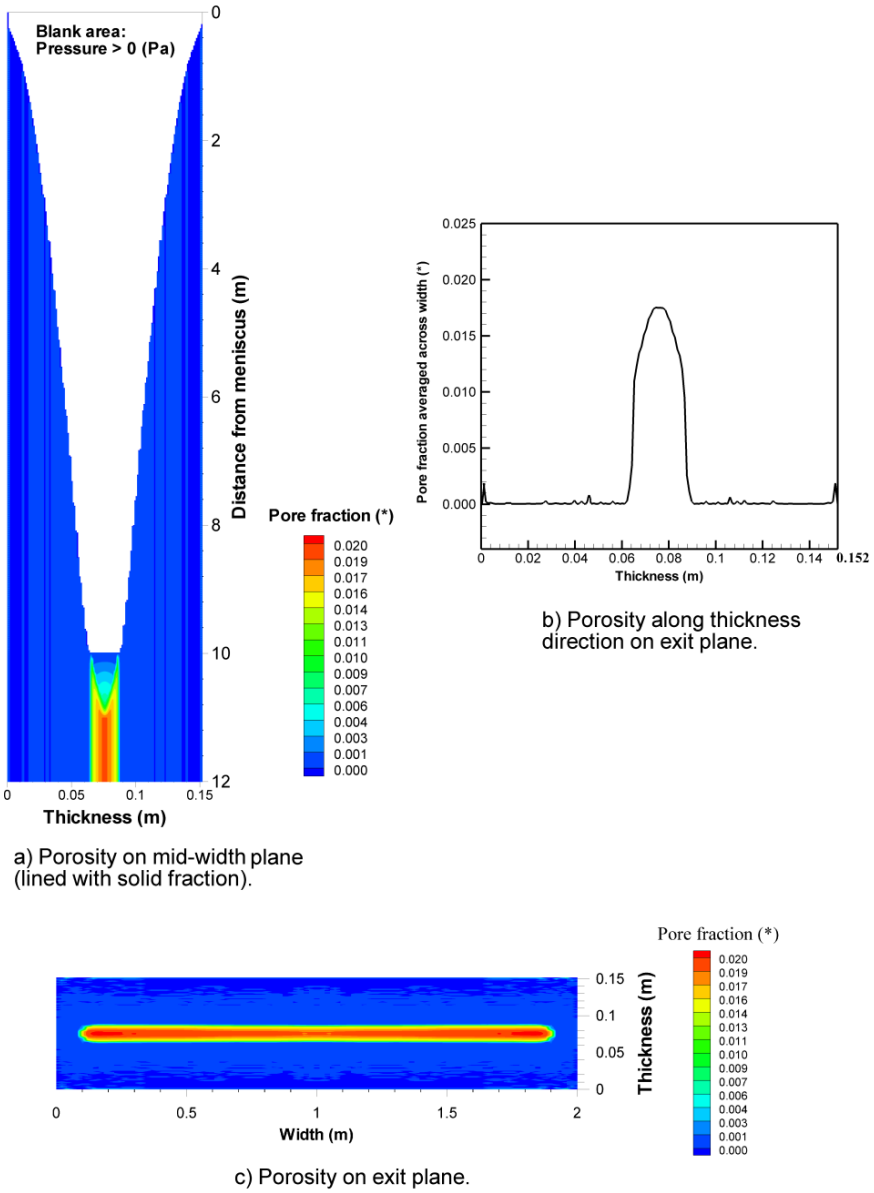

a) Porosity on mid-width plane (lined with solid fraction).

b) Porosity along thickness direction on exit plane.

c) Porosity on exit plane.

Figure 6.5 Porosity results for case 2.

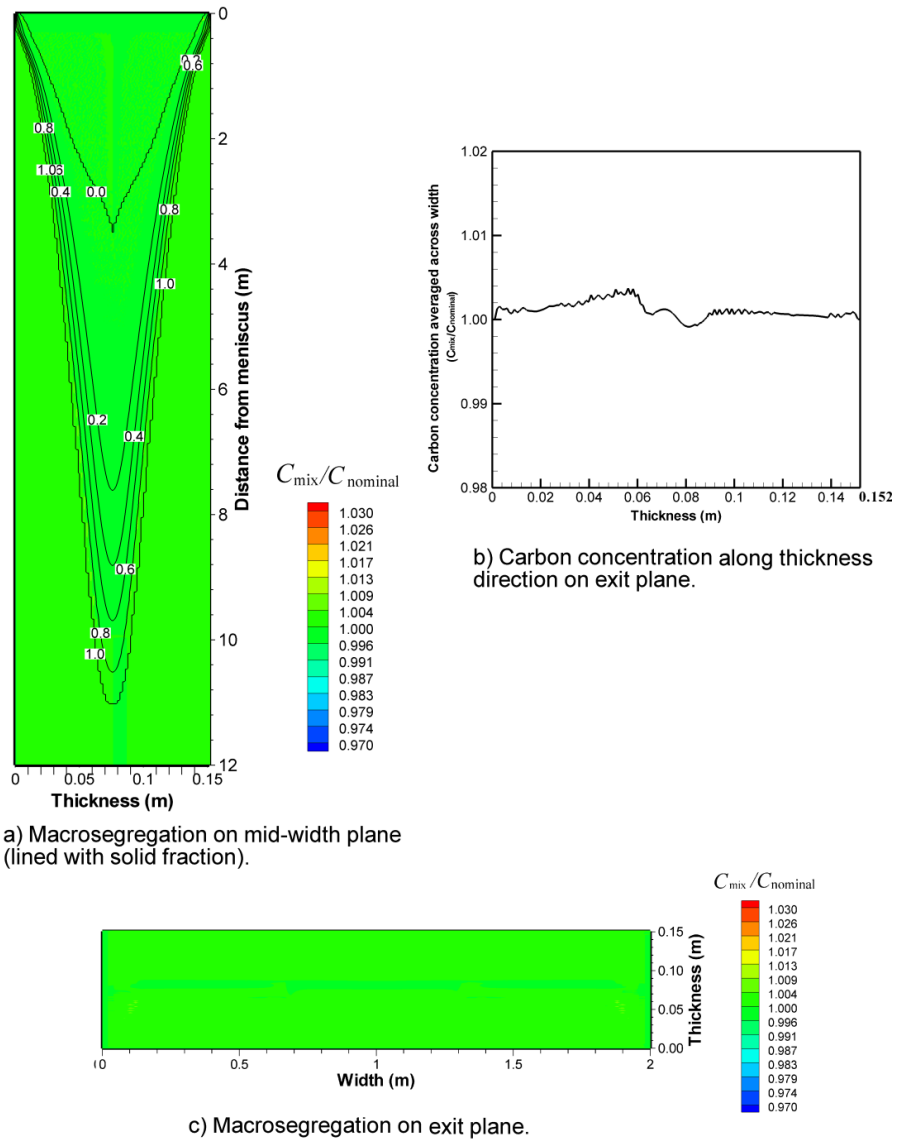

a) Macrosegregation on mid-width plane (lined with solid fraction).

b) Carbon concentration along thickness direction on exit plane.

c) Macrosegregation on exit plane.

Figure 6.6 Macrosegregation results for case 2.

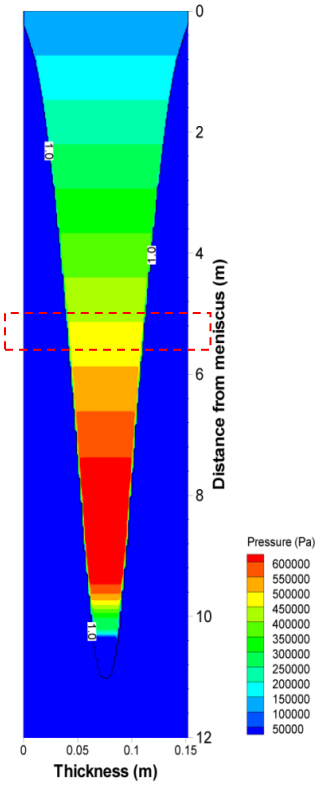

a) Pressure field on mid-width plane (Limited by solidus line).

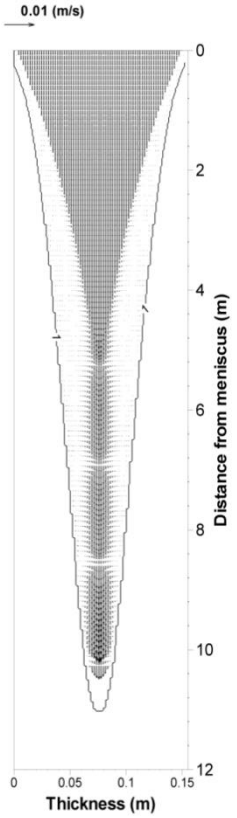

b) Relative velocity on mid-width plane (Limited by solidus line).

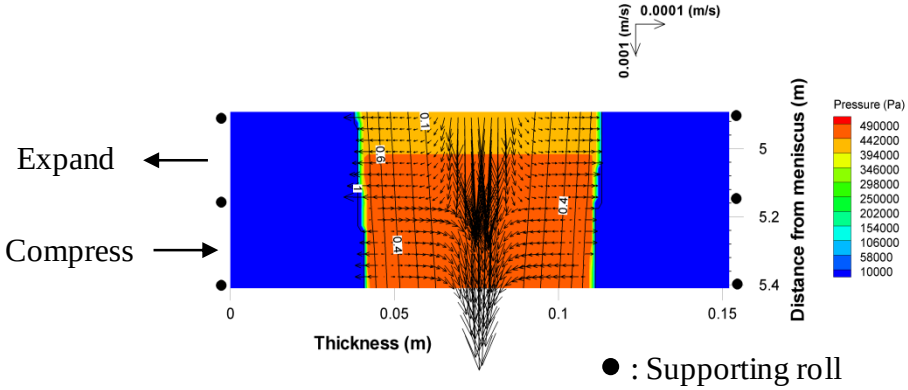

c) Enlarged view of pressure and relative velocity on mid-width plane.

Figure 6.7 Relative velocity and pressure field for case 3.

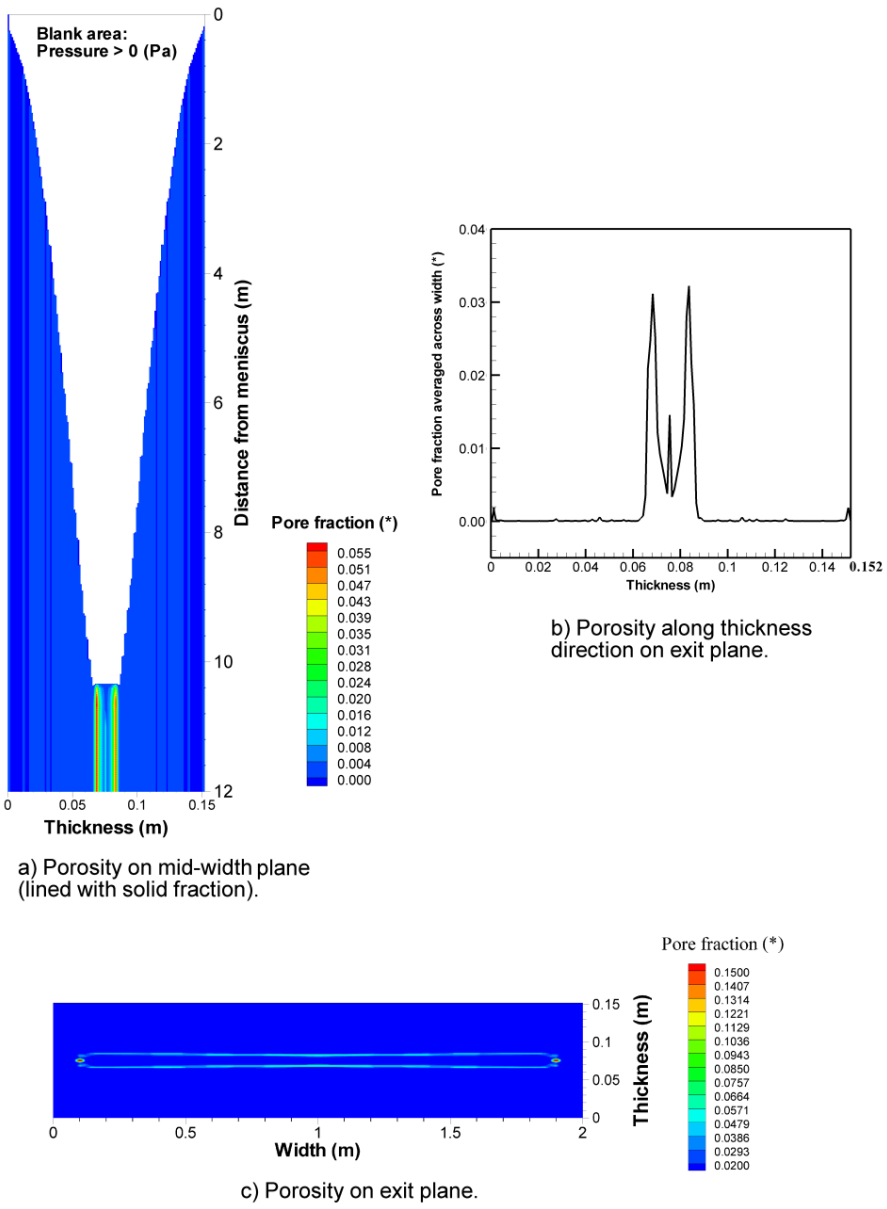

a) Porosity on mid-width plane (lined with solid fraction).

b) Porosity along thickness direction on exit plane.

c) Porosity on exit plane.

Figure 6.8 Porosity results for case 3.

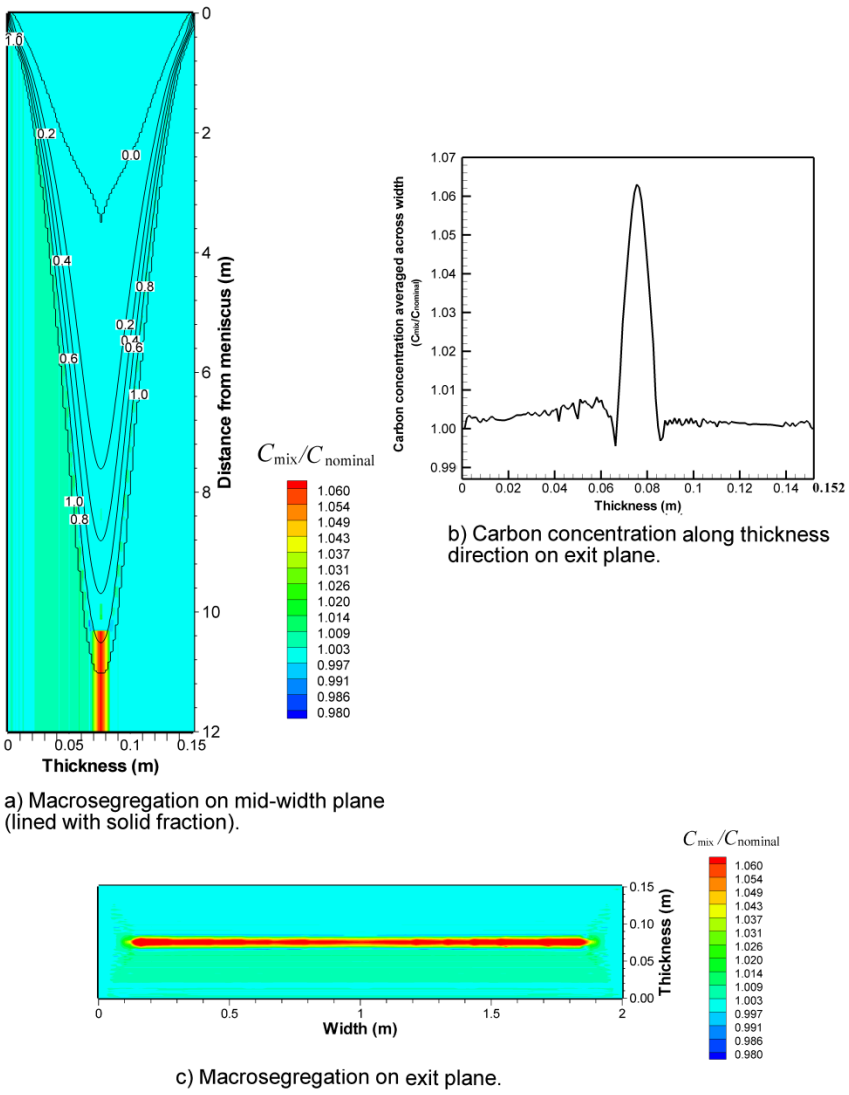

a) Macrosegregation on mid-width plane (lined with solid fraction).

b) Carbon concentration along thickness direction on exit plane.

c) Macrosegregation on exit plane.

Figure 6.9 Macrosegregation results for case 3.

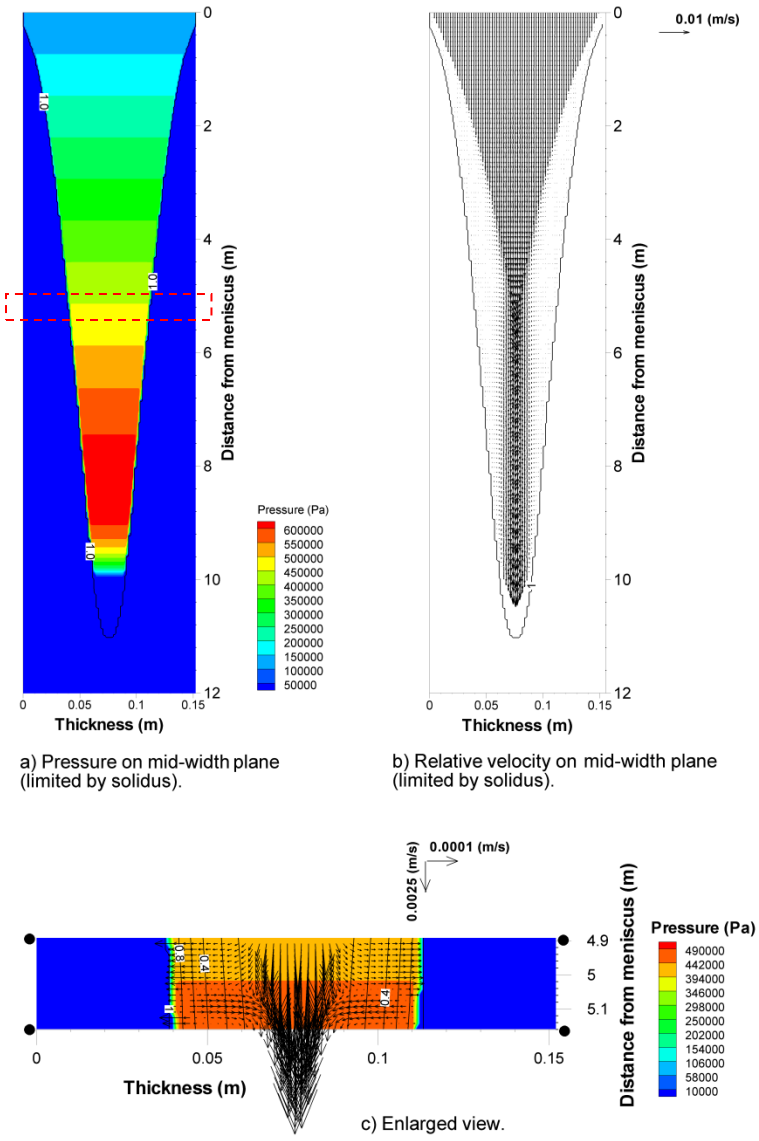

Figure 6.10 Relative velocity and pressure field for case 4.

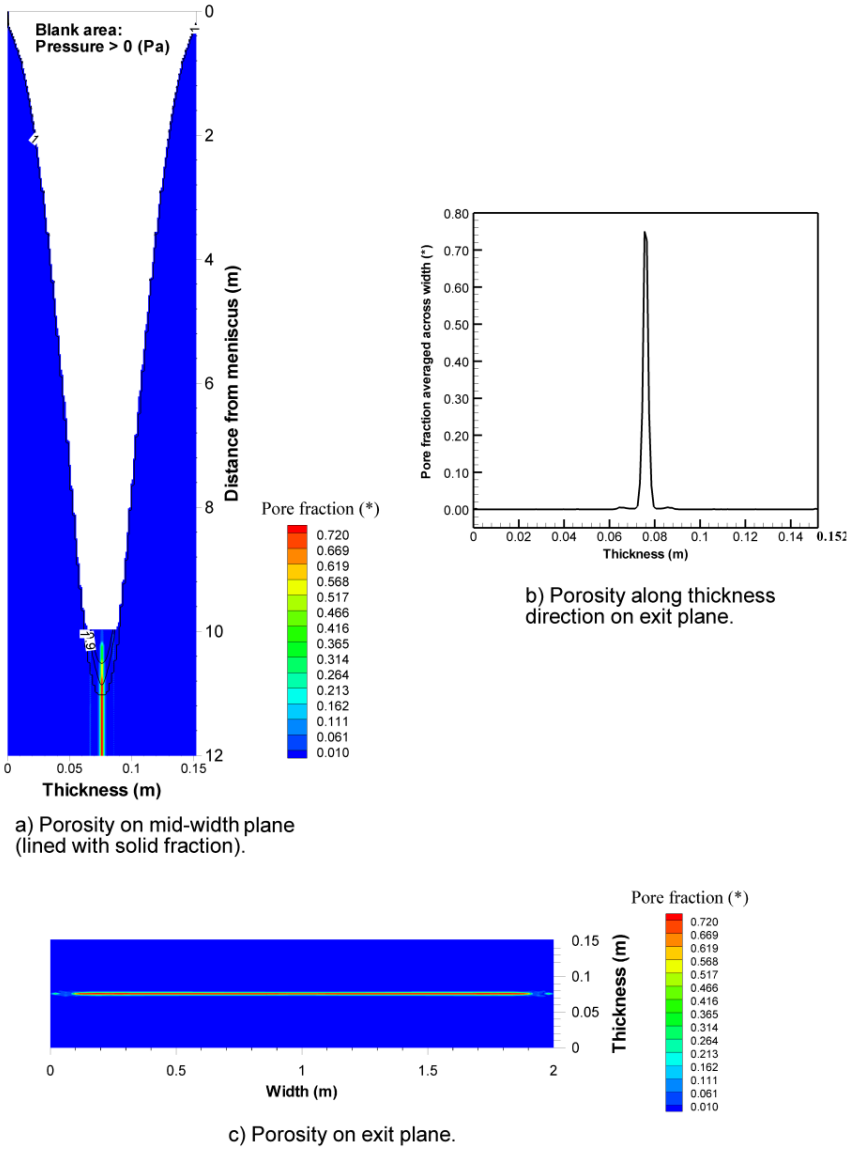

a) Porosity on mid-width plane (lined with solid fraction).

b) Porosity along thickness direction on exit plane.

c) Porosity on exit plane.

Figure 6.11 Porosity results for case 4.

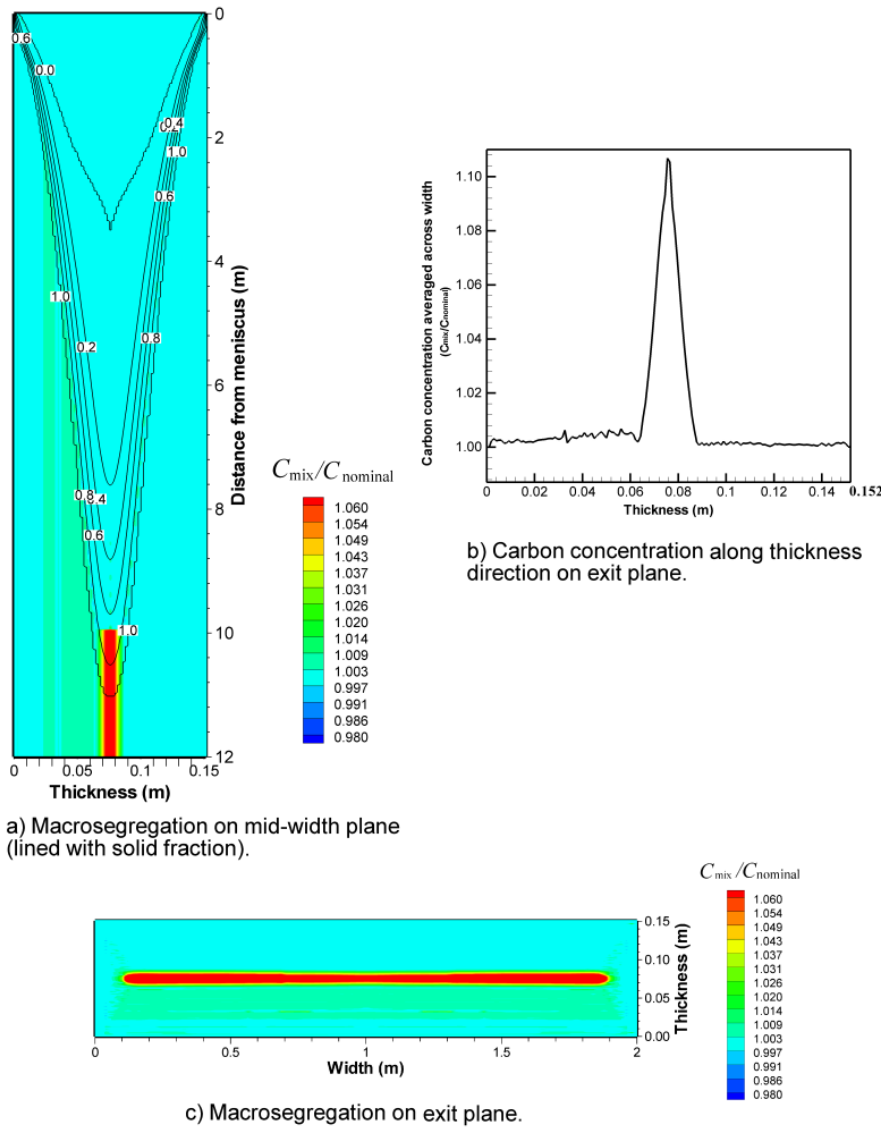

a) Macrosegregation on mid-width plane (lined with solid fraction).

b) Carbon concentration along thickness direction on exit plane.

c) Macrosegregation on exit plane.

Figure 6.12 Macrosegregation results for case 4.

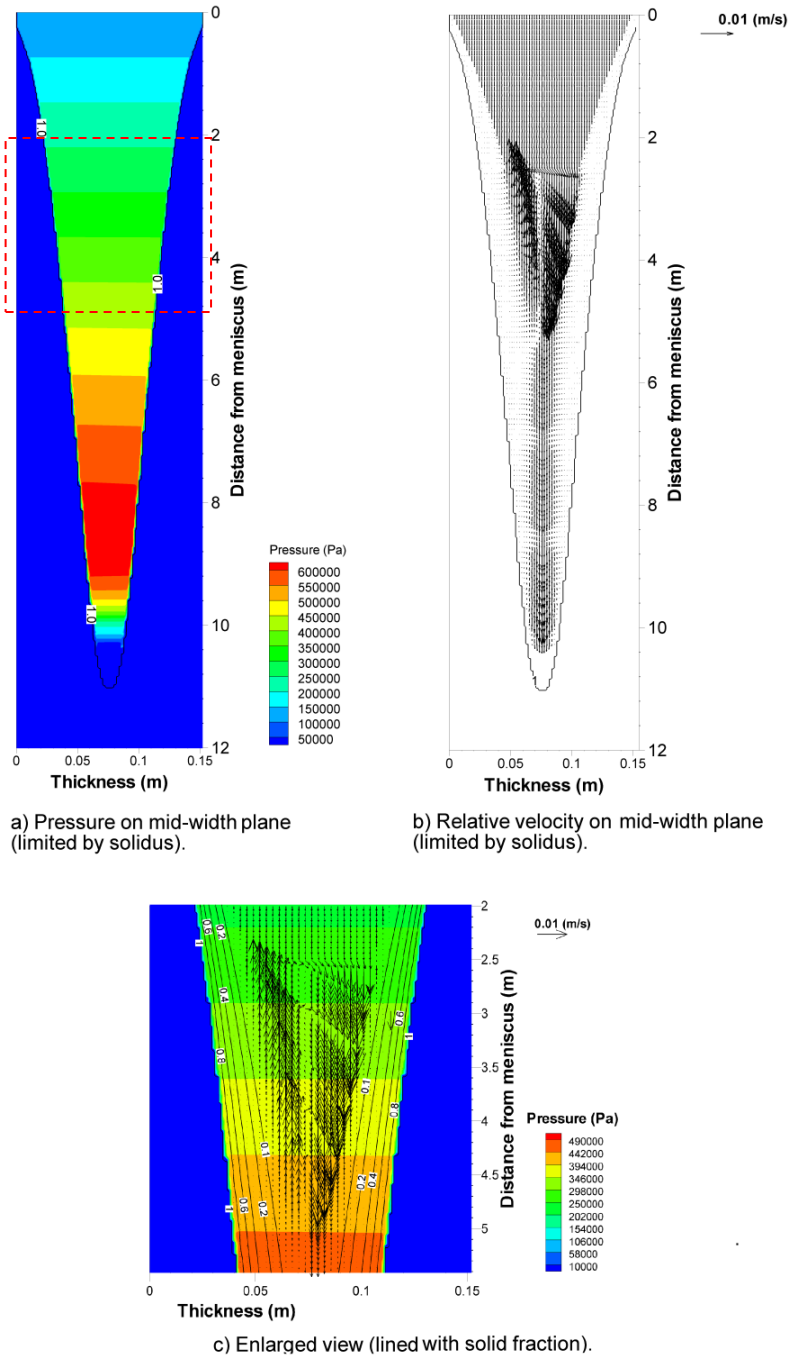

a) Pressure on mid-width plane (limited by solidus).

b) Relative velocity on mid-width plane (limited by solidus).

c) Enlarged view (lined with solid fraction).

Figure 6.13 Relative velocity and pressure field for case 5.

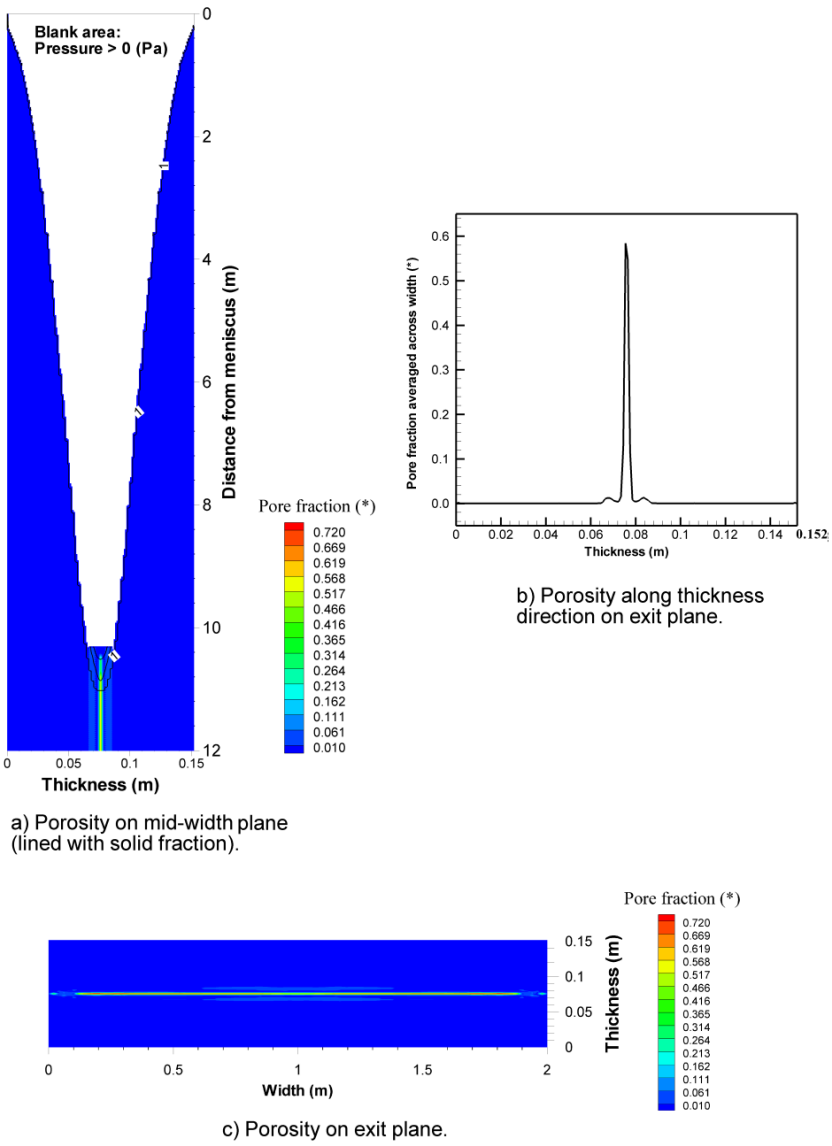

a) Porosity on mid-width plane (lined with solid fraction).

b) Porosity along thickness direction on exit plane.

c) Porosity on exit plane.

Figure 6.14 Porosity results for case 5.

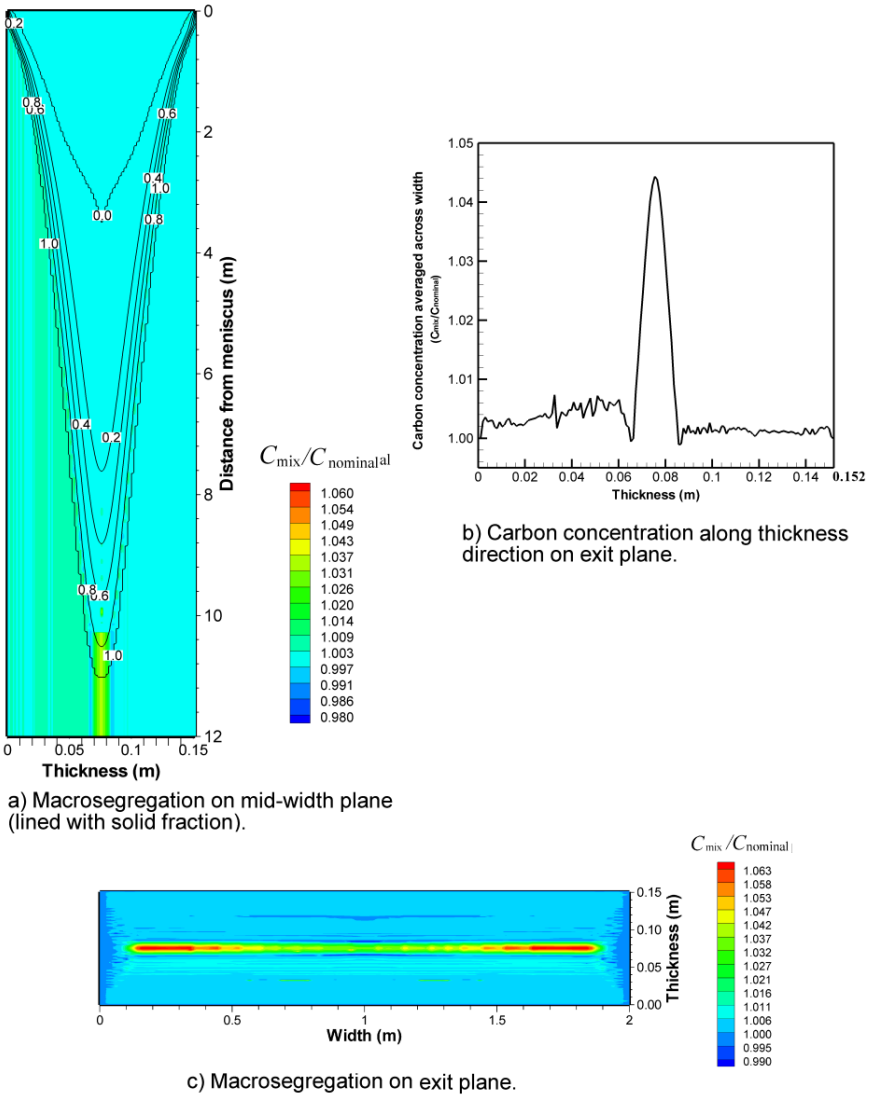

a) Macrosegregation on mid-width plane (lined with solid fraction).

b) Carbon concentration along thickness direction on exit plane.

c) Macrosegregation on exit plane.

Figure 6.15 Macrosegregation results for case 5.

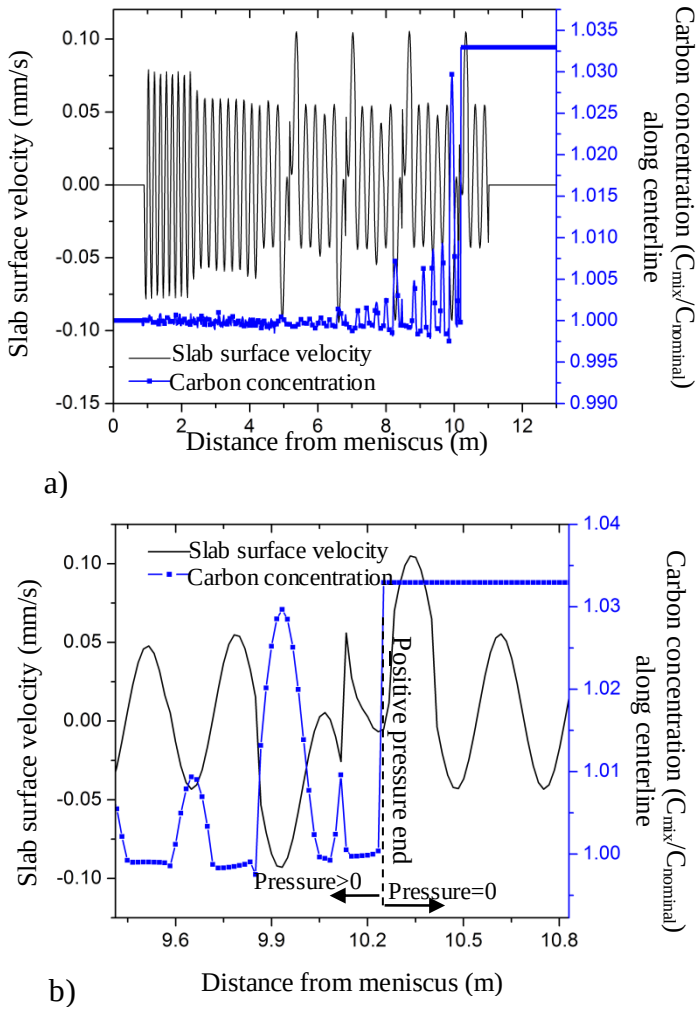

Figure 6.16 Slab surface velocity and carbon concentration along centerline in a) and enlarged view in b).

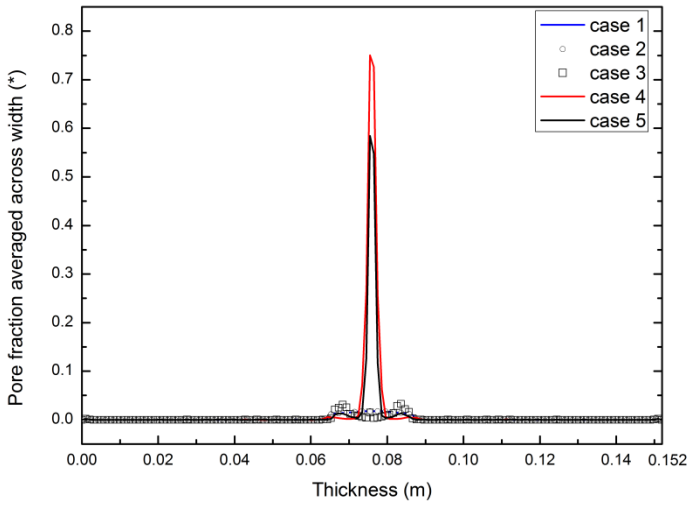

Figure 6.17 Averaged pore fraction along thickness in the final product for different casting conditions (All cases are assumed the same temperature and solid fraction field with the casting speed of 1.3m/min). Case 1: no bulging, constant roll gap, vertical strand; case 2: no bulging, constant roll gap, curved strand; case 3: no bulging, variable roll gap, vertical strand; case 4: with bulging, constant roll gap, vertical strand; case 5: with bulging, variable roll gap, curved strand.

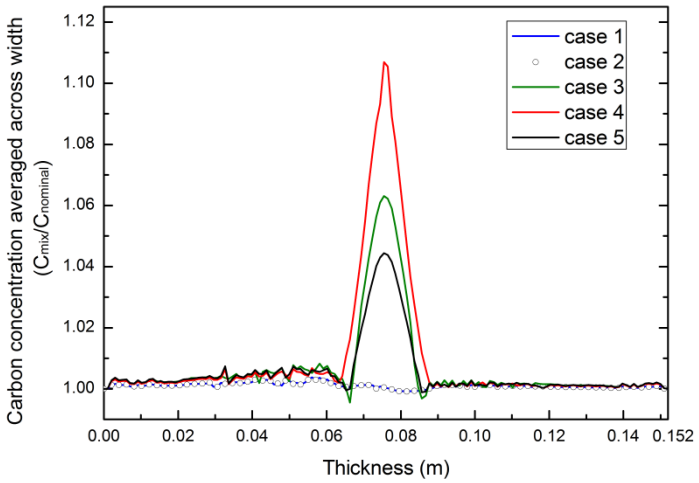

Figure 6.18 Averaged macrosegregation along thickness in the final product for different casting conditions (All cases are assumed the same temperature and solid fraction field with the casting speed of 1.3m/min). Case 1: no bulging, constant roll gap, vertical strand; case 2: no bulging, constant roll gap, curved strand; case 3: no bulging, variable roll gap, vertical strand; case 4: with bulging, constant roll gap, vertical strand; case 5: with bulging, variable roll gap, curved strand.

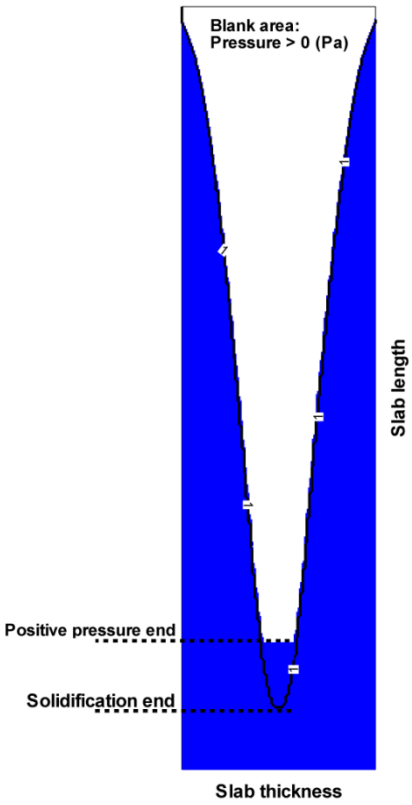

Figure 6.19 Schematic of critical points and region.

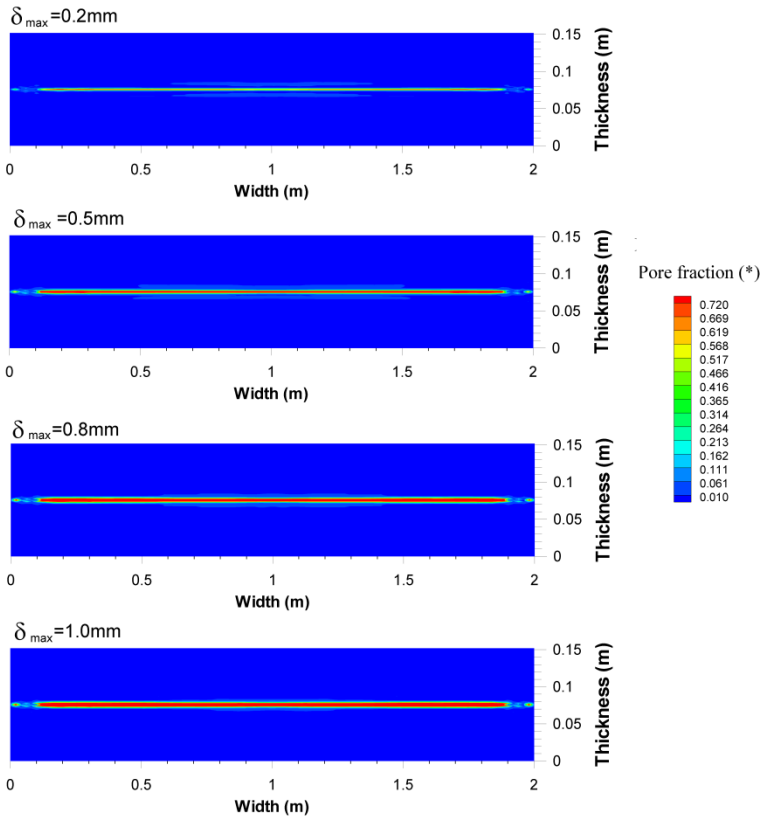

Figure 6.20 Porosity distribution in the final product with different degrees of bulging.

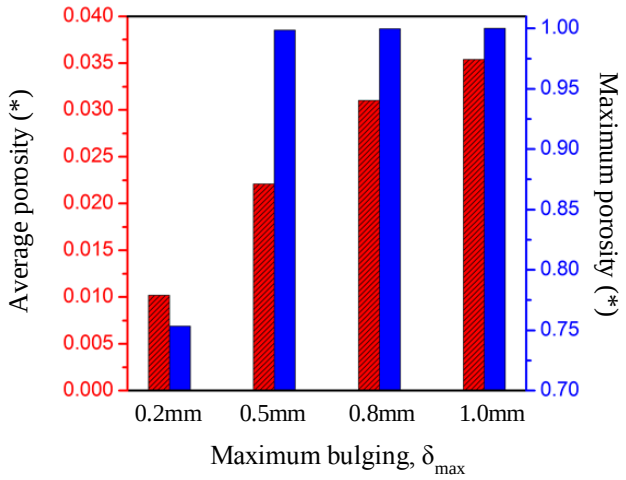

Figure 6.21 Average and maximum porosity in the final product with different degrees of bulging.

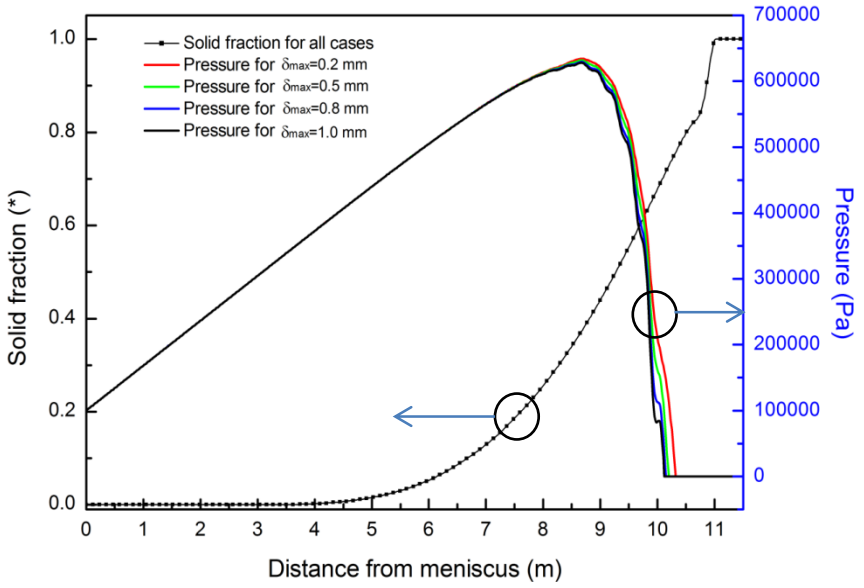

Figure 6.22 Pressure and solid fraction along centerline with different degrees of bulging.

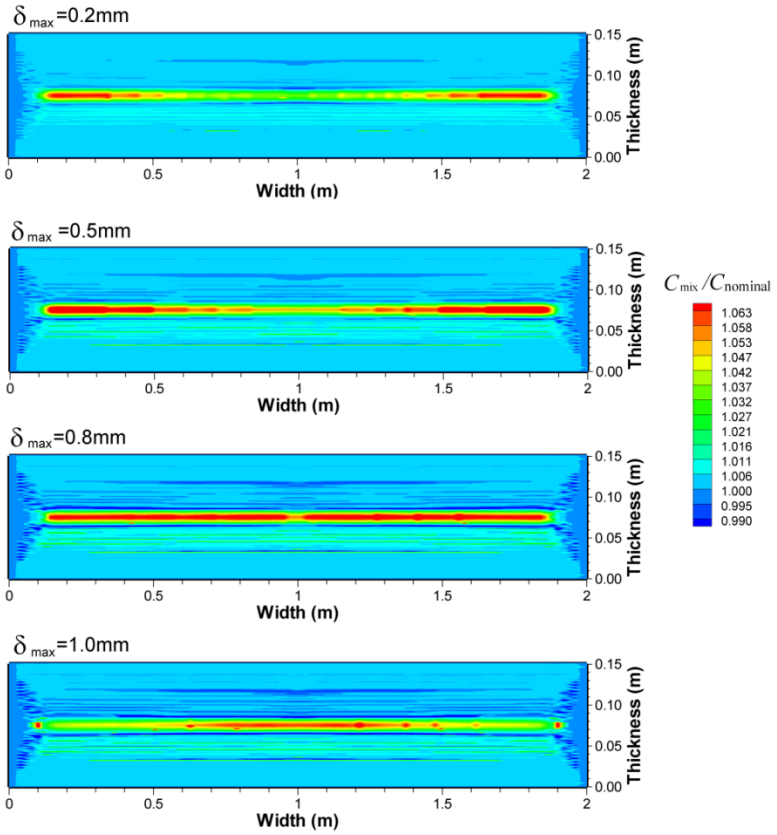

Figure 6.23 Carbon concentration ($C_{mix}/C_{nominal}$) on exit plane with different degrees of bulging.

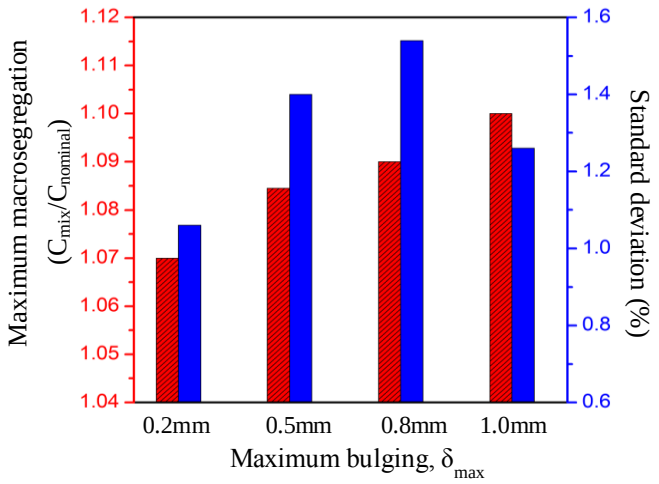

Figure 6.24 Maximum and standard deviation of carbon concentration with different degrees of bulging.

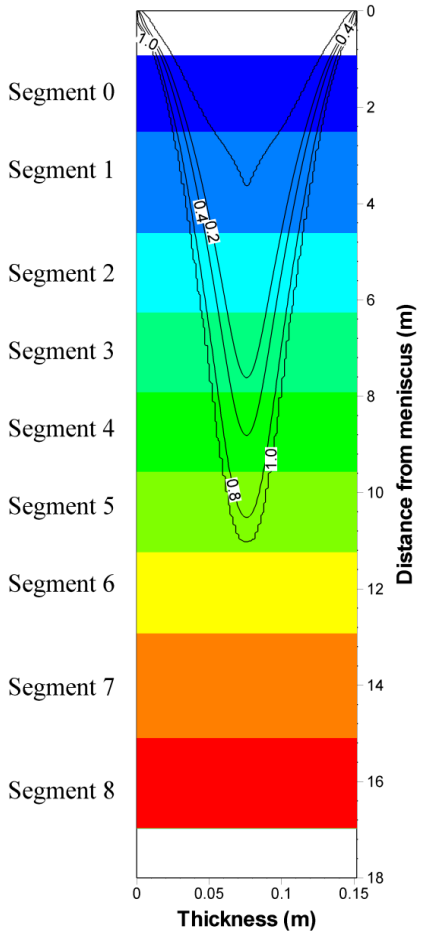

Figure 6.25 Schematic plot of mid-width plane indicating roll segment arrangement; Lined with solid fraction, colored with roll segments (blank area: no roll).

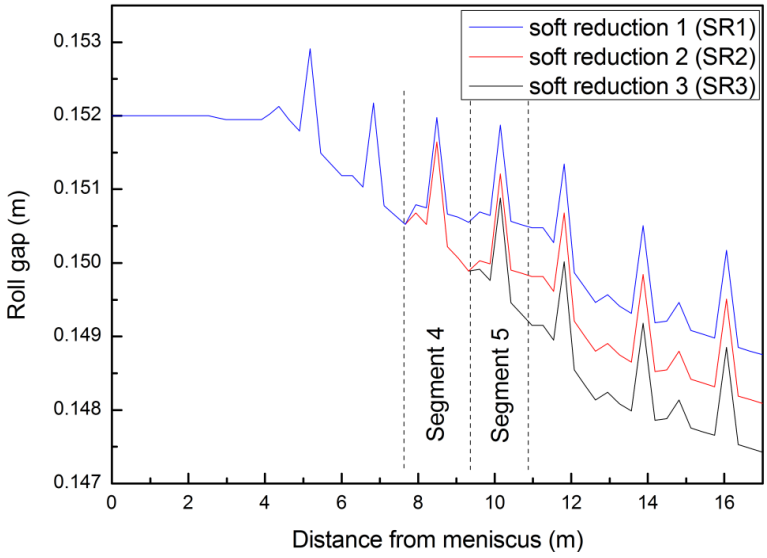

Figure 6.26 Roll arrangements with different degrees of soft reduction.

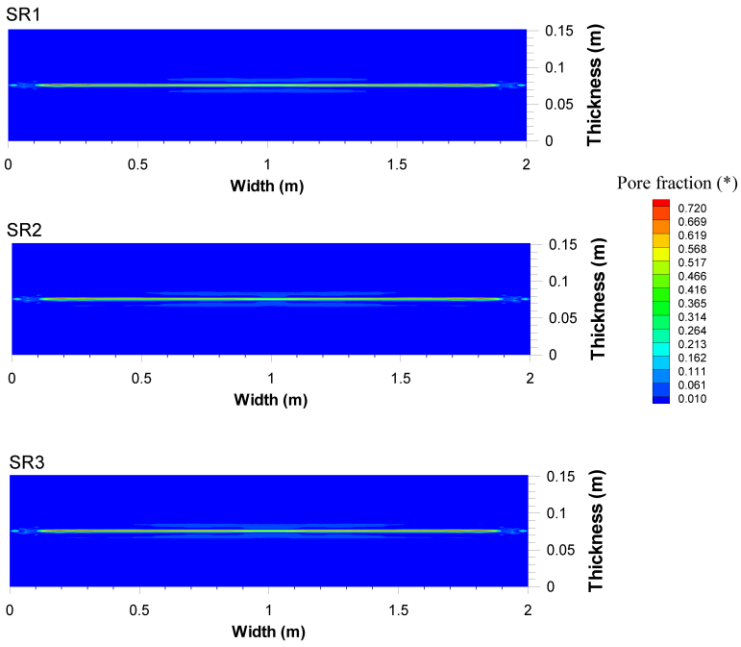

Figure 6.27 Pore fraction on exit plane with different soft reductions.

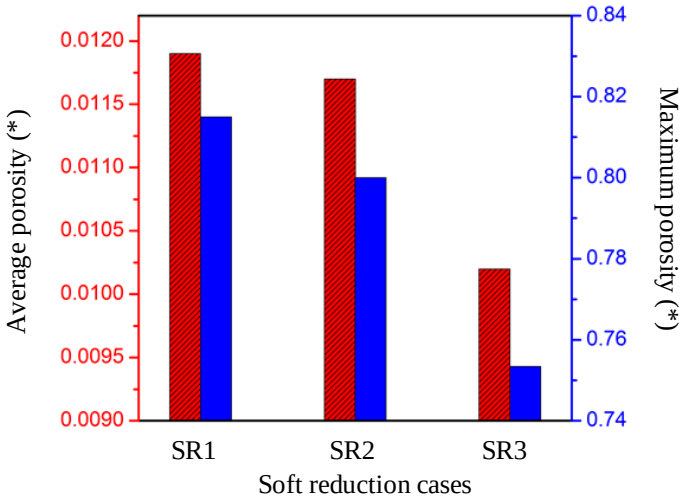

Figure 6.28 Average and maximum porosity on exit plane with different soft reductions.

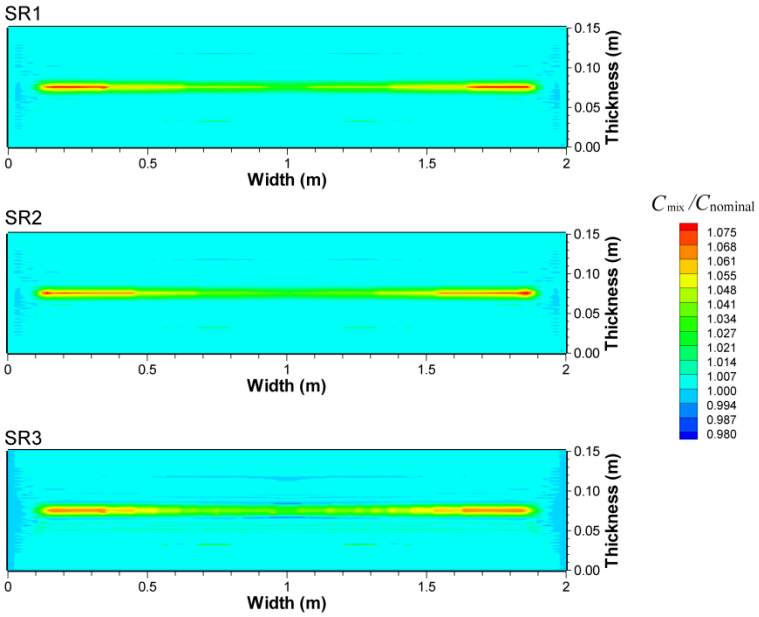

Figure 6.29 Carbon concentration ($C_{mix}/C_{nominal}$)on exit plane with different soft reductions.

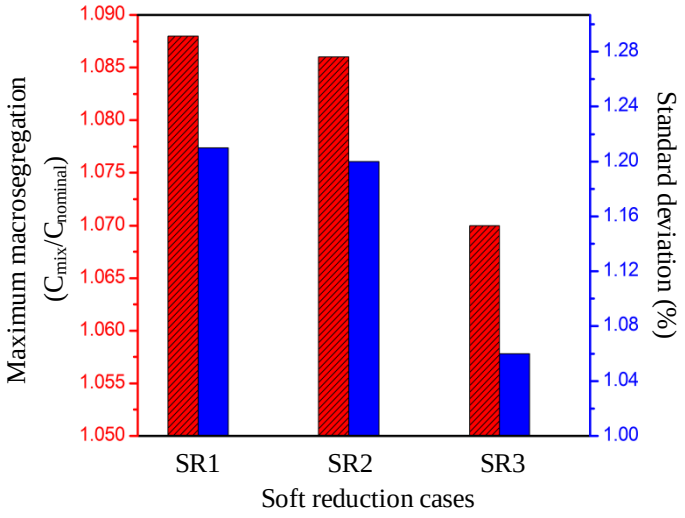

Figure 6.30 Maximum and standard deviation of macrosegregation on exit plane with different soft reductions.

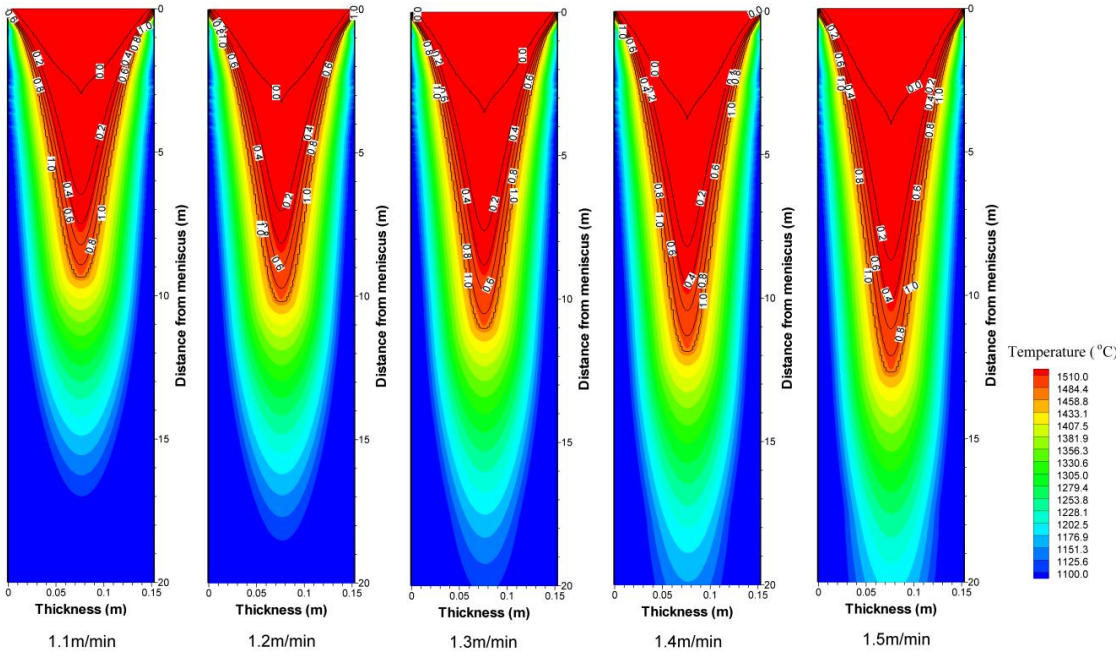

Figure 6.31 Temperature and solid fraction contours with different casting speeds.

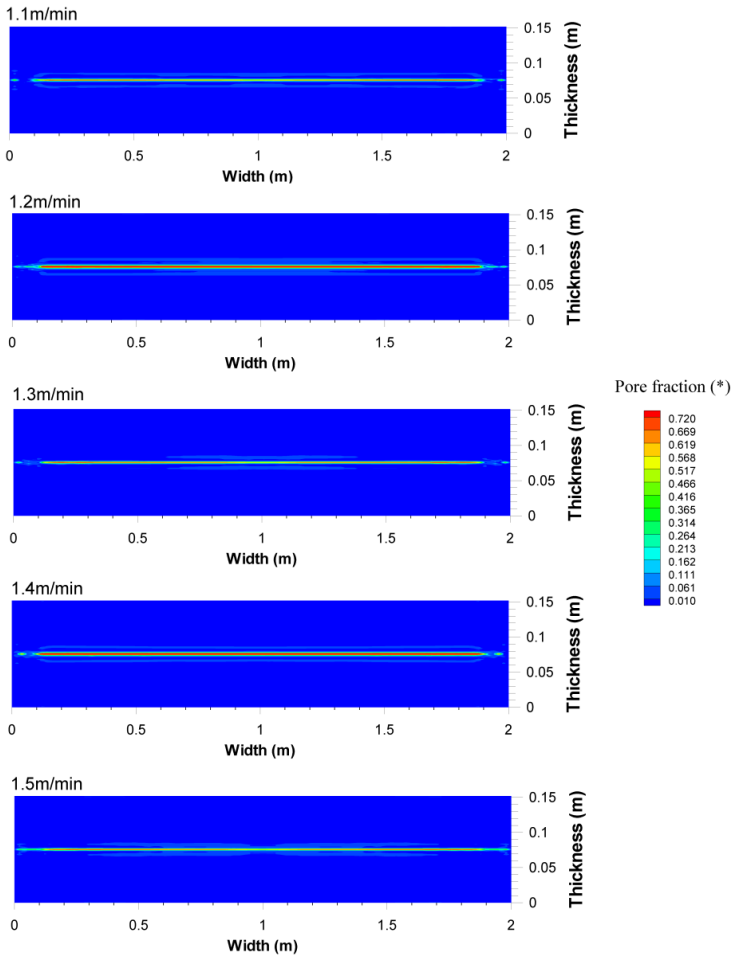

Figure 6.32 Porosity results on the exit plane with different casting speeds.

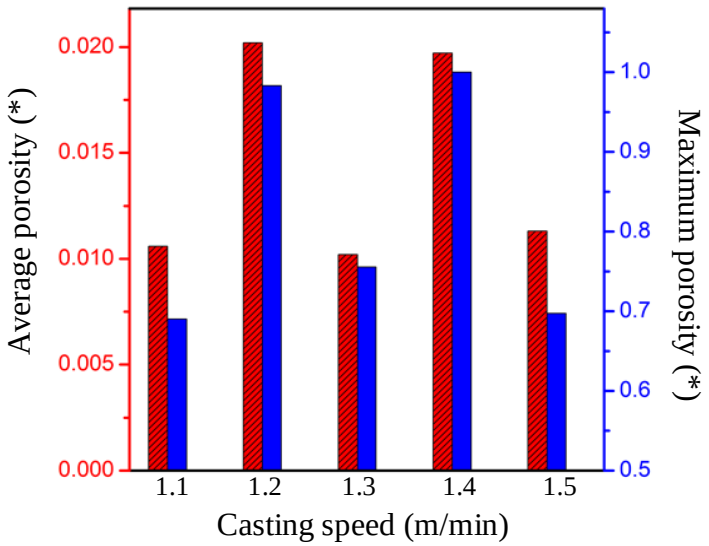

Figure 6.33 Average and maximum porosity in the final products with different casting speeds.

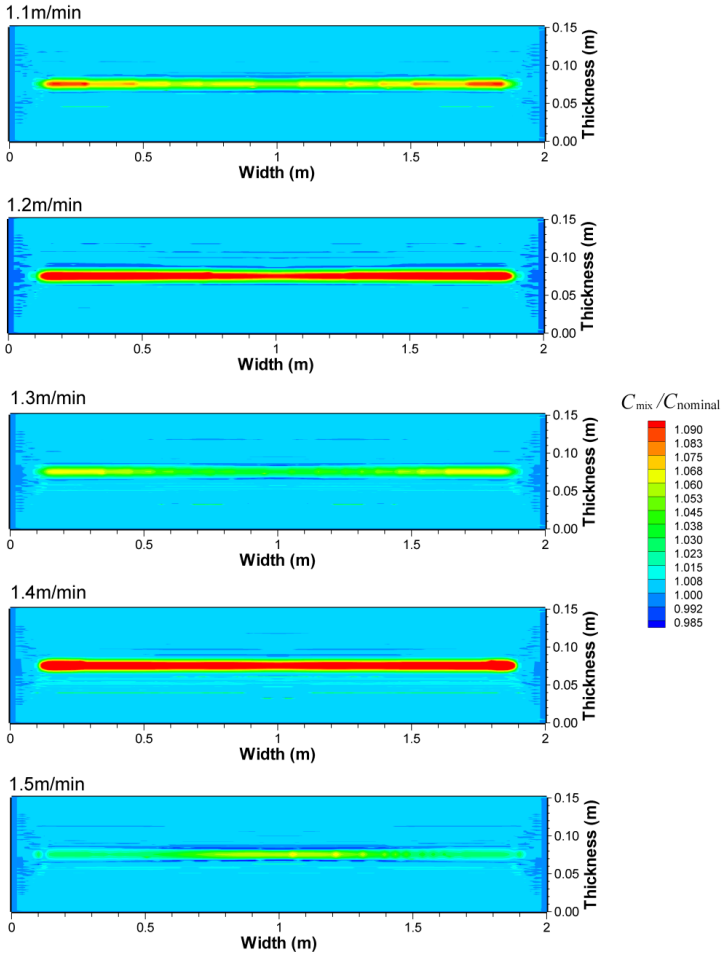

Figure 6.34 Carbon concentration ($C_{mix}/C_{nominal}$) on the exit plane with different casting speeds.

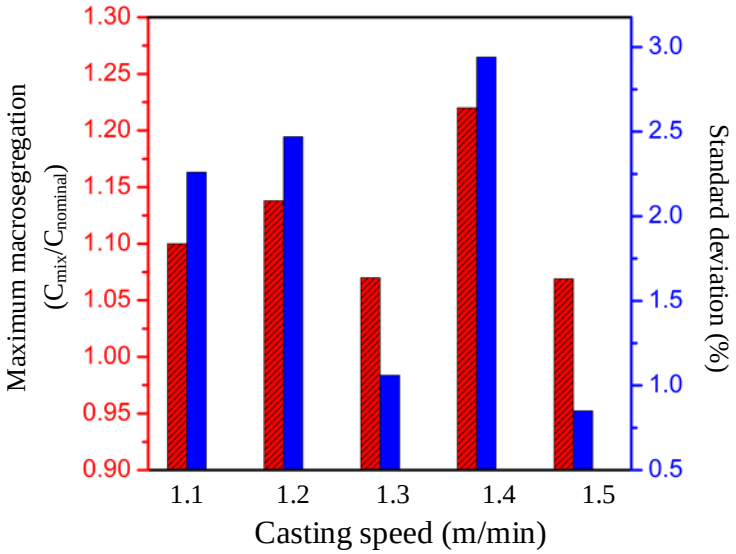

Figure 6.35 Maximum and standard deviation of macrosegregation on exit plane with different casting speeds.

CHAPTER VII

CONCLUTIONS AND RECOMMENDATIONS

7.1 Conclusions

Although the porosity and macrosegregation defects have been the research subjects for the last few decades, there are still problems not solved. Earlier studies on porosity considered only gas porosity and shrinkage porosity. Work on porosity formation due to solid deformation is rare. Most importantly porosity modeling during continuous casting of steel has not been reported. For macrosegregation, there are a few models able to give concentration peak at the centerline, however, porosity formation is not considered in these previous researches. The present thesis performs the study of porosity and macrosegregation due to both solid deformation and shrinkage effect during the continuous casting of steel.

Firstly, the governing equations are derived. Multiphase transport equations are presented accounting for three phases: solid, liquid and porosity. These equations include mass, momentum and species conservation equations. The mass and momentum conservation is combined to derive the pressure equation. The porosity is determined by solving continuity equation at where liquid pressure drops to zero. For solid deformation velocity in pressure and macrosegregation equations, it is modeled using simple algebraic equations with assumed slab surface deflection.

Then the liquid pressure model has been validated by a simplified case. Full featured case with real casting conditions is performed on different meshes to find reasonable grid size to run the calculation.

Finally, the proposed model is applied to different casting conditions to study the relation between operating conditions and defects, i.e., porosity and macrosegregation.

Predictions, with and without solid deformation, are done and the results show the necessity to include solid deformation for porosity and macrosegregation predictions.

Investigations are performed with different casting conditions: varying degree of bulging, soft reduction and casting speeds.

It is clear that higher degree of bulging increases porosity while further soft reduction mitigates porosity. Since for different casting speeds, the thermal fields are not the same, the regions of porosity formation lie in different solid deformation environments. As a result of this, there is no clear relation between casting speed and porosity level in the final product.

The comparison of macrosegregation results with and without solid deformation shows that solid deformation is the main cause of centerline macrosegregation. The magnitude of macrosegregation in final product is case dependent with regard to degree of bulging and casting speed. However, it is clear that soft reduction is able to alleviate macrosegregation due to the inward movement of solute-poor solid phase. So, in the design of roll arrangement, compression is preferred near positive pressure end.

7.2 Recommendations for Future Research

While the present work represents considerable progress in the modeling of porosity formation and macrosegregation in continuous casting of steel, there are some areas that require further consideration to improve the precision. The recommended improvements include:

1. More accurate thermal field calculation model is needed, so as to reduce grid independence. Current used thermal model predicts solidification end by a noticeable difference on different meshes. The extent of solidification end can vary by 0.3 m (see Figure 5.22) along casting direction. As shown in Chapter V, this grid dependence leads to different porosity and macrosegregation results on different meshes. A more accurate thermal field model should be independent of size of mesh and helps reduce calculation by using coarse mesh.

2. Current macrosegregation model considers only solid movement due to bulging and variable roll gap, however, the formation and settling of free dendrite also influence the centerline macrosegregation. It is also desirable to include the effects of thermal contraction on solid phase velocity.

3. Even for solid deformation due to bulging and variable roll gap, the method used in current research is based on assumed surface deflection. Since solid deformation is essential in prediction of porosity and macrosegregation, more advanced solid deformation model based on thermal mechanical analysis is needed.

4. Many phenomena (i.e., heat transfer, phase change, fluid flow, solid deformation, multi-scale species transportation) appear simultaneously during the continuous casting process; however, they are uncoupled and calculated in a sequential manner. The ultimate goal should be deriving a model where all phenomena are coupled.

REFERENCES

1. Institute, A.I.a.S., *American Iron and Steel Institute, "Saving one barrel of oil per ton: A new roadmap for transformation of steelmaking process"*, 2005.

2. Miyazawa, K. and K. Schwerdtfeger, *Macrosegregation in continuously cast steel slabs: preliminary theoretical investigation on the effect of steady state bulging.* Arch. Eisenhutten, 1981. **52**(11): p. 415-422.

3. Koric, S. and B.G. Thomas, *Thermo-mechanical models of steel solidification based on two elastic visco-plastic constitutive laws.* Journal of Materials Processing Technology, 2008. **197**(1–3): p. 408-418.

4. Wang, E.-G. and J.-C. He, *Finite element numerical simulation on thermo-mechanical behavior of steel billet in continuous casting mold.* Science and Technology of Advanced Materials, 2001. **2**(1): p. 257-263.

5. Campbell, J., *Castings*. 2ed 2003, Oxford: Elsevier Butterworth-Heinemann.

6. Campbell, J., *Casting practice: The 10 rules of castings*, 2004, Oxford: Elsevier Butterworth-Heinemann.

7. G., L., *Macrosegregation in steel strands and ingots: Characterisation, formation and consequences.* Materials Science and Engineering: A, 2005. **413–414**(0): p. 19-29.

8. Griffiths, W.D. and D.G. McCartney, *The effect of electromagnetic stirring on macrostructure and macrosegregation in the aluminium alloy 7150.* Materials Science and Engineering: A, 1997. **222**(2): p. 140-148.

9. Zhang, B., J. Cui, and G. Lu, *Effect of low-frequency magnetic field on macrosegregation of continuous casting aluminum alloys.* Materials Letters, 2003. **57**(11): p. 1707-1711.

10. Sang, B., X. Kang, and D. Li, *A novel technique for reducing macrosegregation in heavy steel ingots.* Journal of Materials Processing Technology, 2010. **210**(4): p. 703-711.

11. Sivesson, P., C.M. Raihle, and J. Konttinen, *Thermal soft reduction in continuously cast slabs.* Materials Science and Engineering: A, 1993. **173**(1–2): p. 299-304.

12. A., R., et al., *Strand reduction in continuous casting and its effect on product quality*, 2002.

13. Ginzburg, V.B. and R. Ballas, *Flat rolling fundamentals* 2000, New York: Marcel Dekker, Inc.

14. Thomas, B.G., *Continuous Casting*2001, The Encyclopedia of Materials: Science and Technology: Elsevier Science Ltd.

15. Pascon, F. and A.M. Habraken, *Finite element study of the effect of some local defects on the risk of transverse cracking in continuous casting of steel slabs*. Computer Methods in Applied Mechanics and Engineering, 2007. **196**(21–24): p. 2285-2299.

16. Dalin, J.B. and J.L. Chenot, *Finite element computation of bulging in continuously cast steel with a viscoplastic model.* lnternat. J. Numer. Methods Engrg., 1988. **25**: p. 147-163.

17. Campbell, J., *Complete Casting Handbook: Metal Casting Processes, Techniques and Design*2011: Butterworth-Heinemann Ltd.

18. Grasso, P.-D., J.-M. Drezet, and M. Rappaz, *Hot tear formation and coalescence observations in organic alloys*. JOM-e, 2002.

19. Flemings, M.C., *Our understanding of macrosegregation. Past and Present*. 2000. **40**(9): p. 833-841.

20. G, L., *Macrosegregation in steel strands and ingots: Characterisation, formation and consequences*. Materials Science and Engineering: A, 2005. **413–414**(0): p. 19-29.

21. Bennon, W.D. and F.P. Incropera, *A continuum model for momentum, heat and species transport in binary solid-liquid phase change systems—I. Model formulation*. International Journal of Heat and Mass Transfer, 1987. **30**(10): p. 2161-2170.

22. P.J. Prescott, F.P.I., W.D. Bennon, *Modelling of dendritic solidification systems: reassessment of the continuum momentum equation*. Int. J. Heat Mass Transfer, 1991. **34**: p. 2351-2359.

23. Ni, J. and C. Beckermann, *A volume-averaged two-phase model for solidification transport phenomena*. Metall. Trans. B, 1991. **Vol. 22B**: p. 349-361.

24. Won, Y.M., et al., *Effect ot cooling rate on ZST. LIT and ZDT of carbon steels near melting point*. ISIJ International, 1998. **38**: p. 1093-1099.

25. Wang, C.Y. and C. Beckermann, *A multiphase solute diffusion model for dendritic alloy solidification*. Metall. Trans. A, 1993. **24A**: p. 2787-2802.

26. Brody, H. and M.C. Flemings, *Solute redistribution in dendritic solidification*. Trans. Metall. Soc. AIME, 1966. **236**: p. 615–624.

27. H. Combeau, et al., *Modeling of microsegregation in macrosegregation computations*. Metall. Mater. Trans. A, 1996. **27A**: p. 2314–2327.

28. Wang, C.Y. and C. Beckermann, *A unified solute diffusion model for columnar and equiaxed dendritic alloy solidification*. Mater. Sci. Eng. A, 1993. **171A**: p. 199-211.

29. Louhenkilpi, S., 1995, The Finnish Academy of Technology: Helsinki.

30. Alizadeh, M., H. Edris, and A. Shafyei, *Mathematical modeling of heat transfer for steel continuous casting process*. International Journal of ISSI, 2006. **3**: p. 7-16.

31. Louhenkilpi, S., E. Laitinen, and R. Nieminen, *Real-time simulation of heat transfer in continuous casting*. Metallurgical Transactions B, 1993. **24B**: p. 685-693.

32. Miettinen, J., Metall. Trans. A, 1992. **23A**: p. 1155-1170.

33. Hardin, R.A., et al., *A Transient Simulation and Dynamic Spray Cooling Control Model for Continuous Steel Casting*. Metallurgical and Materials Transactions B, 2003. **34B**: p. 297-306.

34. Louhenkilpi, S., et al., *3D steady state and transient simulation tools for heat transfer and solidification in continuous casting*. Materials Science and Engineering: A, 2005. **413–414**: p. 135-138.

35. M, E.-B., L. N, and F. H., *Simulation of cooling conditions in secondary cooling zones in continuous casting process*. Ironmaking and Steelmaking, 1995. **22**(3): p. 246-255.

36. Shen, H.F., et al., *Simulation using Realistic Spray Cooling for the Continuous Casting of Multi-Component Steel.* J. Materials Science and Technology, 2002. **18**: p. 311-314.

37. Hardin, R.A., H. Shen, and C. Beckermann. *Heat transfer modeling of continuous steel slab sasters using realistic spray patterns*. in *Modeling of Casting, Welding and Advanced Solidification Processes IX*. 2000. Germany: Shaker Verlag.

38. Hardin, R., P. Du, and C. Beckermann, *Three-dimensional Simulation of Heat Transfer and Stresses in a Steel Slab Caster*, in *Heat transfer*2011: Düsseldorf.

39. Wang, C.Y. and C. Beckermann, *A Multiphase Solute Diffusion Model for Dendritic Alloy Solidification*. Metall. Trans. A, 1993. **24A**: p. 2787-2802.

40. Mehrabian, R., M. Keane, and M.C. Flemings, *Interdendritic fluid flow and macrosegregation; influence of gravity*. Metallurgical and Materials Transactions B, 1970. **1**(5): p. 1209-1220.

41. Fujii, T., D.R. Poirier, and M.C. Flemings, *Macrosegregation in a multicomponent low alloy steel.* Metallurgical and Materials Transactions B, 1979. **10**(3): p. 331-339.

42. *Optimum field squeezing from atomic sources: Three-level atoms*. Physical Review A, 1994. **50**(3): p. 2646.

43. Ridder, S.D., S. Kou, and R. Mehrabian, *Effect of fluid flow on macrosegregation in axi-symmetric ingots*. Metallurgical and Materials Transactions B, 1981. **12**(3): p. 435-447.

44. Szekely, J. and A. Jassal, *An experimental and analytical study of the solidification of a binary dendritic system*. Metallurgical and Materials Transactions B, 1978. **9**(4): p. 389-398.

45. Bennon, W.D. and F.P. Incropera, *A continuum model for momentum, heat and species transport in binary solid-liquid phase change systems—II. Application to solidification in a rectangular cavity.* International Journal of Heat and Mass Transfer, 1987. **30**(10): p. 2171-2187.

46. Ni, J. and C. Beckermann, *A Volume-Averaged Two-Phase Model for Solidification Transport Phenomena.* Metall. Trans. B, 1991. **22B**: p. 349-361.

47. Kumar, A., M. Založnik, and H. Combeau, *Study of the influence of mushy zone permeability laws on macro- and meso-segregations predictions.* International Journal of Thermal Sciences, 2012. **54**(0): p. 33-47.

48. Thevik, H.J. and A. Mo, *The influence of micro-scale solute diffusion and dendrite coarsening upon surface macrosegregation.* Int. J. Heat Mass Transfer, 1997. **40 (9)**: p. 2055–2065.

49. Nielsen, Ø., et al., *Experimental determination of mushy zone permeability in aluminum-copper alloys with equiaxed microstructures.* Metall. Mater.Trans. A, 1999. **30A**: p. 2455–2462.

50. M'Hamdi, M., A. Mo, and H.G. Fjær, *TearSim: A two-phase model addressing hot tearing formation during aluminum direct chill casting.* Metallurgical and Materials Transactions A, 2005. **37**: p. 3069-3083.

51. Boehmer, J.R., F.N. Fett, and G. Funk, *Analysis of high-temperature behaviour of solidified material within a continuous casting machine.* Computers & Structures, 1993. **47**(4–5): p. 683-698.

52. Sorimachi, K. and T. Emi, *Elastoplastic stress analysis of bulging as a major cause of internal crack in continuous cast slabs.* The Iron and Steel Institute of Japan (ISIJ), 1977. **63**: p. 1297-1304.

53. Grill, A. and K. Schwerdtfeger, *Finite element analysis of bulging produced by creep in continuously cast slabs.* Ironmaking Steelmaking, 1979. **6**: p. 131-135

54. SAEKI, T., et al., *Effect of bulging and solidification structure on segregation in continuously cast slab.* Transactions ISIJ, 1984. **24**(11): p. 907-916.

55. Bellet, M. and V.D. Fachinotti, *A two-phase two-dimentional fite element thermonechanics and macrosegregation model of mushy zone. Application to Continuous Casting*, in *11th Int. Conf. on Modeling of Casting, Welding and Advanced Solidification Processes*, C.A. Gandin and M. Bellet, Editors. 2006, The Minerals, Metals & Materials Society: Opio, France. p. 169-176.

56. Forestier, R., et al. *Finite element thermomechanical simulation of steel continuous casting*. in *12th Int. Conf. on Modeling of Casting, Welding and Advanced Solidification Processes*. 2009. Vancouver & Alaska: The Minerals, Metals & Materials Society.

57. Boehmer, J.R., et al., *Strategies for coupled analysis of thermal strain history during continuous solidification processes.* Advances in Engineering Software, 1998. **29**(7–9): p. 679-697.

58. Pascon, F., et al. *Finite element modelling of thermo-mechanical behaviour of a steel strand in continuous casting*. in *Proceedings of the 7th European Conference on Advanced Materials and processes*. 2001. Rimini, Italy.

59. Li, C. and B.G. Thomas, *Thermomechanical finite-element model of shell behavior in continuous casting of steel.* Metallurgical and Materials Transactions B, 2004. **35**: p. 1151-1172.

60. Lee, J.-E., et al., *Prediction of Cracks in Continuously Cast Steel Beam Blank through Fully Coupled Analysis of Fluid Flow, Heat Transfer, and Deformation Behavior of a Solidifying Shell.* Metallurgical and Materials Transactions A, 1998: p. 225-237.

61. Inoue, T. and K. Z. G. Wang, *Thermal and mechanical fields in continuous casting slab --A steady state analysis incorporating solidification.* A steady state analysis incorporating solidification, 1988. **58**: p. 265-275.

62. Rammerstrofer, et al., *Temperature fields, solidification progress and stress development in the strand during a continuous casting process of steel*, in *Numerical Methods in Thermal Problems*1979, Pineridge Press. p. 712-722.

63. Park, J.K., et al., *Thermal and Mechanical Behavior of Copper Molds during Thin-Slab Casting (II): Mold Crack Formation.* Metallurgical and Materials Transactions B, 2002. **33B**: p. 437-449.

64. Park, J.K., et al., *Thermal and mechanical behavior of copper molds during thin-slab casting (I): Plant trial and mathematical modeling.* Metallurgical and Materials Transactions B, 2002. **33**: p. 425-436.

65. Grill, A., J.K. Brimacombe, and F. Weinberg, *Mathematical analysis of stresses in continuous casting of steel.* Ironmaking and Steelmaking, 1976. **3**: p. 38-47.

66. Sorimachi, K. and J.K. Brimacombe, *Improvements in mathematical modelling of stresses in continuous casting of steel.* Ironmaking and Steelmaking, 1977. **4**: p. 240-245.

67. Kristiansson, J.O., J. Thermal Stresses, 1984. **7**: p. 209-226.

68. Pascon, F., *2D1/2 thermal-mechanical model of CC of steel using the finite element method*, 2003, University of Liège: Belgium.

69. A., G. and S. K., *Finite-element analysis of bulging produced by creep in continuously cast steel slabs.* Ironmaking and Steelmaking, 1979. **6**(3): p. 131-135.

70. Huespe, A.E., A. Cardona, and V. Fachinotti, *Thermomechanical model of a continuous casting process.* Computer Methods in Applied Mechanics and Engineering, 2000. **182**(3–4): p. 439-455.

71. Bellet, M. and A. Heinrich, *A two-dimensional finite element thermomechanical approach to a global stress-strain analysis of steel continuous casting.* ISIJ International, 2004. **44**: p. 1686-1695.

72. Costes, F., A. Heinrich, and M. Bellet. *3D thermomechanical simulation of the secondary cooling zone of steel continuous casting*. in *10th Int. Conf. on Modeling of Casting, Welding and Advanced Solidification Processes*. 2003. Pennsylvania, USA: The Minerals, Metals & Materials Society.

73. Lee, P.D., A. Chirazi, and D. See, *Modeling microporosity in aluminum–silicon alloys: a review.* Journal of Light Metals, 2001. **1**(1): p. 15-30.

74. Walther, W.D., C. Adams, and W.S. Pellini, *Mechanism for pore formation in. solidifying metals.* AFS Transactions, 1956. **64**: p. 658-664.

75. Piwonka, T.S. and M.C. Flemings, *Pore formation in solidificaiton.* Transactions of the Metallurgical Society of AIME, 1966. **236**: p. 1157-1165.

76. Niyama, E., et al., *Prediction shrinkage in large steel casting from temperature gradient calculations.* International Cast Metals Journal, 1981. **6**(2): p. 16-22.

77. Niyama, E., T. Uchida, and M. Morikawa, *A method of shrinkage prediction and its application to steel casting practice.* International Cast Metals Journal, 1982. **54**: p. 507-516.

78. Sahm, P.R. and P.N. Hansen. *How to model and simulate the feeding process in sasting to predict shrinkage and porosity formation*. in *Modeling of Casting and Welding Processes IV*. 1988. Warrendale, PA: TMS-AIME.

79. Lee, Y.W., E. Chang, and C.F. Chieu, *Modeling of feeding behaviour of solidifying AI-7Si-0.3Mg alloy plate castings.* Metall. Mater. Trans. B, 1990: p. 715-722.

80. Kubo, K. and R. Pehlke, *Mathematical-modeling of porosity formation in solidification.* Metallurgical Transactions B-Process Metallurgy, 1985. **16**(2): p. 359.

81. Pequet, C., M. Gremaud, and M. Rappaz, *Modeling of microporosity, macroporosity, and pipe-shrinkage formation during the solidification of alloys using a mushy-zone refinement method: Applications to Aluminum Alloys.* Metallurgical and Materials Transactions A, 2002. **33A**: p. 2095-2106.

82. Ampuero, J., A.F.A. Hoadly, and M. rappaz, *Modelling of microporosity evolution during the solidification of metallic alloys*, in *Modeling of Casting, Welding and Solidification Processes, V*, 1991. p. 449-454.

83. Ampuero, J., et al., *Modeling of microporosity evolution during the solidification of metallic alloys.* Materials Processing in the Computer Age, 1991: p. 377-388.

84. Flemings, M.C. and G.E. Nereo, *Macrosegregation,. Part. I,.* Trans. TMS-AIME, 1967. **239**: p. 1449.

85. Kajatani, T., J.-M. Drezet, and M. Rappaz, *Numerical simulation of deformation-induced segregation in continuous casting of steel.* Metallurgical and Materials Transactions A, 2001. **32A**: p. 1479-1491.

86. R. J. A. Janssen, et al., *Macrosegregation in continuously cast steel billets and blooms.* Applied Scientific Research, 1994. **52**(1): p. 21-53.

87. Vušanović, I., R. Vertnik, and B. Šarler, *A simple slice model for prediction of macrosegregation in continuously cast billets*, in *The 3rd International Conference on Advances in Solidification Processes*2011, IOP Publishing.

88. Bellet, M. *Two-Phase Multiscale FEM Modelling of Macrosegregation Formation in Steel Slabs*. in *AIP Conference Proceedings*. 2007.

89. Hardin, R.A., K. Liu, and C. Beckermann, *Development of a Model for Transient Simulation and Control of a Continuous Slab Caster*, in *Materials Processing in the Computer Age III*, V.R.V.a.H. Henein, Editor 2000: Warrendale , PA. p. 61-74.

90. Meng, Y. and B.G. Thomas, *Heat Transfer and Solidification Model of Continuous Slab Casting: CON1D.* Metallurgical Transactions B, 2003. **685-705**(34B): p. 685-705.

91. Beckermann, C. and R. Viskanta, *Double-Diffusive Convection during Dendritic Solidification of a Binary Mixture.* PhysicoChemical Hydrodynamics, 1988. **Vol.10**: p. pp. 195-213.

92. Won, Y.-M. and B.G. Thomas, *Simple Model of Microsegregation during Solidification of Steels.* Metallurgical and Materials Transactions A, 2000. **A**.

93. Voller, V.R., *Numer. Heat Transfer, Part B,* 1990.

94. J., M. and L. S., *Calculation of thermophysical properties in carbon and low-alloyed steels for modelling of solidification processes.* Metallurgical and Materials Transactions B, 1994. **25B**: p. 909-916.